

**LIMITATIONS OF LIFEBOATS OPERATING IN ICE  
ENVIRONMENTS**

**ALLISON KENNEDY**





# Limitations of Lifeboats Operating in Ice Environments

by

©Allison Kennedy

A thesis submitted to the  
School of Graduate Studies  
in partial fulfilment of the  
requirements for the degree of  
Master of Engineering

Faculty of Engineering and Applied Science

Memorial University of Newfoundland

July, 2010

St. John's

Newfoundland

## **Abstract**

Conventional lifeboats have not been designed to withstand ice loads. It is currently uncertain if these boats have the structural capacity to withstand an ice collision. The main objective of the research reported here is to determine the structural limitations of conventional lifeboats in order to help devise safe operating procedures for lifeboats in ice.

Three sets of experiments were carried out to gather data required to address the problem of conventional lifeboats operating in ice. Experimentation consisted of material testing of lifeboat fibreglass, laboratory testing of full scale ice impacts, and full scale field trials of a conventional lifeboat in ice. Both the laboratory and field trial results were used in the development of a simple energy model to represent ice loading of a conventional lifeboat operating in ice. The model predictions were compared with material structural limitations defined from laboratory test results. The comparisons provide guidance in determining safe and unsafe operating conditions for a conventional lifeboat in ice.

There are a number of possible practical outcomes from this research. Lifeboat design methods can be improved, new regulations can be introduced to guide lifeboat manufacturers, and the insight into operational considerations can be incorporated in lifeboat training.

## **Acknowledgments**

Many thanks are given to supervisor Dr. Brian Veitch and co-supervisor António Simões Ré without whom this research would not be possible. Thanks are extended for the guidance, theoretical advice, and patience throughout the thesis writing process. It was a great honour to receive insight and direction from two people who are so accomplished and dedicated in their areas of work.

The author is grateful for the financial support received throughout the graduate program. Thanks are extended to the Faculty of Engineering and Applied Science in particular Dr. Brian Veitch for support in the form of a Fellowship. Thanks are also extended to the Department of Education, Government of Newfoundland and Labrador, for a scholarship received relating to Students who Pursue Studies in the Sciences Related to Resource Development. The author is extremely thankful to the Institute for Ocean Technology for the opportunity of part-time employment, for technical support, assistance in experimental testing, and the opportunity to conduct research in an excellent research facility. The author is grateful to the technical staff of the Faculty of Engineering and Applied Science's laboratories for guidance and support throughout the testing phase.

## Table of Contents

Abstract .....	i
Acknowledgements .....	ii
List of Tables .....	vi
List of Figures .....	vii
List of Symbols .....	ix
List of Abbreviations .....	xii
List of Appendices .....	xiii
1 Introduction.....	1
1.1 Aim of Work.....	1
1.2 Scope of Work .....	1
1.3 Literature Review.....	3
2 Experimentation.....	9
2.1 Tensile Tests .....	9
2.1.1 Factor Selection .....	10
2.1.2 Factor Levels.....	10
2.1.3 Experimental Design.....	11
2.1.4 Specimen Preparation .....	12
2.1.4.1 Specimen Temperature .....	12
2.1.4.2 Specimen Heat Treatment.....	12
2.1.4.3 Specimen Submergence .....	13
2.1.4.4 Specimen Pre-Stress.....	13
2.1.5 Experiment Procedure.....	14
2.1.6 Results.....	15
2.1.7 Analysis of Results .....	16
2.1.8 Conclusions.....	19
2.2 Hydraulic Ram Tests.....	20
2.2.1 Data Acquisition System.....	21
2.2.2 Experimental Error.....	22
2.2.3 2008 Hydraulic Ram Tests.....	23
2.2.3.1 Room Temperature 18"x18" Panel.....	24
2.2.3.2 Chilled 18"x18" Panel .....	26
2.2.3.3 Data Analysis.....	27
2.2.3.4 Lessons Learned.....	29
2.2.4 2009 Hydraulic Ram Tests.....	30
2.2.4.1 Test Plan.....	31
2.2.4.2 Test Results.....	32
2.2.4.3 Deformation Pattern.....	32
2.2.4.4 Data Analysis .....	33
2.2.5 Comparison of 2008 and 2009 Tests .....	37
2.2.6 Conclusions.....	41
2.3 Pendulum Tests.....	42
2.3.1 Test Objectives.....	43
2.3.2 Test Set Up.....	43
2.3.3 Instrumentation .....	47

2.3.4	High Speed Camera Calibration .....	51
2.3.5	Testing Procedure .....	52
2.3.6	Test Plan.....	54
2.3.7	Data Calibration .....	55
2.3.8	Results.....	57
2.3.9	Validation of Results.....	58
2.3.10	Data Analysis .....	62
2.3.10.1	Panel Deflection Energy .....	62
2.3.10.2	Coefficient of Restitution.....	64
2.3.10.3	Global Energy .....	66
2.4	Field Trials.....	70
2.4.1	Lifeboat .....	71
2.4.2	Instrumentation .....	71
2.4.3	Test Plan.....	73
2.4.4	Ice Conditions .....	74
2.4.5	Results.....	79
2.4.6	Data Analysis.....	82
2.4.7	Field Trial Comparison to Hydraulic Ram Tests.....	86
2.4.8	Conclusions.....	89
3	Modelling.....	90
3.1	Modeling Approaches.....	90
3.1.1	Simple Force Model.....	92
3.1.2	Lindqvist Model.....	94
3.1.2.1	Model Test Comparison.....	96
3.1.2.2	Lindqvist Model Results .....	97
3.1.3	Extended Lindqvist Model.....	100
3.1.4	Conservation of Energy Model.....	103
3.1.5	Popov Model.....	106
3.1.5.1	Level Ice Case.....	108
3.1.5.2	Pack Ice Model .....	109
3.1.5.3	Effective Mass and Normal Velocity.....	111
3.1.5.4	Model Comparisons.....	113
3.1.5.5	Model Concerns .....	115
3.1.6	Extended Popov Model.....	116
3.1.6.1	Model Comparison.....	118
3.1.6.2	Sensitivity Analysis .....	120
4	Regulated Design.....	129
4.1	CSA Ice Design Loads.....	129
4.1.1	Global Loading .....	130
4.1.2	Local Loading .....	131
4.2	ISO Ice Design Loads .....	133
4.2.1	Global Loading .....	134
4.2.2	Local Loading .....	135
4.3	Design Load Comparison .....	136
4.3.1	CSA versus ISO .....	137
4.3.2	Design Loads versus Laminate Limitations.....	138

4.3.3	Design Loads versus Model Predictions.....	139
4.4	Applicability to Small Craft.....	140
5	Conclusions.....	142
	References.....	145
	APPENDIX A.....	151
	APPENDIX B.....	153

## List of Tables

Table 1: Tensile Test Results.....	15
Table 2: Effects List.....	17
Table 3: ANOVA Results.....	19
Table 4: Summary of 2009 Hydraulic Ram Test Results .....	32
Table 5: Calibration Table .....	56
Table 6: Summary of Pendulum Test Results.....	57
Table 7: Force Check Data .....	61
Table 8: Global Energy Percentages.....	69
Table 9: Ice Measurements .....	76
Table 10: Ice Strength Range.....	78
Table 11: Summary of Field Trial Data.....	80
Table 12: Hydraulic Ram Limits and Typical Field Measurements.....	88
Table 13: Design Loads for Nominal Area of 0.018 m <sup>2</sup> .....	139

## List of Figures

Figure 1: Ice Failure Process.....	2
Figure 2: Specimen Pre-Stress .....	13
Figure 3: Tensile Testing Machine .....	14
Figure 4: Tested Specimens.....	16
Figure 5: Diagnostic Plots.....	18
Figure 6: Hydraulic Ram Test Set Up.....	20
Figure 7: Underneath Video Camera Set Up .....	22
Figure 8: 18" ×18" Panel Test Setup .....	24
Figure 9: Room Temperature 18"×18" Panel After Impact.....	25
Figure 10: Room Temperature 18"×18" Panel Damage Pattern .....	25
Figure 11: Chilled Panel After Impact.....	27
Figure 12: 2008 Hydraulic Ram Results.....	28
Figure 13: 18" and 30" Deformation Patterns .....	33
Figure 14: 24", 26" and 28" Panel Results .....	35
Figure 15: 2009 Hydraulic Ram Results.....	36
Figure 16: Comparison of 2008 and 2009 Test Deformation Pattern.....	38
Figure 17: Comparison of 2008 and 2009 Test Underside Camera.....	38
Figure 18: Comparison of 18"×18" Panel Results.....	40
Figure 19: Acrylic Panel and Sea Chest .....	42
Figure 20: Lifeboat support system .....	44
Figure 21: Ice sphere carving.....	45
Figure 22: Ice sphere hoisted to required drop angle.....	46
Figure 23: Port Impact Panel and Load Cells .....	48
Figure 24: Ice sphere accelerometers inside protective casing.....	49
Figure 25: External LVDT.....	49
Figure 26: High speed camera images.....	52
Figure 27: Accelerometer box fitted to ice sphere.....	53
Figure 28: Drop angle measurement.....	53
Figure 29: Mounted Accelerometer Measurements.....	59
Figure 30: Load Cell Measurements – 10 kN .....	60
Figure 31: Load Cell Measurements – 50 kN .....	60
Figure 32: Load Cell Arrangement .....	63
Figure 33: Panel Deformation Analysis.....	64
Figure 34: Coefficient of Restitution Analysis .....	66
Figure 35: Global Displacement - 0.5" LVDT Measurement.....	68
Figure 36: Field Test Location.....	70
Figure 37: External Control Station.....	72
Figure 38: Lifeboat Manoeuvre in Ice .....	74
Figure 39: Level and Pack Ice Conditions.....	74
Figure 40: Typical Ice Thickness.....	75
Figure 41: Internal Camera View of Ice Thickness .....	76
Figure 42: Front Camera Views.....	78
Figure 43: Force versus Time Curve for Ice Impact.....	81
Figure 44: Field Impacts – Level and Pack .....	82

Figure 45: Lifeboat Collision with Melting Level Ice .....	85
Figure 46: Field Impacts - Front and Side .....	86
Figure 47: Overhead View of Field Trial Impact .....	87
Figure 48: Simple Force Model: Global Acceleration versus Speed.....	93
Figure 49: Hull Angles (Adapted From Lindqvist, 1989) .....	96
Figure 50: Lindqvist Model Predictions Compared To Resistance Test Results .....	98
Figure 51: Ice Resistance versus Speed .....	99
Figure 52: Extended Lindqvist Comparison with Field Trial Measurements.....	102
Figure 53: Popov Model Comparison with Field Measurements .....	114
Figure 54: Extended Popov Pack Ice Comparison .....	119
Figure 55: Extended Popov Level Ice Comparison .....	119
Figure 56: Pack Ice Predictions – Ice Mass Variation .....	121
Figure 57: Level Ice Predictions - Ice Thickness Variation .....	122
Figure 58: Pack Ice Predictions - Ice Thickness Variation.....	123
Figure 59: Level Ice Predictions - Ice Strength Variation .....	124
Figure 60: Pack Ice Predictions - Ice Strength Variation .....	125
Figure 61: Level Ice Predictions - Stiffness Variation.....	126
Figure 62: Pack Ice Predictions - Stiffness Variation .....	127
Figure 63: Pack Ice Predictions – Coefficient of Restitution Variation .....	128
Figure 64: CSA Global Ice Loads.....	131
Figure 65: CSA Local Ice Loads .....	133
Figure 66: ISO Global Ice Loads .....	135
Figure 67: ISO Local Ice Design Loads .....	136
Figure 68: CSA vs ISO - Local Design .....	137
Figure 69: CSA vs ISO - Global Design.....	138
Figure 70: Operational Guidance.....	143

## List of Symbols

### General Terms

$x, y, z$	Coordinate system axis
$v_1, v_2$	vessel speed prior to and after collision
$g$	acceleration due to gravity
$e$	Coefficient of restitution between lifeboat laminate and ice
$k$	Panel stiffness
$v_b$	Ice brine volume
$a_{global}$	Global acceleration of lifeboat

### Ice Terms

$m_{ice}$	Ice mass
$H_{ice}$	Ice thickness
$\sigma_c$	Ice compressive strength
$\sigma_f$	Ice flexural strength
$E$	Ice modulus of elasticity

### Lifeboat Parameters

$L$	Lifeboat length on waterline
$B$	Lifeboat breadth
$T$	Lifeboat draft
$m_{lifeboat}$	Lifeboat loaded mass

### Lindqvist Terms

$R_c$	Resistance to crush ice
$R_B$	Resistance to break ice

$R_s$	Resistance to submerge ice
$\sigma_b$	Ice breaking strength
$A_u$	Area of the flat bottom
$A_f$	Area of the bow
$\delta\rho$	Density difference between water and ice
$\alpha, \phi$	Bow angles
$\psi$	Function of $\alpha$ and $\phi$ ; $\psi = \arctan(\tan\phi/\sin\alpha)$
$\mu$	Friction factor between ice and hull surface
$A_{yz}, A_{xz}, A_{xy}$	Submerged area in $YZ$ , $XZ$ , and $XY$ planes
$m_{add, ice}$	Added mass of ice piece
$w$	Ice cusp width
$D$	Ice cusp depth
$v_s$	Ice sliding speed

#### **Conservation of Energy Model Terms**

$l_{indent}$	Ice indentation distance
$E_{propulsion}$	Propulsion energy
$E_{ice}$	Ice failure energy
$E_{panel}$	Panel deformation energy
$t$	Thrust deduction fraction
$T$	Lifeboat thrust

#### **Popov Terms**

$P_{ice}$	Ice pressure
$A$	Nominal ice contact area

$P_o, ex$	Ice pressure area constants
$\delta_{ice}$	Ice indentation
$R$	Lifeboat bow radius
$m_e$	Effective mass of lifeboat at collision point (kg)
$v_n$	Normal velocity at collision point (m/s)
$C_o$	Mass reduction coefficient
$\lambda l, \mu l, \eta l$	Moment arms
$l, m, \text{ and } n$	Direction cosines
$AM_x, AM_y, AM_z, AM_{pit}, AM_{yaw}$	Added mass terms
$r_x, r_y, r_z$	Radii of gyration

#### CSA Standard Terms

$C_p, D_p$	Empirical constants that relate the ice pressure to the nominal contact area
$x_o$	Offset in the distribution of full-scale measurements
$\alpha$	Factor that defines the dependence of pressure on contact area
$F_z(z_e)$	Exceedence probability
$v$	Expected number of events
$r$	Expected proportion of impacts

#### ISO Standard Terms

$w$	Structure width
$C_R$	Ice strength coefficient.
$m$	Empirical exponent
$P_G$	Global ice pressure
$P_L$	Local ice pressure

## List of Abbreviations

ANOVA	Analysis of Variance
ASTM	American Society for Testing and Materials
CIS	Canadian Ice Services
CSA	Canadian Standards Association
DAS	Data Acquisition System
DC	Direct Current
DE	Design Expert™
DGPS	Digital Global Positioning System
DOE	Design of Experiments
EER	Escape, Evacuation and Rescue
GPS	Global Positioning System
IMO	International Maritime Organization
ISO	International Standards Organization
ITTC	International Towing Tank Conference
LSA	Life Saving Appliances
LVDT	Linear Variable Differential Transformer
PA	Pressure - Area
SNAME	Society of Naval Architects and Marine Engineers
TEMPSC	Totally Enclosed Motor Propelled Survival Craft

**List of Appendices**

APPENDIX A

2009 Hydraulic Ram Test Results

APPENDIX B

Field Trial Results

# 1 Introduction

## 1.1 *Aim of Work*

The aim of this thesis work is to assess key performance limitations of lifeboats operating in ice. Of particular interest are the structural limitations and how they relate to various ice conditions. To gain insight into this matter, laboratory and field experiments have been conducted and used in the development of a simple semi-empirical model to represent a conventional lifeboat interacting with ice. This work can provide insight into the design of an ice-capable lifeboat for use in Arctic and Sub-Arctic operations. It can also be incorporated into performance based standards that govern lifeboat operation in ice environments.

## 1.2 *Scope of Work*

Ice failure can occur in different modes depending on loading speed, loading magnitude and contact geometry. Ice can exhibit continuum behaviour as well as fracture behaviour. Continuum behaviour involves failure modes such as elastic buckling, creep buckling and ductile indentation (Sanderson, 1988). Continuum behaviour is apparent for small strain rates and thus does not describe the typical behaviour of ice upon contact with a lifeboat. Ice fracture behaviour includes the following modes of ice breaking: crushing, flexural failure, radial cracking and spalling (Sanderson, 1988). These modes are represented in Figure 1 below which illustrates a typical lifeboat interaction with ice.

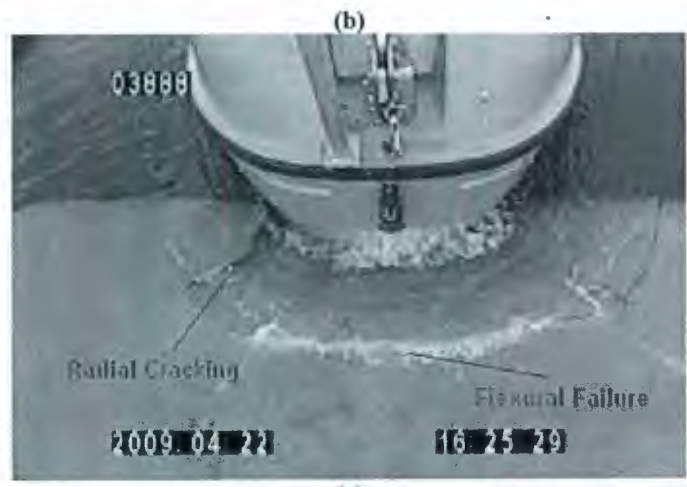


Figure 1: Ice Failure Process

The process of ice failure due to fracture can involve either fracture mode alone, or the combination of two or more modes. Sanderson (1988) described an ice deformation mode map. This map can be used as an aid to predict the ice failure type. The map is a function of both indentation rate and aspect ratio. According to this map, the lifeboat, while operating under normal speed, will interact with ice at field trial thickness such that it fails in crushing with radial and circumferential cracking. This suggested ice failure mode was observed during field trials and is represented in Figure 1(a) and Figure 1 (b).

The limitations of a lifeboat's structure in ice are a function of the laminate strength, the ice conditions and the ice failure mechanism. The failure mode is directly linked to the ice conditions: strength, thickness and type. Lifeboats are typically constructed of laminate material. The extent to which the hull deforms plays a role in the magnitude of the impact force from an ice collision.

### *1.3 Literature Review*

There has been research conducted regarding the operation of ships in ice to inform the structural and propulsive design of icebreaking ships. This research includes laboratory experiments, full-scale field trials, and numerical modelling. Some of this work can be extended to provide insight to the phenomena involved in lifeboats operating in ice. However, icebreaking ships and lifeboats react differently to ice loading due to variations in displacement, maximum speed, hull-material type and bow configuration. Hence, there

is a need for research focused on lifeboat-ice interaction to gain a full understanding of the limits of these small boats in ice.

Model tests of conventional lifeboats operating in ice conditions were conducted by Simões Ré and Veitch (2007), Barker et al. (2004), Lau and Simões Ré (2006) and Simões Ré et al. (2006). Simões Ré and Veitch (2007) and Lau and Simões Ré (2006) performed three series of lifeboat model tests including launching tests, over-powered sail away tests, and resistance tests. The launching and over-powered sail away tests concluded that ice concentrations from 6/10<sup>ths</sup> to 8/10<sup>ths</sup> were impassable by the lifeboat and the limit was reached at lower ice concentrations for thicker and larger ice pieces (Simões Ré & Veitch, 2007). These tests also concluded that increases in engine power extended the performance limits in ice only marginally. The resistance test results led to the development of a numerical model of the lifeboat formulated using the discrete element code DECIDE3D (Lau & Simões Ré, 2006). This model assumes the vessel is a rigid body and thus does not consider hull deformation. Also, this model did not consider ice failure in flexure which resulted in predicted force values higher than measured force values in some cases (Lau & Simões Ré, 2006). Barker et al. (2004) performed lifeboat model tests in ice and waves. These tests indicated that the lifeboat could travel through higher ice conditions when waves were present (Barker et al, 2004). However, this was only true when the lifeboat travelled in the direction of the waves. These tests did not consider ice impact loads.

Field trials involving a full-scale lifeboat operating in ice have been conducted and reported by Igloliorte et al. (2007, 2008) and Simões Ré et al. (2008). One set of trials took place in the Northumberland Strait, between PEI and Nova Scotia, during the winter of 2002. In these un-powered field trials the lifeboat was left un-manned in the ice and checked upon periodically via helicopter. The measurement instrumentation for these trials included a GPS, digital thermometers, bilge alarm, battery voltage indicator, inclinometers, pressure sensors, video camera and a load cell. The GPS was used to measure the position and track of the lifeboat while the load cell was attached between the lifeboat and its mooring line to measure global loads while tethered (Igloliorte et al., 2007).

The Igloliorte (2007) trials showed external structural damage to the lifeboat hull. The majority of damage was due to a steel cladding that was added to the hull for added strength. This cladding was subsequently pulled away from the laminate resulting in rivet holes through the hull. The hull structure was damaged but not to the extent to jeopardize hull integrity. There were cracks apparent on the port transom, on the starboard bow and on the port and starboard sides of the hard chine. Also, the internal foam layer was separated from the hull laminate. The damage was due to ice compression loading. During testing the ice concentrations were between 8/10 and 9/10<sup>+</sup> as reported by Canadian Ice Services (CIS). Another observation from these trials was that ice thickness is a less important factor in lifeboat survivability than ice strength (Igloliorte et al., 2007). This point was made after observing the lifeboat extruded from the ice in various ice thicknesses.

A second set of field trials conducted by Igloliorte et al. (2008) were held in the spring of 2006. These trials were held in New World Island, Newfoundland. During these trials the Totally Enclosed Motor Propelled Survival Craft (TEMPSC) was driven into broken and brash ice conditions and observations were made based on the performance. These trials differed from the previous trials in that the TEMPSC was manned and manoeuvred through the ice. Findings from these tests indicated that the TEMPSC had significant capability to operate in managed ice covered water (Igloliorte et al., 2008).

Simões Ré et al. (2008) also completed field testing of a TEMPSC in sea ice. One set of field trials commenced in May 2007, in the vicinity of Triton, NL. The TEMPSC was outfitted with an array of instrumentation including global accelerometers and a global positioning system. Tests were conducted in both level and pack ice conditions. These field trials indicated that TEMPSC progress was difficult or prevented in 7/10<sup>ths</sup> or higher ice coverage and that better progress was made at concentrations at and below 5/10<sup>ths</sup> (Simões Ré et al., 2008). A second set of field trials was conducted with the same conventional TEMPSC after it was modified to include a bow shoulder impact panel. These trials took place in April, 2009 in Triton, NL. The impact panel contained a dynamometer capable of recording ice impact forces in the *x*, *y* and *z* directions. Findings from these field trials have not yet been published but will be described and used in this thesis.

There has been extensive numerical modelling concerning ice-breaking ships in ice. Popov et al. (1968) numerically modelled an ice breaker to predict collision forces. This model reduces a 3D equation to 1D by assuming the collision is between a single body and a rigid wall (Popov et al., 1968). Lindqvist (1989) proposed a model to represent a ship operating in level ice. This equation can be used to predict the ice resistance forces. Another numerical model of a ship in level ice was presented by Liu et al. (2006). This is a rigid body model that was developed for use in an ice navigation simulator. Other attempts to predict the ice resistance on a structure have been reported by Lewis and Edwards (1970) Lewis et al. (1982), Colbourne (1987) Spencer (1992), Milano (1973, 1980) and Kotras et al. (1983), for example. There were no publications found describing numerical modelling of small-craft in ice.

Alternatives to the lifeboat mode of evacuation in ice have been considered. The Arktos is an amphibious evacuation craft that was designed for operation in Arctic ice conditions (Seligman et al., 2008). There have also been solutions proposed by O'Brien (2004), Johansson (2006) and Browne et al., (2008) regarding the design of a modified lifeboat capable of ice operation. The Seascope system is composed of an evacuation craft and deployment mechanism system that has been developed to the prototype stage (O'Brien, 2004). Johansson (2006) presented concept design ideas for an ice breaking lifeboat. This lifeboat is over 200 tonnes with a capacity for 250 people. Browne et al., (2008) presented the practical design of an ice strengthened lifeboat that has been developed to the pre-prototype design stage. This lifeboat has a capacity for 66 passengers and a full-load weight of 18.0 tonnes.

There are regulations relevant to the design of TEMPSC for open water, but currently there are no guidelines on TEMPSC design in ice. The International Maritime Organization (IMO) has issued life-saving appliances guidelines that govern the structural design and maintenance of lifesaving equipment (Life-Saving Appliances, 2003). IMO has also issued a guideline for ships operating in polar regions which has a chapter governing life-saving appliances. However, this chapter still does not account for ice loading design (IMO, 2007). The International Standards Organization (ISO) has circulated a draft standard (ISO 19906, 2008) that provides guidance for the design and operational procedures of Arctic offshore structures. This draft standard has a chapter regarding EER systems that defines objectives for evacuation craft but does not provide detailed design guidance. Transport Canada has released standards for lifeboats that govern the material selection, design, and construction of conventional lifeboats (Transport Canada, 1992). These standards do not provide any guidance relevant to ice loading. There have been environmental guidelines proposed for EER systems in ice-covered waters by Timco and Dickins (2005). These guidelines conclude that there is no single EER system that can reliably meet the requirements of all Arctic structures.

## 2 Experimentation

Both laboratory testing and field trials were conducted to explore areas of lifeboat-ice interaction and to gather relevant data. Tensile tests were conducted to determine the effect of certain parameters on lifeboat laminate strength. Hydraulic ram tests were performed to define the impact limitations of lifeboat laminate. Pendulum tests involving ice spheres and a full-scale lifeboat were executed to determine empirical values required for modelling and to prepare a data acquisition system for field testing. Field trials were performed in Triton, NL, in which a full-scale lifeboat was operated in sea ice. The purpose of these trials was to gather realistic ice impact data for comparison with modelling predictions.

### 2.1 *Tensile Tests*

An important characteristic of the structural strength of fibreglass is the tensile strength. There are a number of factors that are thought to affect the tensile strength of fibreglass. The factors that were assessed in this study include material lay-up, specimen temperature, heat treatment, submergence and pre-stress. The following analysis details a set of tensile tests that were conducted to determine which of the aforementioned factors significantly affected the tensile strength and thus the structural integrity of lifeboat fibreglass. The tensile tests followed ASTM standards (1996). The test results were analysed using methods of Design of Experiments (DOE).

### **2.1.1 Factor Selection**

A primary consideration of the tensile tests was the effect of material lay-up on fiberglass tensile strength. Limitations in the quantity of actual lifeboat material available prevented all laboratory testing from being completed on the same material. Replicated lifeboat laminate panels were prepared in accordance with the lay-up and materials used in the lifeboat material. The laminate lay-up of the resin and cloth was selected based on the results of a burn test completed on a piece of the original lifeboat laminate. To compare the strength test results of replicated and actual lifeboat fiberglass an assessment was made concerning the reaction of each material to loading. The remaining four factors selected for assessment in the study were temperature, heat treatment, submergence and pre-stress, which are factors that lifeboats are regularly subjected to in their life cycle and may affect the material strength.

### **2.1.2 Factor Levels**

The tensile tests were assessed using a factorial experiment design. This type of design allows for an assessment of a large number of factors from the results of a limited number of experimental runs. There are two levels for each factor in a factorial design. A level represents a particular value of the factor. The two levels for the categorical factor - material lay-up - were actual lifeboat material and replicated lifeboat material. The replicated material was set as the low level of this factor and the actual material was set as the high level. The actual lifeboat fiberglass came from the hull of an out of use TEMPS. The levels for temperature were chosen based on the available facilities as well

as ease of experimentation. The cold room was pre-set to  $-20^{\circ}\text{C}$  for specimen preparation. A sample specimen was chilled in the cold room overnight and then transferred using an insulated cooler to the tensile testing machine. The temperature of the specimen was then recorded as  $-10^{\circ}\text{C}$ . This value was chosen to be the lower level of the temperature factor. Room temperature, which was measured at  $22^{\circ}\text{C}$ , was used for the upper temperature level.

Heat treatment, submergence and pre-stress were all categorical factors as well, with the lower level representing 'no' and the upper level representing 'yes.' For example, a specimen that had a low level for the pre-stress factor was not subjected to pre-stress. The methods involved in specimen treatment are discussed in a subsequent section of this thesis.

### ***2.1.3 Experimental Design***

DOE methods were used to design an optimal experimental plan to determine the significant factors effecting fibreglass tensile strength. An effective method to determine the significance of a set of factors to a result is to perform a fractional factorial design. Five factors were assessed in the tensile experiments. A half-fraction factorial design with five-factors would be of the form  $2^{5-1}$  and result in a total of 16 tests. This experimental outline would allow for an assessment of the significance of the five factors on tensile strength.

As a means of ensuring valid results, two replicates of the half fraction design were completed. By testing two replicates, the possibility of an outlying result being analysed is greatly reduced. The second replicate acts as a verification of the first and a large variance between the two would indicate a problem in the results.

#### ***2.1.4 Specimen Preparation***

This section describes the preparation of the tensile samples prior to testing. The tensile samples were cut to standard test size, then milled to their requisite thickness in a milling machine, and subjected to treatments. The treatment times were selected such that they fit within the testing schedule.

##### ***2.1.4.1 Specimen Temperature***

The specimens were cooled to  $-20^{\circ}\text{C}$  in a freezer room and then transferred to the test site in an insulated carrier. Prior to testing, the temperature of the specimens was measured using a digital thermometer. The tests were not conducted until the temperature of the chilled specimens rose to  $-10^{\circ}\text{C}$ , which is the lower level of the temperature factor. The specimens tested at  $22^{\circ}\text{C}$  were brought to the testing site 24 hours prior to testing. The temperature of the test site was consistently  $22^{\circ}\text{C}$ . The 24-hour wait allowed the specimens to adjust to the room temperature.

##### ***2.1.4.2 Specimen Heat Treatment***

The first step was to cool the specimens to approximately  $-20^{\circ}\text{C}$  in the large cold room. The specimens were left at this temperature for 24 hours. The specimens were then

removed from the cold room and warmed to room temperature for approximately 8 hours. Then they were returned to the cold room again for an additional 24 hours and allowed to cool to  $-20^{\circ}\text{C}$ . The specimens were then removed from the cold room and allowed to adjust to room temperature.

#### *2.1.4.3 Specimen Submergence*

The specimens were submerged in fresh water at  $18^{\circ}\text{C}$  for seven hours. After immersion the specimens were dried prior to any other treatments and prior to testing.

#### *2.1.4.4 Specimen Pre-Stress*

Each specimen was pre-stressed by hanging a 5 kg weight from its midpoint for 21 hours. While the weights were in place the specimens were supported at each endpoint leaving the mid section unsupported. A picture representing this set up is shown below.



**Figure 2: Specimen Pre-Stress**

### **2.1.5 Experiment Procedure**

The experimental procedure followed for the tensile tests is outlined below.

1. Measurements of width and thickness were taken using a vernier caliper at the midsection of the reduced width section of the specimen.
2. The width and thickness values were used to formulate the area required for stress calculations.
3. The specimens were placed in the tensile machine and clamped at both ends.
4. A strain gauge was attached to the midsection of the specimen.
5. Increasing tensile force was applied to the specimen until fracture occurred.
6. All compiled data was saved to a folder specific to the test specimen.

The figure below shows the testing machine that was used to conduct these experiments.



**Figure 3: Tensile Testing Machine**

### 2.1.6 Results

The results gathered during experimentation are shown below. Note the large range of tensile stress values that were observed.

Table 1: Tensile Test Results

Test #	Tensile Stress (Mpa)	Test #	Tensile Stress (Mpa)
1	133.76	17	108.04
2	111.89	18	136.88
3	113.90	19	117.62
4	103.45	20	141.23
5	94.06	21	136.10
6	97.45	22	111.44
7	146.21	23	46.08
8	143.96	24	88.44
9	64.11	25	140.25
10	89.83	26	43.96
11	39.86	27	130.24
12	98.03	28	115.11
13	143.21	29	147.55
14	132.68	30	86.22
15	88.13	31	97.52
16	130.29	32	149.14

All specimens broke in a similar location, which was in the middle section but near the wider exterior section. None of the specimens broke directly in the centre of the specimen. The figure below shows all specimens after they were tested.



**Figure 4: Tested Specimens**

### ***2.1.7 Analysis of Results***

All experimental results were entered into the statistical software Design Expert (DE) for analysis. This program uses the ANOVA test to evaluate the results and formulate conclusions. The first consideration was to decide which effects should be included in the model. To do this one must observe the effects list provided by DE and see which effects had large percent contributions.

The effects list indicated that *C*, *E*, *AB* and *BE* had the highest percent contributions and thus should be included in the model. This model is not hierarchical and thus DE automatically selected *A* and *B* to also be included in the model in order to have hierarchy. The effects list is shown below.

Table 2: Effects List

	Term	Stdized Effects	Sum of Squares	% Contribution
	Intercept			
	A-Material Type	-1.41	15.94	0.053
	B-Temperature	-1.49	17.65	0.059
	C-Heat Treatment	-18.76	2816.97	9.40
	D-Submergance	-1.07	9.12	0.030
	E-Pre-Stress	32.08	8233.90	27.49
	AB	-12.85	1321.33	4.41
	AC	-2.24	39.99	0.13
	AD	-3.87	119.69	0.40
	AE	9.53	726.81	2.43
	BC	2.24	39.98	0.13
	BD	-0.23	0.41	1.370E-003
	BE	12.50	1250.91	4.18
	CD	-10.06	808.93	2.70
	CE	5.63	253.78	0.85
	DE	0.63	3.13	0.010
	ABC		Aliased	
	ABD		Aliased	
	ABE		Aliased	
	ACD		Aliased	
	ACE		Aliased	
	ADE		Aliased	
	BCD		Aliased	
	BCE		Aliased	
	BDE		Aliased	
	CDE		Aliased	
	ABCD		Aliased	
	ABCE		Aliased	
	ABDE		Aliased	
	ACDE		Aliased	
	BCDE		Aliased	
	ABCDE		Aliased	
	Lack Of Fit		0.000	0.000
	Pure Error		14293.46	47.72

Next, the three main assumptions of the ANOVA test were verified. These were confirmed by reviewing the diagnostic plots. The assumption of normality was satisfied by viewing the normal plot of residuals and confirming that all data points aligned well with the normal line. The second assumption was that the variance of the data set was equally distributed around the mean. This was ensured by analysing the residuals versus predicted plot which proved that all data points had roughly equal variances. The third main assumption of the ANOVA was that the data was random. This was verified by viewing the residuals versus test plot. It should also be noted that the box-cox plot was

reviewed to determine if DE suggested a data transformation. There was no data transformation suggested. The diagnostic plots are shown below.

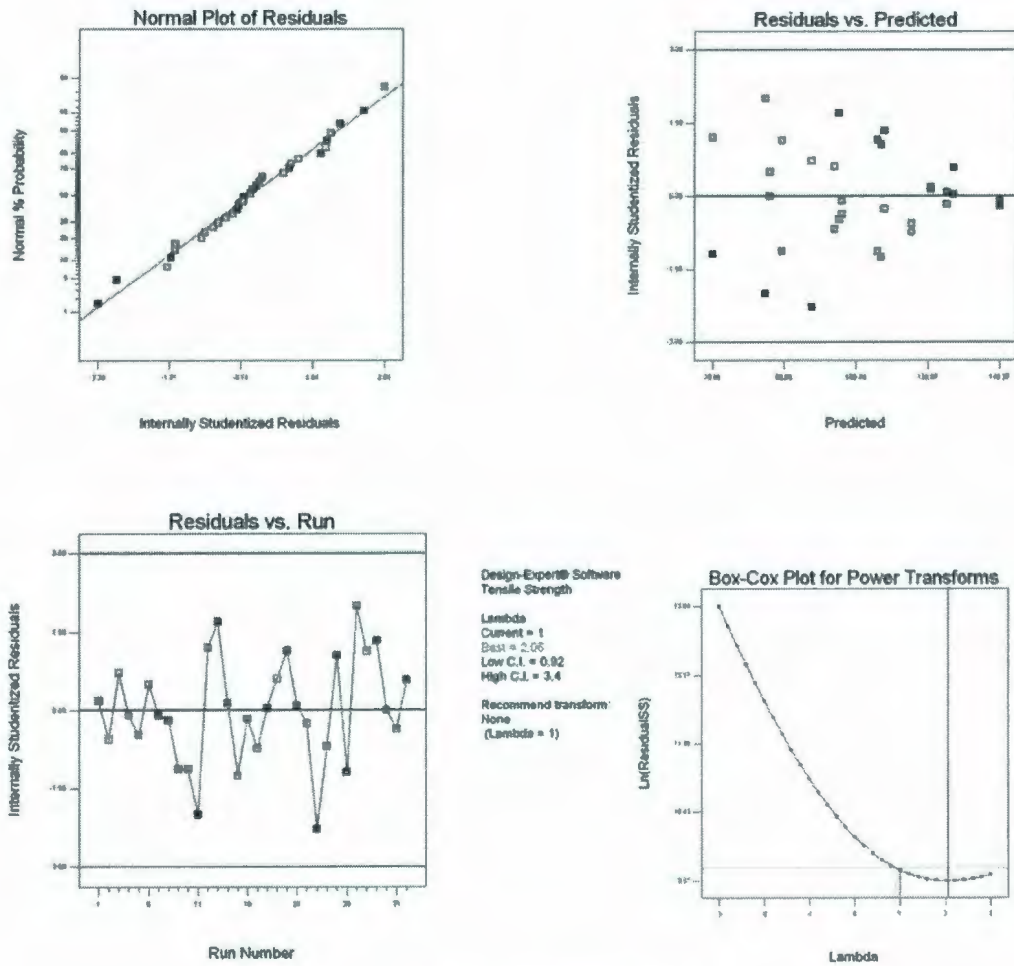


Figure 5: Diagnostic Plots

When all assumptions were verified the ANOVA results were studied. These results are shown below. An alpha value of 0.05 was used in this analysis and therefore any effects that had a p-value below 0.05 were deemed as significant.

Table 3: ANOVA Results

Source	Sum of Squares	df	Mean Square	F Value	p-value Prob > F
Model	13656	6	2276.16	3.49	0.0120
<i>A</i> -Material Type	15.94	1	15.93	0.024	0.8770
<i>B</i> -Temperature	17.65	1	17.64	0.027	0.8706
<i>C</i> -Heat Treatment	2817	1	2816.97	4.32	0.0480
<i>E</i> -Pre-Stress	8234	1	8233.9	12.63	0.0015
<i>AB</i>	1321	1	1321.33	2.03	0.167
<i>BE</i>	1251	1	1250.90	1.92	0.178
Residual	16295	25	651.81		
Lack of Fit	2002	9	222.42	0.248	0.980
Pure Error	14293	16	893.31		
Cor Total	29952	31			

The results indicated that the model itself was significant with a p-value of 0.012 and the lack of fit was not significant with a p-value of 0.9801, which indicated a good model. There were only two effects that were significant including *C* and *E* which corresponded to heat treatment and pre-stress respectively.

### 2.1.8 Conclusions

The tensile tests showed that heat treatment and pre-stress were significant factors. The findings implied that lifeboat laminate can be affected by temperature variation in ice environments and impacts with ice. The material-type did not significantly influence the tensile strength of lifeboat fibreglass. This indicated that replicated laminate material was representative of actual lifeboat laminate at least in terms of tensile strength.

## 2.2 Hydraulic Ram Tests

The hydraulic ram tests were structural tests in which a fibreglass specimen was impacted with a steel ram head until puncture occurred. Various sized fibreglass panels at both cold and warm temperatures were impacted. During hydraulic ram testing the ram head was moved at a constant speed of approximately 0.054 m/s. The purpose of the tests was to determine the limiting loads of lifeboat hull material and to establish the effect of panel size and temperature. The results of these tests can lead to the determination of an optimal panel size for a lifeboat operating in ice. During testing, the fibreglass panels were held in position by a metal frame that could be extended in two directions to accommodate a range of panel sizes. Below is an illustration of the test set up.



**Figure 6: Hydraulic Ram Test Set Up**

The majority of the test panels were fabricated to represent lifeboat laminate. There was laminate material available for testing which came from an out of use lifeboat. However,

there was only enough of this material to fabricate two 18"×18" panels. All panels were approximately ¼" thick which corresponds to a conventional lifeboat hull thickness.

Each fibreglass panel tested was marked with a 1"×1" grid on the interior side of the panel. The "interior" side represented the panel side without gel coat as this is the side of the panel that would be facing to the interior of the lifeboat. The purpose of this grid was to enable a comparison of damage pattern after testing.

### ***2.2.1 Data Acquisition System***

The data acquisition system for the hydraulic ram tests included three video cameras and a dynamometer, which was contained within the hydraulic ram itself. The dynamometer measured both the impact force and the deflection of the panel. One camera was positioned on the side of the panel and lights were arranged so that clear pictures could be obtained of the experiments. A second video camera was positioned in front of the panel viewing both the hydraulic ram and the panel, while a third small video camera was positioned underneath the panel to obtain an underside view of the deformation. The following figure illustrates the underneath camera set up. As can be seen from this picture, the base of the frame held the camera steady.

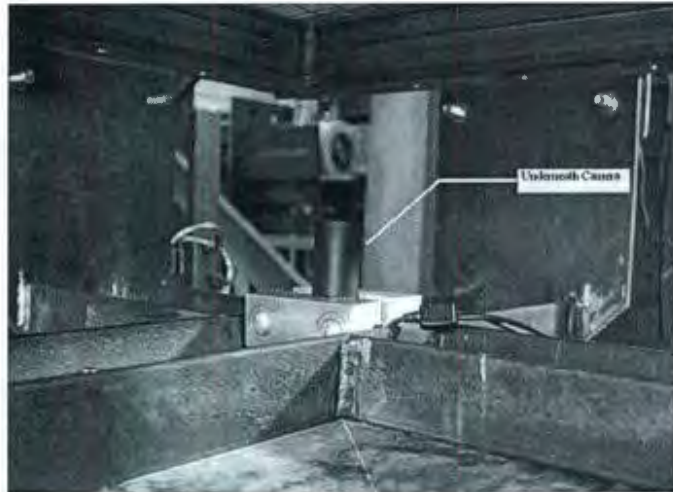


**Figure 7: Underneath Video Camera Set Up**

The hydraulic ram recorded force in the unit of kilo pound and displacement in the unit of millimetre. It measured the force and displacement at a frequency of 20 Hz. The hydraulic ram was connected electronically to a personal computer which stored the measured force and displacement values in comma separated variables files.

### ***2.2.2 Experimental Error***

The hydraulic ram tests contained a number of uncertainty elements contributing to the values of the measured data. An uncertainty analysis defined the interval in which the measured data fell.

There are two main types of error: precision and bias error. Precision error deals with the error involved in repetition of experimentation. There were no repeated tests completed in the hydraulic ram tests and therefore this term was ignored. Bias error is a fixed component of error which is the same for any experiment completed, that is, it does not

vary from test to test. The bias error was defined and included in the results of the hydraulic ram test findings.

There were two values measured: force and displacement. The force was measured by a 146 kilo pound load cell and the displacement was measured by a 10 inch LVDT. The rating of each device corresponds to the upper limit of measurement. The uncertainty involved in the displacement measurement was found in the 2009 MTS Services and Accessories catalogue. This listed the typical manufacturer's uncertainty in a linear LVDT as 2%. The uncertainty in force measurement was found from load cell specifications from Nova Tech Load Cells. The typical uncertainty involved in load cells calibrated hydraulically was listed as 1%. Error bars were added to the results of hydraulic ram testing to indicate the error range in displacement and force measurement.

### ***2.2.3 2008 Hydraulic Ram Tests***

Hydraulic ram tests were conducted in July 2008 with two 18"×18" laminate panels. These panels came from the hull of a conventional lifeboat. A goal of the 2008 tests was to determine the yield and ultimate force limit of lifeboat laminate panels. The other experimental goal was to gain a better understanding of the test process and parameters. The execution and analysis of these tests resulted in improvement of 2009 testing.

### *2.2.3.1 Room Temperature 18"x18" Panel*

The first test was conducted on an 18"x18" room temperature fibreglass lifeboat panel. The room temperature at the test facility was measured prior to testing and was found to be 20 °C. The panel was bolted on each of the four corners to the hollow metal frame. This simulated clamped end conditions on the panel. The circular impact head was driven into the centre of the fibreglass panel with increasing force until it punctured the panel. The figure below demonstrates the set up for this test.

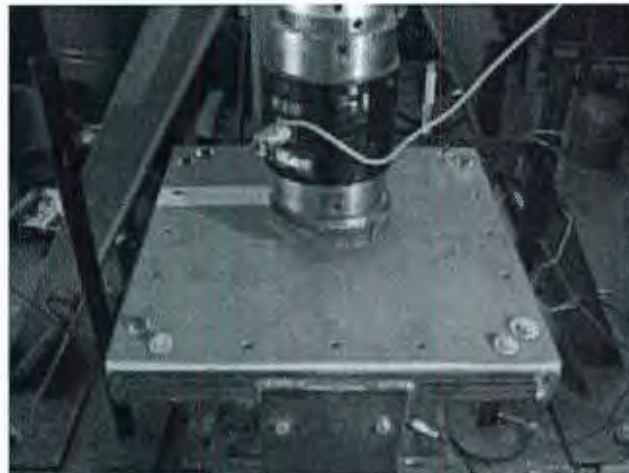


**Figure 8: 18" ×18" Panel Test Setup**

The panel was oriented in such a way that the circular impact head hit it in the centre at a 90-degree angle. The panel frame support was bolted onto the ground so that it did not move or shake upon impact. The panels were marked, North, South, East and West on the corresponding sides so that the damage of all panels could be compared at the impacted orientation. Below is a figure demonstrating the panel after impact.



**Figure 9: Room Temperature 18"×18" Panel After Impact**

The results from the hydraulic ram showed a peak force of approximately 74 kN and a maximum displacement of around 32 mm. The puncture in the material occurred around the perimeter of the impact head and then moved out towards the edge. This was observed in detail from bottom photographs of the deformed panel. The picture below represents the damage pattern.

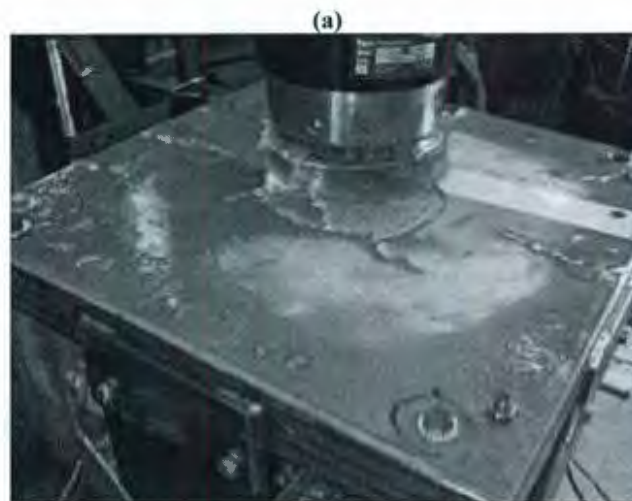


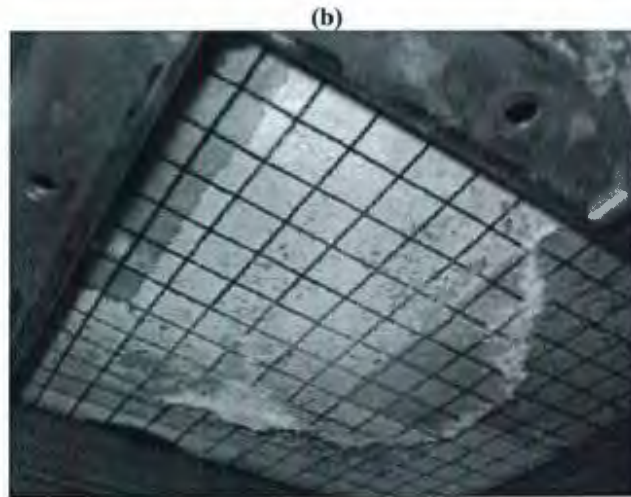
**Figure 10: Room Temperature 18"×18" Panel Damage Pattern**

Figure 10 indicates that the damage is in a circular pattern, which outlines the impact head and extends outwards in two directions towards the panel sides.

### *2.2.3.2 Chilled 18"x18" Panel*

The second hydraulic ram test was conducted on a lifeboat panel similar to the first but chilled to approximately  $-20^{\circ}\text{C}$ . The panel was chilled to represent the lifeboat panel operating in cold conditions. The set up was the same, with the panel centred such that the impact head struck in the center. The results of this impact showed a maximum force of approximately 75 kN and a maximum displacement of 42.4 mm. The maximum force value was close to the room temperature panel; however the chilled panel had a significantly larger maximum displacement. Pictures of the deformed panel are shown below.





**Figure 11: Chilled Panel After Impact**

The deformation patterns of both room temperature and chilled panels were quite similar. Both patterns outlined the circular impact head and lead out towards the panel sides.

### ***2.2.3.3 Data Analysis***

The results of both hydraulic ram tests were plotted as force versus deflection curves. The puncture energy was determined by finding the area under these curves, which was completed using integration. The puncture energy is the amount of energy the panel absorbs up until fracture. The force versus displacement plots for the cold and room temperature panels are shown below.

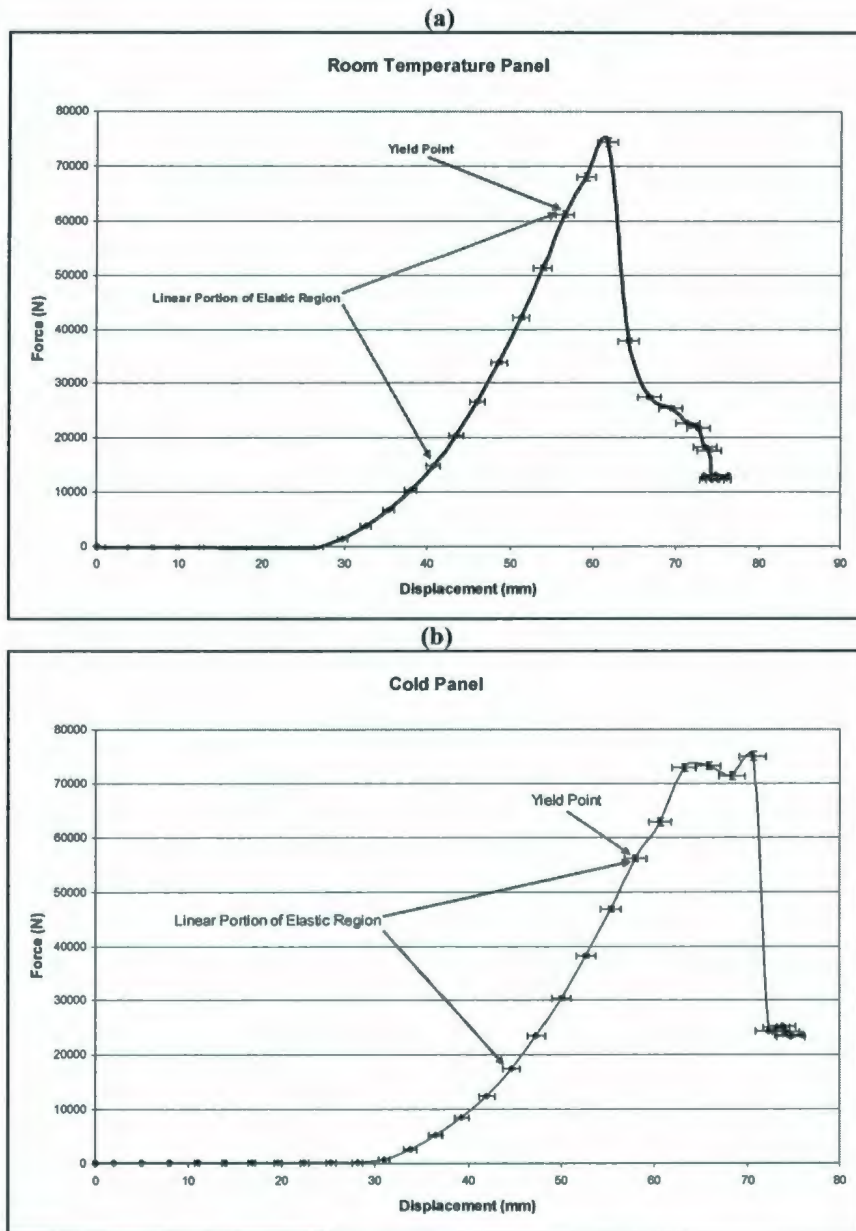


**Figure 12: 2008 Hydraulic Ram Results**

Data analysis showed that the room temperature panel had puncture energy of approximately 1000 J while the chilled panel had puncture energy of approximately 1500 J. Despite the fact that the maximum force values for both panels were similar, the amount of energy required to break the panels differed by nearly 500 J. In other words, it

took an additional 500 J to puncture the cold panel than it did to puncture the room temperature panel.

The ultimate strength of the panels could be found by dividing the maximum force by the impact area. The impact head of the hydraulic ram was a 3" radius circle. It was assumed that the impacting edge hit at a perfect 90-degree angle leading to a contact area of 0.018 m<sup>2</sup>. The ultimate strength for the room temperature and chilled panels was found to be 4.13 MPa and 4.17 MPa respectively.

The lifeboat panel stiffness was estimated by determining the slope of the elastic portion of the force versus displacement curve for the chilled laminate panel. Two considerations were made in this analysis. The first considered the linear portion of the elastic region of Figure 12. This resulted in a stiffness value of 2.91 MN/m. The second consideration involved the non-linear portion of the elastic region. The panel stiffness found using this method was 2.06 MN/m. Note that this is the stiffness as defined by the entire elastic range, beginning when the force starts to rise to the yield point. The range in lifeboat laminate stiffness was found to be 2.06 – 2.91 MN/m.

#### *2.2.3.4 Lessons Learned*

One of the goals of the initial two hydraulic ram tests was to gain a better understanding of the test process and parameters. From the initial tests there were a few interesting points that must be considered when preparing for future hydraulic ram tests. The first consideration involved the panel damage pattern. Damage was concentrated and

initialized around the perimeter of the impact head. A hemispherical impact head may prevent this from occurring. Another consideration was that the panel moved slightly as it was impacted. The frame must be securely bolted to the floor so that motions do not occur, which can cause errors. The final consideration was that the small underside panel camera did not cover the entire range of the panel. A camera with a broader range of vision must be used to capture the deformation of the entire panel.

#### ***2.2.4 2009 Hydraulic Ram Tests***

A second set of hydraulic ram tests were conducted in July, 2009. These tests were more substantial than the first tests in terms of the number of specimens tested and they incorporated the lessons learned from 2008 testing. The 2009 tests included testing 13 replicated lifeboat laminate panels. The 2009 hydraulic ram tests followed guidelines outlined in ISO standards.

The ISO standard: ISO 6603-2 entitled Plastics – Determination of puncture impact behaviour of rigid plastics - defines the practice of testing a sample specimen to determine the puncture impact energy. This protocol dictates the sample size to be either a 60 mm square or a 60 mm diameter circle, both having a thickness of 2 mm. The standard recommends a hemispherical striking head which is to be lubricated with oil or grease prior to each test. The standards were developed for drop tests, in which a steel object is dropped onto a test specimen. The sample size for the 2009 hydraulic ram tests

was varied from the ISO recommendation to mimic realistic lifeboat-ice impact situations.

There were some important differences in the arrangement of the 2009 tests that resulted from lessons learned from 2008 testing and recommendations from ISO 6603 – 2. These differences include the following:

1. The hydraulic ram head used was hemispherical in shape with a radius of 7.6 cm (3”).
2. The bolts holding the hydraulic ram base to the cement floor during testing were tightened.
3. The underside camera used was a “fish-eye” type camera capable of capturing the entire underside of the panel.

Another difference in the two test sets was that the 2008 tests were completed on two panels of the same size and varying temperatures. The 2009 tests were completed on panels of differing dimensions but constant room temperature.

#### *2.2.4.1 Test Plan*

There were a total of 13 panels tested in the 2009 test sequence. These panels were divided into six different sizes: 18”×18”, 20”×20”, 22”×22”, 24”×24”, 26”×26” and 30”×30.” There were two panels of each size except for the 18”×18” panel. The reasoning

behind testing only one 18"×18" panel was due to the limited amount of material for testing as well as the fact that this size panel had been tested previously in the 2008 tests.

#### **2.2.4.2 Test Results**

A summary of results, in terms of impact energy, maximum force, and displacement at fracture, for each of the 13 tests, is provided in the table below. The results are indicative of the average values of the two panels tested for each panel size.

**Table 4: Summary of 2009 Hydraulic Ram Test Results**

<b>Panel Size (in)</b>	<b>Impact Energy (J)</b>	<b>Disp @ Fracture (mm)</b>	<b>Max Force (kN)</b>
18	1092	32.2	30.3
20	935	40.4	32.0
22	1113	40.8	34.9
24	1014	43.9	32.9
26	958	43.0	33.6
28	966	53.2	35.7
30	848	55.6	33.3

The impact energy ranged from 848 to 1113 J, the displacement at fracture ranged from 32.2 mm to 55.6 mm and the peak force ranged from approximately 30.3 kN to 35.7 kN.

#### **2.2.4.3 Deformation Pattern**

There was a distinct damage pattern difference between the 2009 test specimens in terms of the larger and smaller dimensioned panels. The smaller panels had deformation patterns concentrated in the centre of the panel while the larger panels had deformation patterns that extended to the edges of the panel in almost a straight line. Figure 13(a) and

(b) illustrate damage on the front and back of an 18"×18" panel while Figure 13(c) and (d) represent damage on the front and back of a 30"×30" panel.

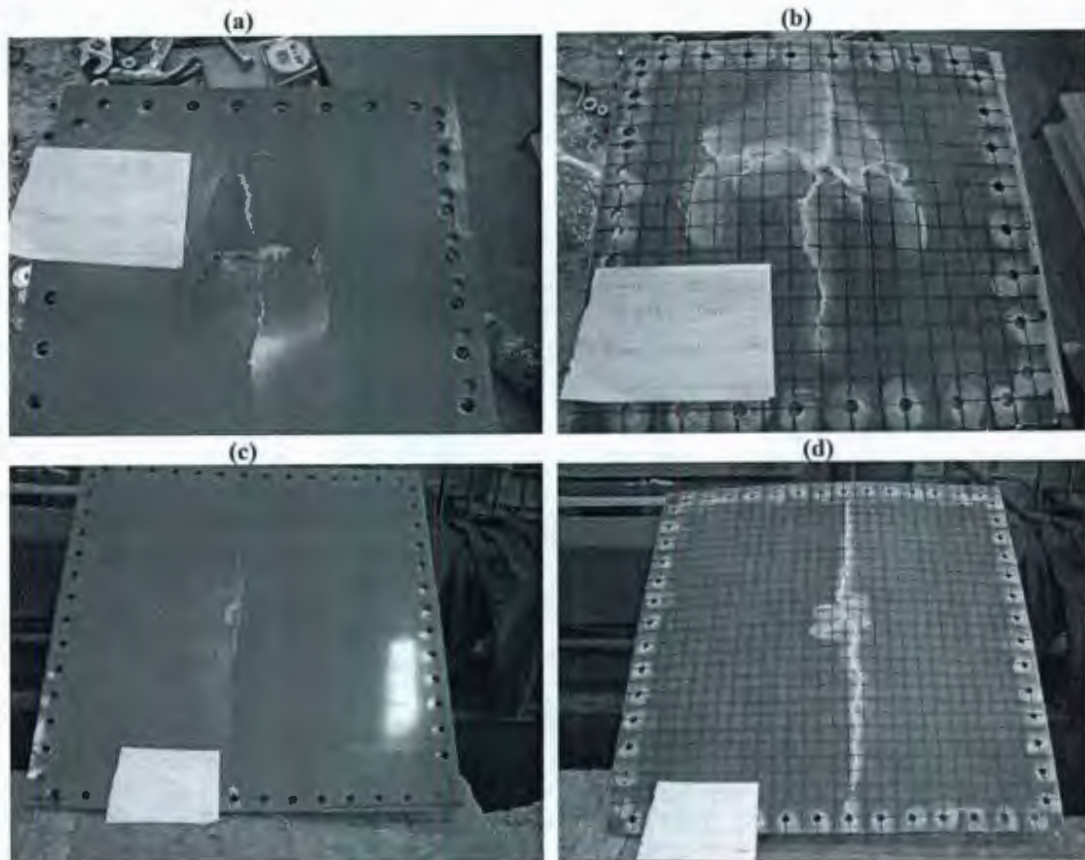
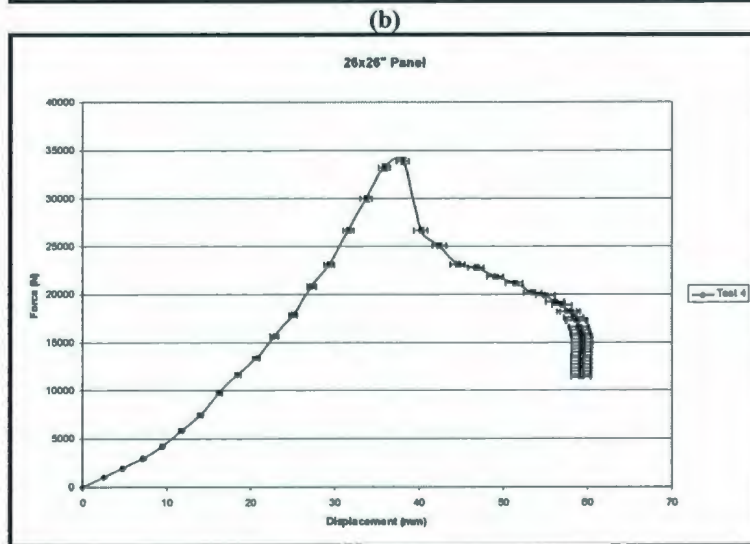
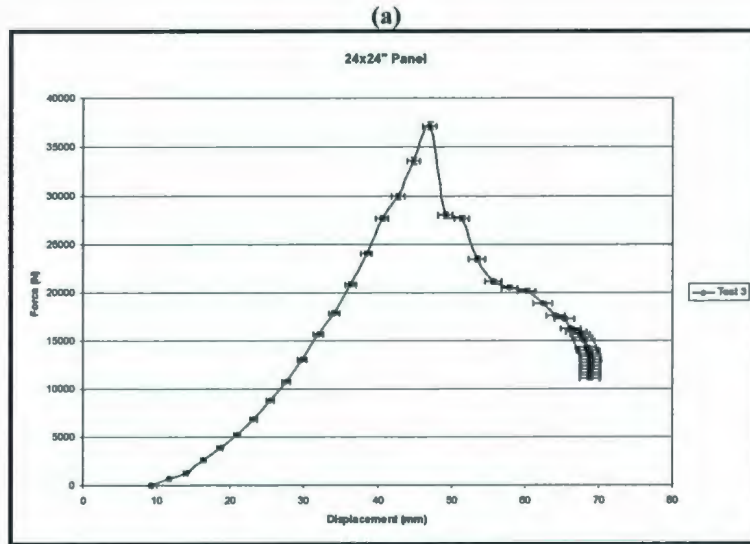


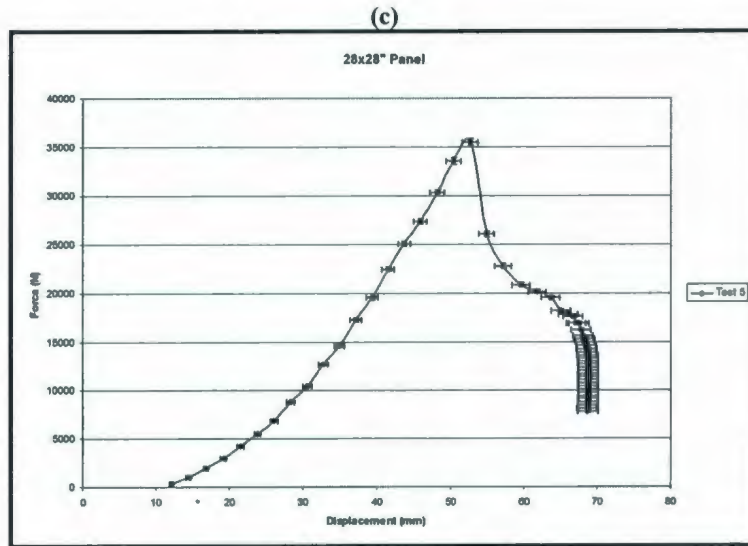
**Figure 13: 18" and 30" Deformation Patterns**

#### **2.2.4.4 Data Analysis**

The data for the 2009 hydraulic ram tests were analysed using the same procedure as the 2008 tests. The data from each of the 13 tests was plotted in terms of force versus displacement to get an idea of the maximum force, displacement and impact energy. Three of these curves are shown in Figure 14 to demonstrate the analysis process. The

force versus displacement curves for the remaining panel sizes tested in the 2009 hydraulic ram tests are provided in Appendix A.

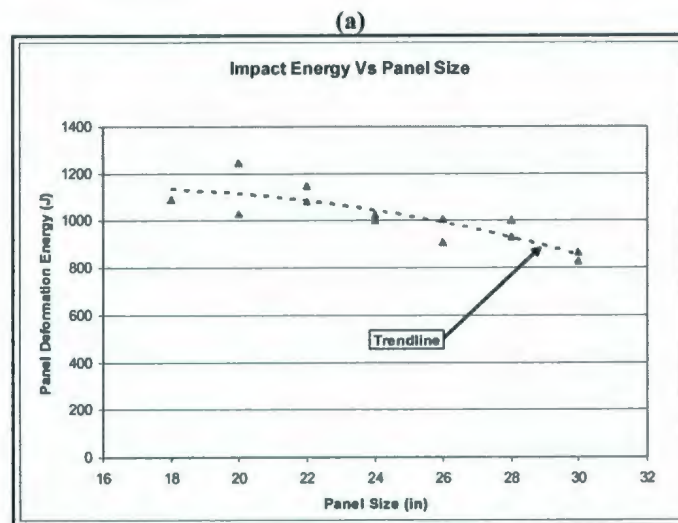




**Figure 14: 24", 26" and 28" Panel Results**

The results showed that for each panel size the maximum force was around 35 kN and the displacement at maximum force was between 35 mm and 55 mm. The impact energy was found for each of the 13 test specimens using numerical integration.

The maximum force, maximum displacement and impact energy were plotted against panel size. These plots are shown in Figure 15 (a), (b) and (c).



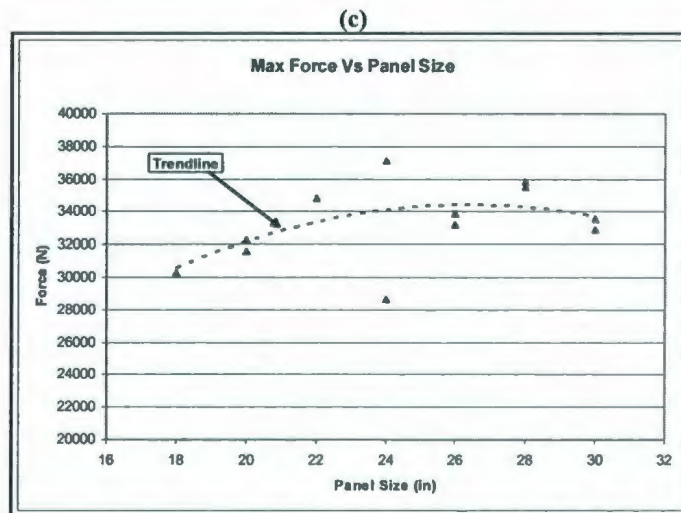
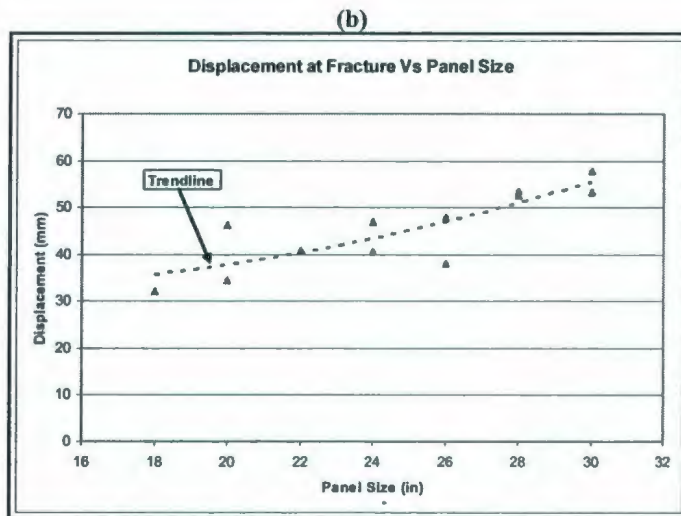


**Figure 15: 2009 Hydraulic Ram Results**

First, consider these three curves in terms of variation in panel size. It is clear that the impact energy as well as the maximum displacement prior to complete fracture were affected by changing panel size. Figure 15(a) indicated that as the panel size increased the impact energy decreased with a variation of approximately 300-400 J between the largest and smallest panels. Figure 15(b) indicated that increasing panel size had the opposite effect on maximum displacement. As the panel size increased the maximum displacement

also increased significantly. The impact of varying panel size on the maximum force was less clear as illustrated by Figure 15(c). However, a peak was reached at a panel size of 24" with lower values for smaller and larger panels. The values for maximum force are all in the same range between 28 kN and 38 kN.

### ***2.2.5 Comparison of 2008 and 2009 Tests***

There were a number of differences between the results of the 2008 and 2009 tests. Some variation was due to the changes in test set up. Another probable source of variation relates to the different material types tested. The replicated and actual lifeboat material reacted similarly to tensile loading as shown by the results of the tensile tests. Despite the fact that the two materials behaved similarly to tensile loading, they may not have reacted the same to impact loading.

The panel deformation pattern of the 2009 tests was substantially different from the deformation pattern encountered with the 2008 tests. The 2008 test pattern distinctly outlined the impact head while the 2009 test deformation pattern did not appear to be affected by the geometry of the impact head. Figure 16(a) represents the typical deformation pattern observed during the 2008 hydraulic ram tests and Figure 16(b) represents damage from the 2009 tests.

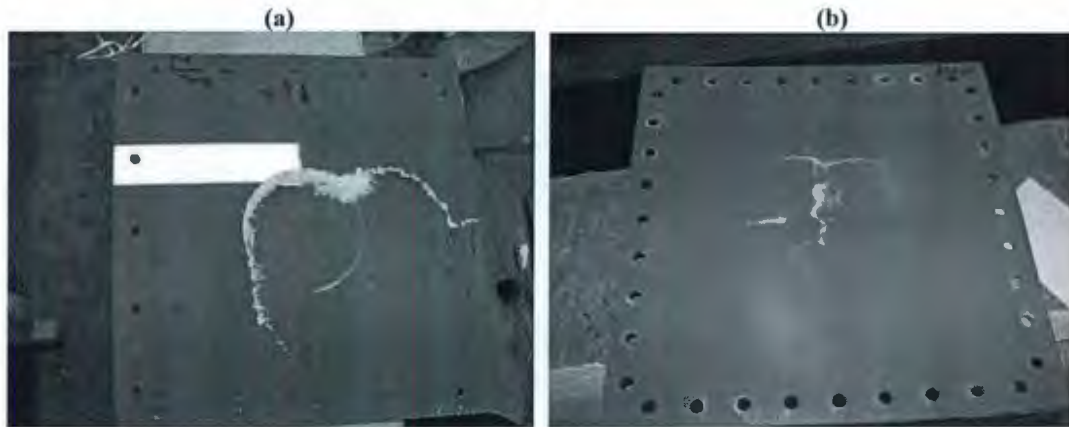


**Figure 16: Comparison of 2008 and 2009 Test Deformation Pattern**

The deformation pattern observed in the 2009 tests did not follow the contour of the ram head thus suggesting that the use of a hemispherical impactor was successful.

The underside view of the panel was entirely visible in the 2009 tests as opposed to the partial view in the 2008 tests. The 2009 tests used a different type of camera to capture video underneath the panel. The “fish-eye” camera had the capability to capture a broad area at a short focal distance. Images from the 2008 and 2009 tests are shown below. The picture on the left corresponds to 2008 testing while the photograph on the right illustrates the 2009 testing.

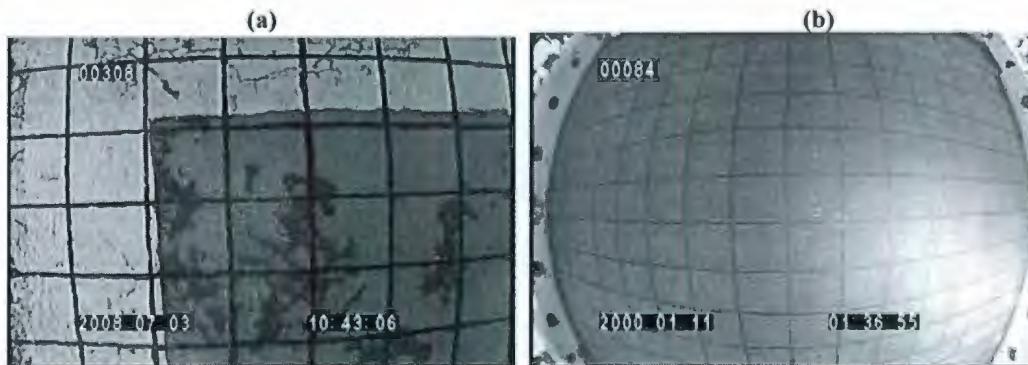


**Figure 17: Comparison of 2008 and 2009 Test Underside Camera**

The grid size on the laminate was the same for the 2008 and 2009 tests (1"×1"). In Figure 17(a) only 7"×5" was visible. The full panel size was 18"×18" and therefore the visible section was only a small portion at the centre of the panel. The figure to the right shows the entire underside of the 18" ×18" panel. The image was distorted because the camera used was of the fish-eye type.

There was a large difference in terms of maximum force and displacement values between the 18"×18" room temperature panel tested in the 2008 tests and the same size panel tested in the 2009 tests. However, the impact energy was similar. The force versus displacement plots for the 18"×18" panel in 2008 and 2009 testing are shown below. Notice that the maximum force encountered in the 2008 tests was between 70 kN and 80 kN. When this same panel size was tested in 2009 the maximum force was only around 30 kN. The displacement at maximum force of the 2008 test was approximately double that of the 2009 test with values of approximately 30 mm and 60 mm respectively. Despite the variation in maximum force and displacement the impact energy was similar with values of 1002 J and 1092 J for 2008 and 2009 tests respectively. This was due to the shape of the curve. The amount of deformation between force peak and ultimate panel failure was much greater for the 2009 than the 2008 test.

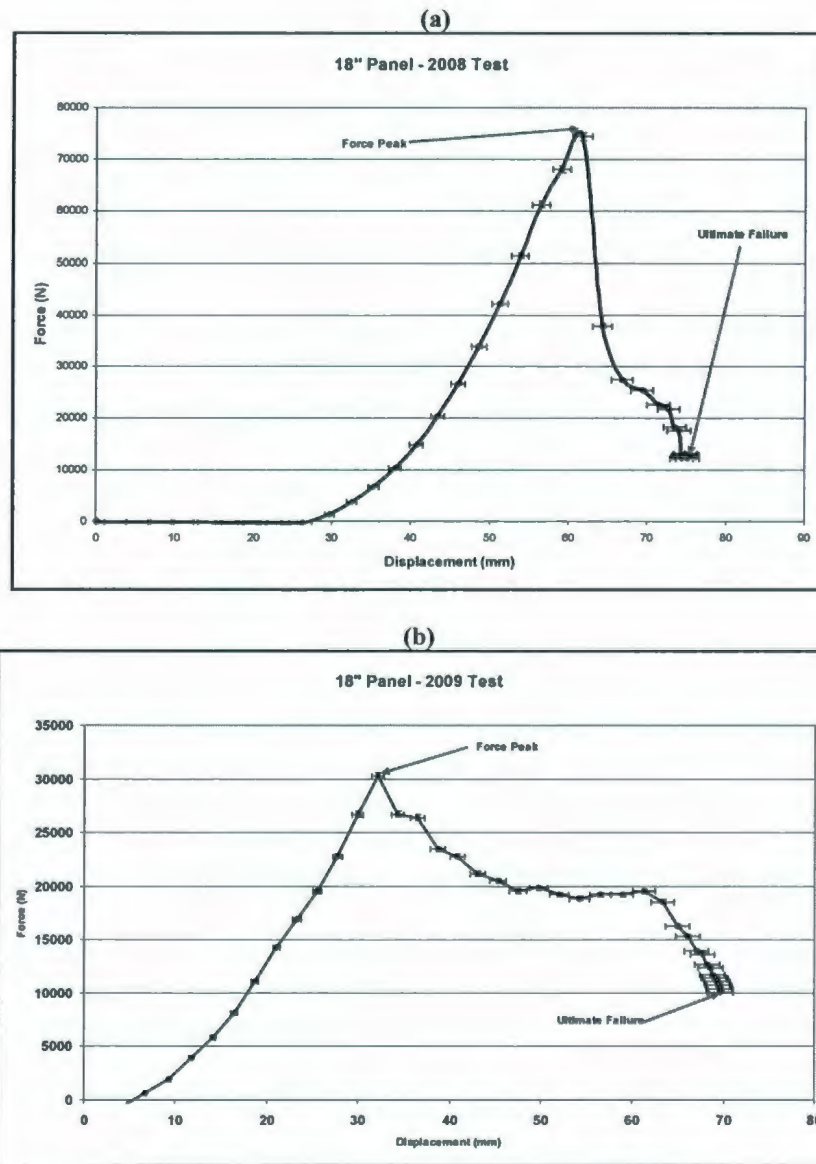


**Figure 18: Comparison of 18" x 18" Panel Results**

One possible explanation for the large variation in results is that the panel material for each test was different. The 2008 panels tested came from an actual lifeboat while the 2009 panels were fabricated to replicate the original panels. Another source of discrepancy could be the variation in hydraulic ram impact heads.

### **2.2.6 Conclusions**

The main findings from the analysis of the 2008 and 2009 hydraulic ram tests are outlined below. These conclusions are all related to the impact behaviour of lifeboat fibreglass.

1. The temperature of the panels did not have a significant effect on maximum force.
2. Panels tested at lower temperatures had higher maximum displacement.
3. A change in panel temperature significantly affected the impact energy relating to ultimate failure of fibreglass.
4. An increase in panel size resulted in an increase in the maximum displacement of fibreglass prior to fracture.
5. An increase in panel size lead to a decrease in panel failure energy.
6. Panel size variation had a negligible effect on maximum force.
7. Impactor shape affected the panel deformation pattern.
8. Replicated lifeboat laminate panels differed from actual lifeboat panels in terms of maximum impact force and displacement, but were similar in terms of panel failure energy.

### 2.3 Pendulum Tests

A set of experiments were designed and conducted using a modified 20-person TEMPSC. The lifeboat modifications included the installation of port and starboard acrylic impact panels in the hull. These panels were mounted on force dynamometers in the bow area of the TEMPSC. To accommodate the panels and force dynamometers, two sea chests were manufactured and incorporated into the hull structure. These sea chests were waterproofed and sealed to the inside of the vessel, totally enclosing the dynamometers as well as internal video cameras. The figures below show an external view of the port impact panel and a view of the starboard sea chest.

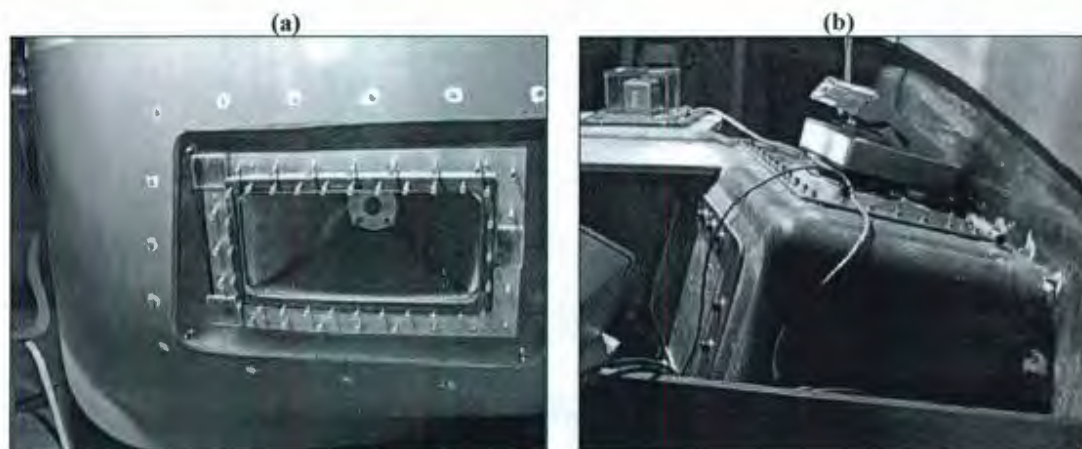


**Figure 19: Acrylic Panel and Sea Chest**

The experiments involved suspending ice spheres from a line acting as a pendulum. The sphere was then set at a specified angle, and allowed to freefall in the pendulum's natural arc until impact with the panel.

### **2.3.1 Test Objectives**

There were four main objectives of the pendulum tests. The first was to calibrate ice loads for field conditions. The second was to ensure that the modified lifeboat was prepared for field trials. The third objective was to assess the relationship between panel energy and impact energy. The final objective was to determine a component required to semi-empirically model the lifeboat impacting ice, specifically the coefficient of restitution.

To meet the objectives a test plan was developed in which 33 tests were planned for impacts at different locations on the acrylic panel and from various drop heights. Tests were also completed on both sides of the lifeboat. At the time of testing only the port acrylic panel had a working dynamometer while the starboard side was fitted with a dummy dynamometer. The purpose of impacting the starboard side was to determine the force reading on the working dynamometer of an impact to the opposite side.

### **2.3.2 Test Set Up**

The lifeboat was braced using a strap over the bow which was secured to two wedge-shaped supports on either side of the vessel. The strap was tightened to limit the motion of the lifeboat upon impact. The support wedges were located in close proximity to the hull to restrict motion and were of sufficient weight to hold the lifeboat in place. The lifeboat support system is shown in Figure 20 below.



**Figure 20: Lifeboat support system**

Twelve sand bags weighing 22.7 kg (50 lbs) each were positioned inside the lifeboat for added support during impact. The lifeboat was placed on chocks rather than remaining in its trailer, also contributing to stability during impact.

The main frame support for suspending the pendulum consisted of four 5.0 m x 0.30 m steel I-beams. These beams were set up in a rectangle and braced with rails that spanned the length of the two sets of beams. At the far sides of the set up there were two square columns that extended across the width of the two I-beams. The forward column supported the pivot of the pendulum and the aft column supported a winch system for raising the ice sphere prior to drop. The aft column was located at a greater height up the I-beams to allow the ice sphere to be raised to the required height.

The frame was placed perpendicular to the panel being tested to ensure that the ice specimen would impact normal to the panel and limit sliding or scraping along the panel.

The majority of the tests were conducted on the port side of the boat. The impacts to the starboard side were conducted after all impacts to the port side were completed. To impact the starboard side, the test set up was moved using a large overhead crane.

The ice spheres used as impact objects in these tests were grown as two independent halves and then frozen together with a metal rod in between. At one end of each rod there was an eye hook and at the other end, there was a flat plate with a bolt pattern. The ice was frozen around the metal bar such that the eye hook protruded from the bottom and the flat plate was flush with the top. The eye hook was used as means of raising the ice sphere prior to release while the flat plate was used to bolt the line to the ice sphere. When the ice specimens were fully frozen they had shape imperfections, so an ice carving knife and chain saw were used to carve the specimens into a sphere shape. The figure below illustrates this process.



**Figure 21: Ice sphere carving**

During the planning stage of the experiment, a pulley system was included to hoist the specimen as well as enable a quick release. This proved to be too physically demanding for a person to hoist a 90 kg ice sphere to the desired release angle. There were also concerns that the quick release system would require a significant force, which could potentially skew the path of the pendulum, resulting in an off target impact. As a result of these concerns, a motorized winch was used to raise the ice sphere, and a line was cut as the release. The line can be seen in the figure below, which includes the harness that was used to hold and hoist the ice sphere.

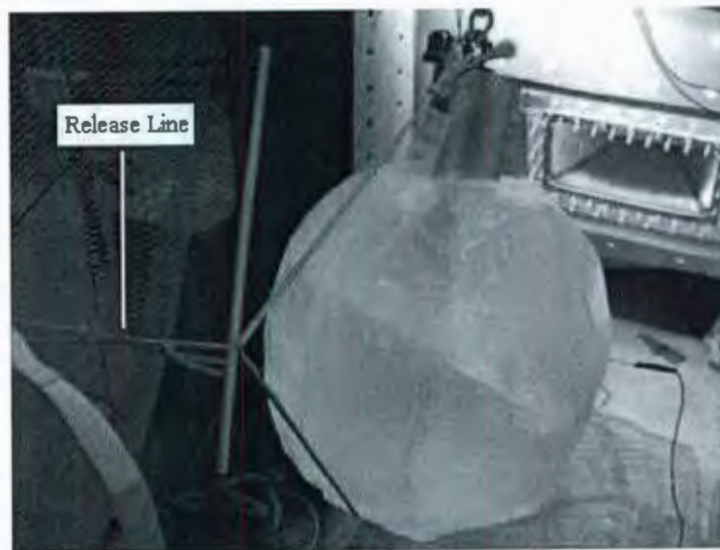


**Figure 22: Ice sphere hoisted to required drop angle**

A digital inclinometer was used to ensure that the ice sphere was raised to the correct angle prior to each release.

### **2.3.3 Instrumentation**

A right hand coordinate system was used for the lifeboat in which the  $x$  direction runs positively along the length of the boat towards the bow, the  $y$  direction runs positively across the beam from starboard to port and the  $z$  direction is in the vertical direction with positive direction upwards. Since the ice is free to rotate as it swings it is necessary to define a second coordinate system pertaining to the ice sphere. In this coordinate system the  $z_I$  axis has a positive direction upwards and the  $x_I$  and  $y_I$  axes are free to rotate in the horizontal plane.

The dynamometer inside each panel consisted of 6 U2B Force Transducers. These load cells were connected with flex links, minimizing cross-talk between the load cells. There were three load cells with 10 kN capacity, and three with 50 kN capacity. The three 50 kN load cells measured force into the panel, or across the beam of the ship. Two of the 10 kN load cells measured force along the length of the ship and the other measured the vertical force. All load cells sampled at a rate of 8000 Hz. The drawing below illustrates the port impact panel and associated load cells.

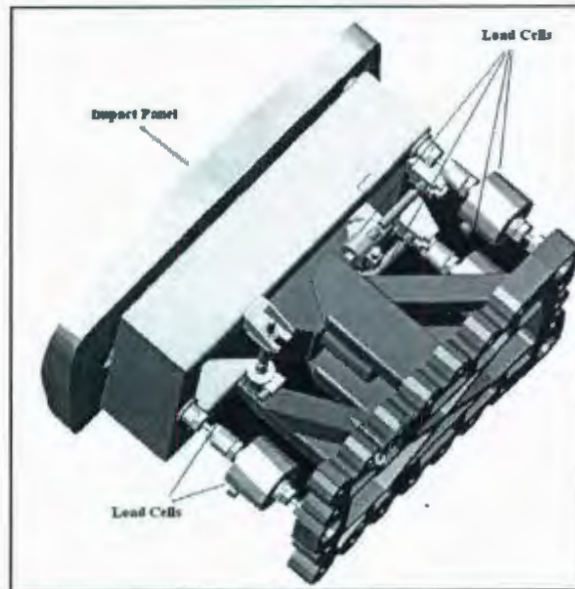


**Figure 23: Port Impact Panel and Load Cells**

Inside the lifeboat there was an inertial sensing system (MotionPak™) that measured the accelerations and rotations in the  $x$ ,  $y$  and  $z$  directions of the lifeboat. It was mounted internally on the centreline between the two sea chests. Measurements from this device can be used to determine global accelerations due to ice impact.

Mounted to each ice specimen during impact were two surface mounted micro machined accelerometers. The accelerometers were in an aluminum box to prevent damage during impact. The accelerometers were positioned 90 degrees from one another to allow for acceleration measurements in two directions ( $x_i$  and  $y_i$ ). The accelerometers are shown in the figure below.



**Figure 24: Ice sphere accelerometers inside protective casing**

There were two LVDT's (GCD-SE Series Precision Gage) used during testing to measure panel and lifeboat movement during an impact. A 0.25-inch LVDT was placed inside the lifeboat against the sea chest holding the panel that was being tested in order to record how much the panel moved during impact. A 0.5-inch LVDT was placed outside the lifeboat against the opposite panel, to record global movement of the lifeboat during impact. The 0.5-inch LVDT can be seen outside the lifeboat in the figure below.



**Figure 25: External LVDT**

A high-speed camera was used to record each impact in order to determine the contact area and impact speed. The camera was located at a position perpendicular to the impact. The camera used was a Photron Ultima APX-RS and in conjunction with the camera, an automatic trigger function was used for the first half of the testing. A Canon hand-held PowerShot S2 IS was used during the experiment to document all aspects of the procedure. The Canon camera was used to take pictures of the set up and decommission, as well as specific portions of the impacts. The Canon camera was also used to record videos of each impact. There was a Defender Security camera placed on one of the forward I-beams to record an above view of each impact, as well as a Defender Security black & white, weatherproof bullet type camera placed inside both panels, looking out of the lifeboat.

A scale was made available to weigh each ice specimen before any impact occurred. Each specimen was weighed prior to impact and again when it was either deemed too damaged to be used further, or when the specimen shattered. Each instrument, with the exception of the high-speed camera, Canon hand-held camera, and the scale were wired together, resulting in 16 data logging channels. The data files were recorded onto a laptop inside the lifeboat, which was connected via a network cable to a laptop outside the boat located at the operation station. The video from the cameras inside the panels and the security camera outside the lifeboat were stored on Secure Digital (SD) cards. The data from these cards were transferred to a computer at the operator station after each test.

#### **2.3.4 High Speed Camera Calibration**

Before the high-speed camera could be used, it was calibrated so that it would capture each impact in its entirety. To calibrate the camera, a foam sphere was hung from a pendulum and swung into the lifeboat. The camera recorded impacts with the foam sphere while adjusting location, frame rate (fps) and the resolution (pixels) in the camera settings. The camera was also calibrated for automatic start using a color triggering technique. The camera began recording when a color contrast appeared in the view.

A number of trial runs were completed until the camera was adjusted so that the impacts were fully recorded. The frame rate was initially set to 1000 fps. During test set 4, which will be elaborated upon in the next section, the frame rate was reduced to 500 fps. The resolution of the recording was 1024×1024-pixels throughout the experiments. An example of the quality of video recorded is shown in the illustration below which represents an ice specimen prior to and after an impact. The videos were saved as a series of jpeg images as the movie files were extremely large. The jpegs can be viewed as a movie using the program Midas Player.

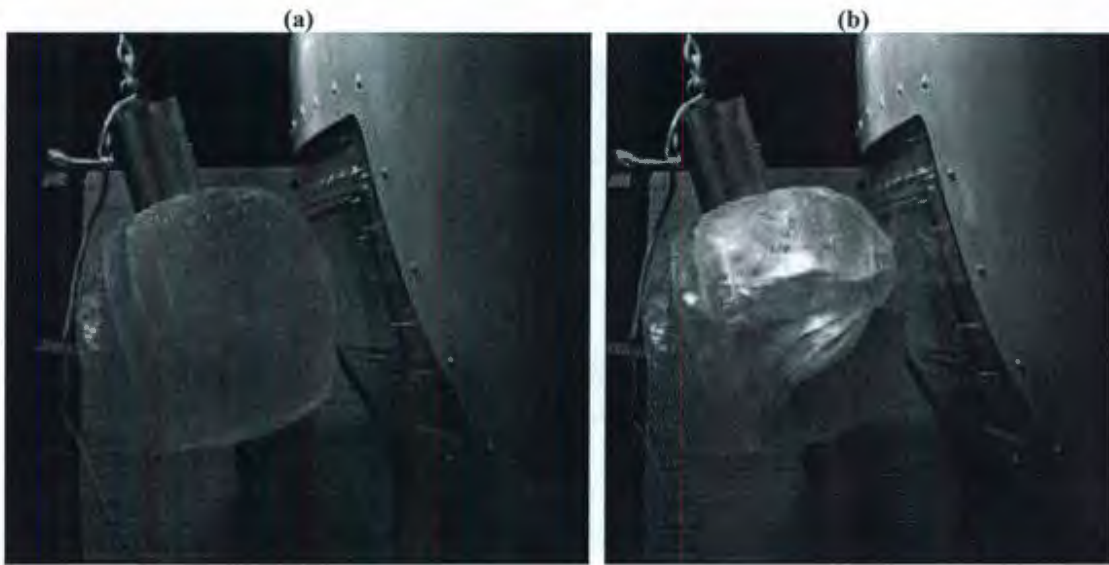


Figure 26: High speed camera images

### **2.3.5 Testing Procedure**

A total of 33 tests were performed with 9 ice specimens. Specimens were stored in a cold room and brought to the lab as needed, in order to maintain a similar temperature between specimens. Upon arrival, a hole was drilled into the ice specimen, and a probe was inserted to measure the temperature approximately 7.6 cm (3") below the surface of the ice. Next, the ice sphere was weighed and then brought to the center of the frame to attach the accelerometer box and pendulum. The figure below illustrates the accelerometer box as it was fitted to the ice sphere.



**Figure 27: Accelerometer box fitted to ice sphere**

After the accelerometers were attached, the ice was raised and connected to the line. The length of the pendulum was 2.0 m from the center of the specimen to the pivot point. The specimen was then raised to the desired angle. When the specimen was at the specified angle, the drop angle was recorded using an inclinometer. The temperature of the specimen was taken again just prior to release.



**Figure 28: Drop angle measurement**

The ice sphere was allowed to swing into the panel and was then restrained after impact to avoid the specimen hitting the panel a second time. After impact the panel was inspected visually, and the testing team verified whether or not the impact had been recorded by checking the data recordings. If the specimen had shattered, the largest pieces were weighed to compare with the initial weight. This was done so that the impact energy for the subsequent test could be determined. If the specimen was intact, it was rotated to a surface free of previous impacts. The ice specimen was then re-set to be used in a subsequent impact.

### **2.3.6 Test Plan**

Four sets of tests were conducted during the pendulum experiments. Test set one included three impacts in the center of the port panel, at a drop angle of 20°. These tests were performed while adjusting the DAS filters, to find the optimal setting. The favourable filter setting was found to be 8000 Hz for the load cells and 800 Hz for the other instruments. The optimal sampling rate for the data was found to be 50,000 Hz. These values were set and used throughout the remaining tests. Test set two included impacts in the centre of the port panel at various release angles. This was done to obtain a range of dynamometer readings that could be compared with the theoretical impact values to confirm dynamometer accuracy. Test set three involved impacts at critical points forward and aft of the centre of the acrylic panel. The impacts were aligned to occur directly on the load cells. The purpose of this test set was to compare dynamometer readings versus theoretical force values for an impact directly on a load cell. Test set four included

impacts in the centre of the starboard side. This was performed in order to determine the force reading resulting from a theoretically known impact force on the opposite side of the vessel. In other words, the effect of an impact on the starboard side was recorded on the port side.

### **2.3.7 Data Calibration**

Prior to analysis of the collected data files, each file had to be calibrated. The calibrations for all of the pendulum test data were completed using a calibration program called DataLoggerCal. This was a calibration program developed by the Institute for Ocean Technology. The calibration file containing the calibration coefficients for all of the instrumentation was put into the program along with the file to be calibrated. This automatically calibrated the required data against the input calibration values using a linear calibration.

The calibration file contained slope and offset values for each set of measured data. For example, each of the two LVDT's had separate slope and offset values. To determine the calibration values each instrument was calibrated using five calibration points. The data acquisition system recorded the measurements in counts. As an example of the calibration process, the 0.5 inch LVDT will be discussed. To determine the slope and offset of the calibration curve for this instrument, the LVDT was displaced some known distance and the corresponding count value was recorded. Then the LVDT was displaced at four higher

known values and the count values were recorded. The count versus displacement was subjected to linear regression from which the offset and slope was found.

Once all instruments were calibrated, the recorded data (in counts) were compared to the calibration line to determine the measurement in physical units i.e. length, acceleration and force. The calibration file used for the pendulum tests is shown below. This table also provides a description and labelling scheme for each channel.

**Table 5: Calibration Table**

<b>Channel Number</b>	<b>Description (Channel Label)</b>	<b>Unit</b>	<b>Slope</b>	<b>Offset</b>
1	Load cell oriented in z-direction ( $F_{z1}$ )	N	0.298	-9.79E03
2	Load cell oriented in x-direction ( $F_{x1}$ )	N	0.297	-9.75E03
3	Load cell oriented in x-direction ( $F_{x2}$ )	N	0.296	-9.69E03
4	Load cell oriented in y-direction ( $F_{y1}$ )	N	1.48	-4.84E04
5	Load cell oriented in y-direction ( $F_{y2}$ )	N	1.48	-4.84E04
6	Load cell oriented in y-direction ( $F_{y3}$ )	N	1.48	-4.85E04
7	Accelerometer located on ice sphere ( $A_{x1}$ )	g	2.01E-02	-657
8	Accelerometer located on ice sphere ( $A_{y1}$ )	g	2.02E-02	-659
9	Inclinometer in Lifeboat ( $I_x$ )	deg/sec	1.88E-03	-61.7
10	Inclinometer in Lifeboat ( $I_y$ )	deg/sec	1.89E-03	-61.8
11	Inclinometer in Lifeboat ( $I_z$ )	deg/sec	1.91E-03	-62.5
12	Accelerometer in lifeboat ( $A_x$ )	g	6.70E-04	-21.9
13	Accelerometer in lifeboat ( $A_x$ )	g	6.71E-04	-21.9
14	Accelerometer in lifeboat ( $A_x$ )	g	6.73E-04	-22.1
15	Internal LVDT (0.25" LVDT)	inch	7.48E-06	-0.245
16	External LVDT (0.5" LVDT)	inch	1.48E-05	-0.484

### 2.3.8 Results

Below is a summary of the results from the pendulum tests. The absolute value of the recorded measurements are presented.

**Table 6: Summary of Pendulum Test Results**

Test #	Drop Angle (deg)	Impact Point (on panel)	Impact Speed (m/s)	Sphere Mass (kg)	Peak Force (Y) (N)	0.25 LVDT (mm)	0.5 LVDT (mm)	Global Accel (g)	Ice Sphere Accel (g)
1	20	Centre Impact	0.5102	88.9					
2	20	Centre Impact	2.3	88.9	41187	2.91	3.73	28.91	63.30
3	20	Centre Impact	2.1	88.9					
4	15	Centre Impact		89.4	25395	1.45	1.15	22.12	40.20
5	15	Centre Impact	0.3125	89.4					
6	20	Centre Impact	1.8	89.4	34278	2.41	2.23	29.60	62.70
7	15	Centre Impact		89.4	14248	0.75	1.44	29.40	13.70
8	20	Centre Impact		89.4	28673	1.86	2.00	25.02	67.10
9	20	Centre Impact	2.3	93	38513	2.38	2.51	24.21	43.20
10	15	Centre Impact		93					
11	25	Centre Impact		93	26663	1.50	2.18	15.40	23.08
12	30	Centre Impact		93	39758	2.03	3.89	19.53	37.10
13	25	Centre Impact		93	27665	1.71	2.50	22.99	44.05
14	15	lower bow corner		94.3	17387	0.80	2.01	20.54	20.21
15	15	upper bow corner		94.3	34345	2.07	1.55	28.50	27.94
16	15	upper bow corner	1.314	94.3	17037	0.91	1.81	21.84	21.67
17	15	upper aft corner	1.4	94.3	35091	2.20	2.26	27.24	28.39
18	15	upper aft corner		94.3					
19	20	upper aft corner	1.4	94.3	29177	1.62	2.16	22.93	47.02
20	15	lower aft corner	1.3	91.2	18932	0.99	2.59	19.04	32.13
21	15	lower aft corner	1.3	91.2	17276	0.92	2.46	14.91	29.63
22	15	Centre Impact	1.2	91.2	20910	1.09	2.56	16.66	23.64
23	20	Centre Impact	1.8	91.2	28147	1.53	1.83	14.01	35.76
24	30	Centre Impact	3.45	91.4	40637	2.44	3.55	21.39	45.47
25	25	Centre Impact	2.619	91.4	37207	2.09	3.12	19.69	46.27
26	20	Centre Impact	1.7	91.4	15848	0.73	1.33	6.97	43.47
27	30	Upper Centre	3.14	45.4	28603	1.68	2.10	20.03	76.54
28	15	Upper Centre	1.2	45.4	9193	0.41	0.44	7.98	34.54
29	20	Centre Impact		45.4	20641	1.27	2.73	16.48	51.18
30	25	Centre Impact	2.365	45.4	20825	0.97	2.35	12.16	45.27
31	20	Centre Impact		51					
32	30	Centre Impact		51					
33	30	Centre Impact		25.5					

The peak force values provided in the table refer to the sum of the peak value from each of the three y-direction load cells. The two LVDT columns contain recordings of the peak displacements for each impact. The two acceleration columns refer to the peak resultant acceleration value for each impact. The acceleration is given in units of 'g' which represents a unit of gravity (9.81 m/s<sup>2</sup>).

The blank spaces in the Table 7 indicate that the data was not collected. The impact speed was measured using high speed camera results. Some impacts were only partially captured by the high speed camera and therefore the impact speed could not be computed. This inadequacy was due to an issue with camera triggering. The data acquisition system remote trigger failed for some of the tests. There was also an incidence of lost battery power.

The maximum recorded values in each column of Table 6 are highlighted. The maximum impact force was approximately 41 kN and resulted from a centre impact, on the port impact panel, at a drop angle of 30 degrees which corresponded to an impact speed of 3.45 m/s. The maximum local and global displacements were recorded as 2.91 mm and 3.89 mm, respectively. The maximum global and pendulum accelerations were measured to be 29.6 g and 76.54 g. Note that the maximum recorded impact force occurred during the same test as the maximum calculated impact speed. However, the maximum displacements and accelerations did not occur at the same impact.

### ***2.3.9 Validation of Results***

The results of the mounted accelerometer readings and the dynamometer readings were validated by comparing the known impact mass with the mass calculated using Newton's law and the results of overall measured force and acceleration. The equation used to calculate ice mass is shown below.

$$m_{ice} = \frac{F_{impact}}{a_{ice}}$$

**Equation 2.1: Ice Sphere Mass**

In this equation  $F_{impact}$  is the resultant force measured by the dynamometer and  $a_{ice}$  is the resultant acceleration measured by the accelerometers that were mounted to the ice piece. The process is described below for one particular case. The test considered refers to test 19, which was a part of test set number 3. This test involved an ice sphere with an initial mass of 94 kg. The impact occurred at a critical point aft of the centre of the panel and had a drop angle of 20 degrees.

The following graphs are plots to illustrate the raw data collected from this impact. Figure 29 shows the  $x_I$  and  $y_I$  accelerations that were recorded from the mounted accelerometers. The accelerations were recorded in units of gravity (g).

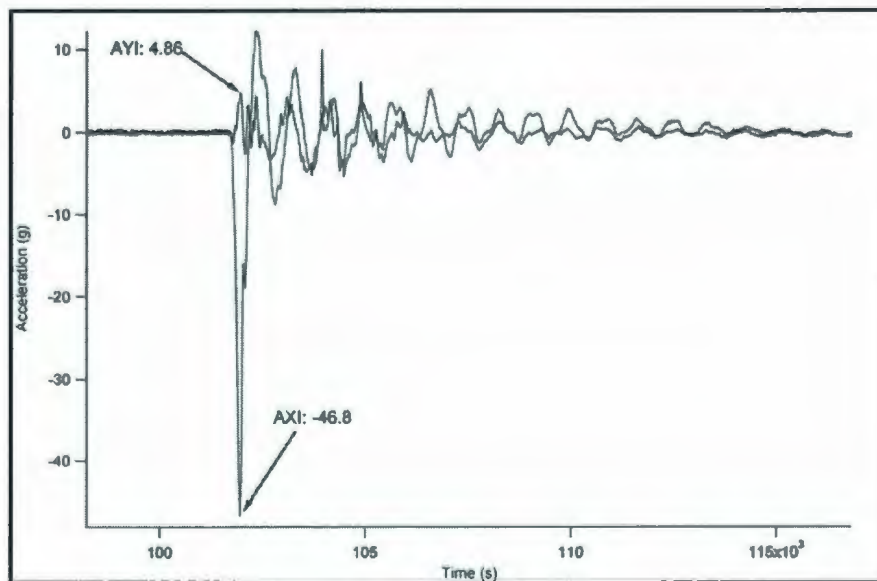


**Figure 29: Mounted Accelerometer Measurements**

The total acceleration was obtained from the sum of the squares of the accelerations measured in the  $x_I$  and  $y_I$  components. The acceleration in the  $z_I$  direction was assumed to be negligible. Figure 30 and Figure 31 illustrate the forces recorded by the three 10 kN load cells, and the three 50 kN load cells, respectively.

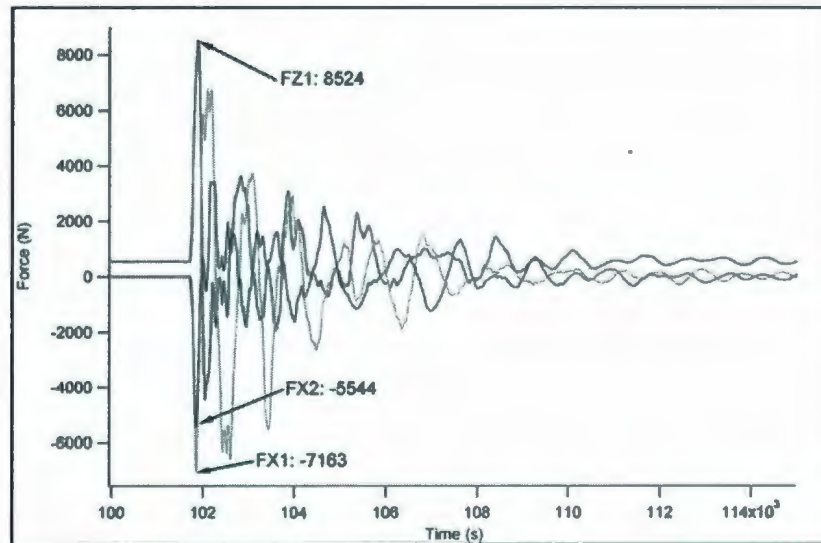


Figure 30: Load Cell Measurements – 10 kN

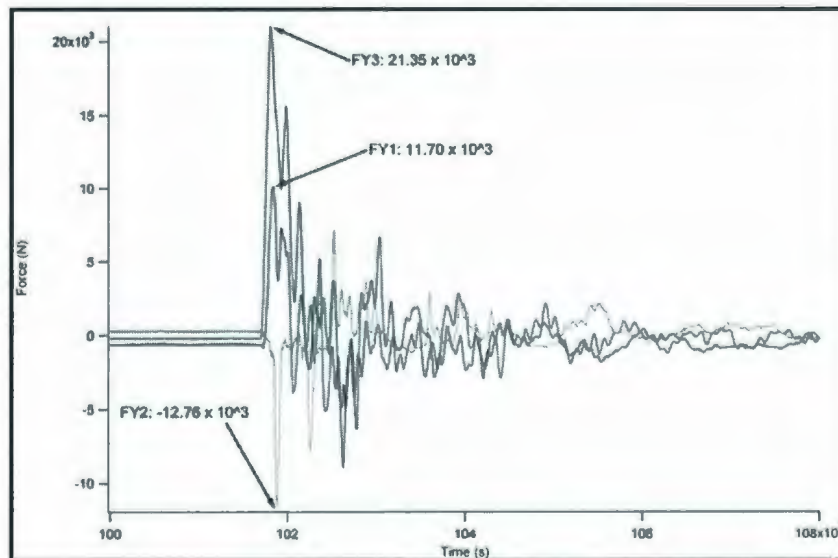


Figure 31: Load Cell Measurements – 50 kN



weight of the specimen. The percent error between calculated and measured ice sphere mass was calculated to be 7.87%. The error was calculated using the equation below.

$$\text{PercentError} = \left(1 - \frac{\text{calculated}}{\text{measured}}\right) \times 100\%$$

**Equation 2.2: Error in Mass Calculation**

The calculated error shows that the readings from the dynamometer as well as the accelerometers are less than 8%. Causes for the error could stem from noise in the dynamometer readings, rotation of ice sphere, inaccuracy in the scale used to weigh the specimen, or calculation error.

### **2.3.10 Data Analysis**

The data was analysed to find the unknowns outlined in the test objectives. Data analysis was completed using the program Igor™. The sections below detail the analysis completed on the pendulum test data.

#### **2.3.10.1 Panel Deflection Energy**

The panel deformation energy was found using the results of the 0.25", internal LVDT in conjunction with the y-direction load cell readings. The internal LVDT measured the deflection into the lifeboat, which was along the y-axis. There were three load cells that measured the force in the y-direction on the acrylic panel. The figure below shows the acrylic panel and the position of the six load cells that were behind it. The load cells

labelled  $Y_1$ ,  $Y_2$  and  $Y_3$  take force measurements in the  $y$ -direction. These were the load cells considered in the panel deflection energy analysis.

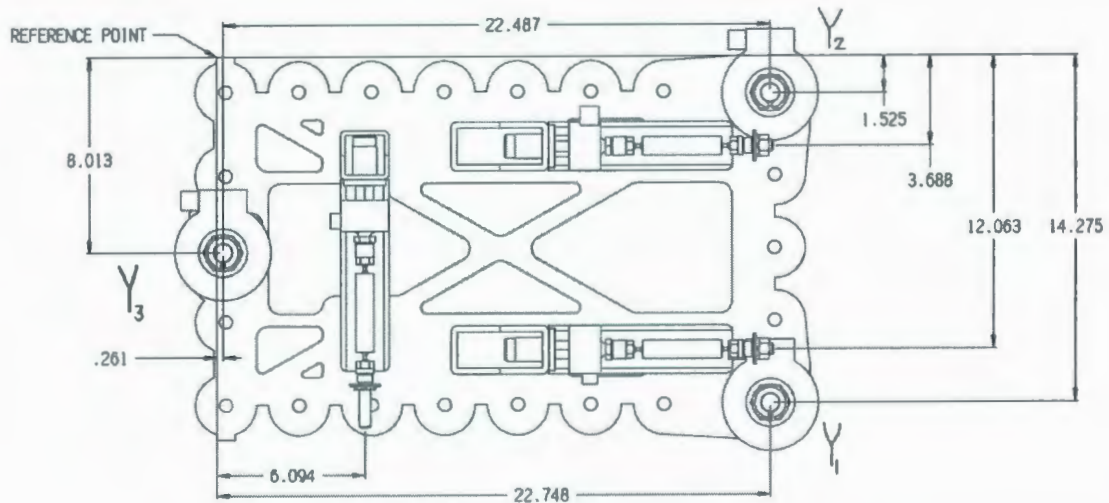


**Figure 32: Load Cell Arrangement**

The LVDT was secured against the fibreglass casing around the load cells and therefore the deflection was due to a combination of all of the forces in the  $y$ -direction. The impact energy for each test was found by integrating the area under the force versus displacement curves.

The panel deformation energy was found for four tests that each had varying impact energies so that a function could be found describing the panel energy versus impact energy. The following plot shows a summary of the panel deformation analysis. The trend line adequately describes the data as indicated by the high R-squared value. Therefore, the equation presented on the graph can be used to predict the panel deformation energy for higher impact energy terms.

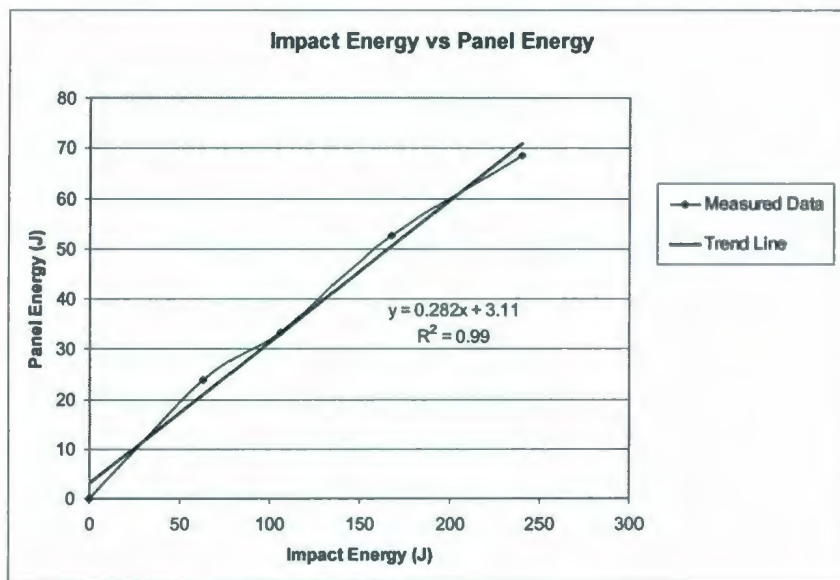


**Figure 33: Panel Deformation Analysis**

Figure 33 indicated that the energy absorbed by the panel increased approximately linearly with increasing impact energy. The impact energy involved in the pendulum tests was smaller than what would be encountered by a lifeboat impacting ice in the field.

### 2.3.10.2 Coefficient of Restitution

To determine the coefficient of restitution, the ratio of ice velocity after the pendulum swing impact to the velocity prior to impact was studied. This ratio was found for a range of impact energy values in order to determine the pattern of the coefficient of restitution with increasing impact energy. The lifeboat was impacted at four different drop angles: 15, 20, 25 and 30 degrees. The speed prior to and after each impact was found using the high-speed video for each drop. Behind the impact there was a 100 mm × 100 mm grid, which enabled a distance measurement.

The high-speed video was analysed using the program Midas Player. This program has the ability to play jpeg files and allows the user to start and stop the video as needed. To find the distance travelled by the ice sphere, the initial position was marked on the high-speed video, then the video was advanced a known number of frames and the final position was marked. The initial ice sphere position corresponded to a horizontal and vertical pixel value. This was the same for the final position. The grid was used to determine an actual distance to which a change in pixel values corresponded. To do this, the marker was placed in the corner of one block of the grid and the pixel values were recorded. Then the marker was moved to the opposite corner of the same block and the pixel values were recorded. This provided a scale factor as to how many horizontal and vertical pixels corresponded to 100 mm. The distance travelled by the sphere was taken as the trajectory of the travel. This was estimated using the  $x$  and  $y$  components of the distance.

The frame rate of each test was known, enabling a time computation, which was required to calculate the velocity. The number of frames the video advanced divided by the frame rate results in the time taken to travel the given distance. The distance was divided by the time to get the speed prior to and after impact. Refer to Figure 26(a) and (b) for high-speed camera images that illustrate the ice sphere directly prior to and directly after collision.

The coefficient of restitution was found as a function of increasing impact energy. The results showed that at low impact energy values, the coefficient of restitution was at the highest point and then as the impact energy increased the coefficient of restitution levelled off to a value of approximately 0.2. A plot of the coefficient of restitution versus the impact energy is shown below.

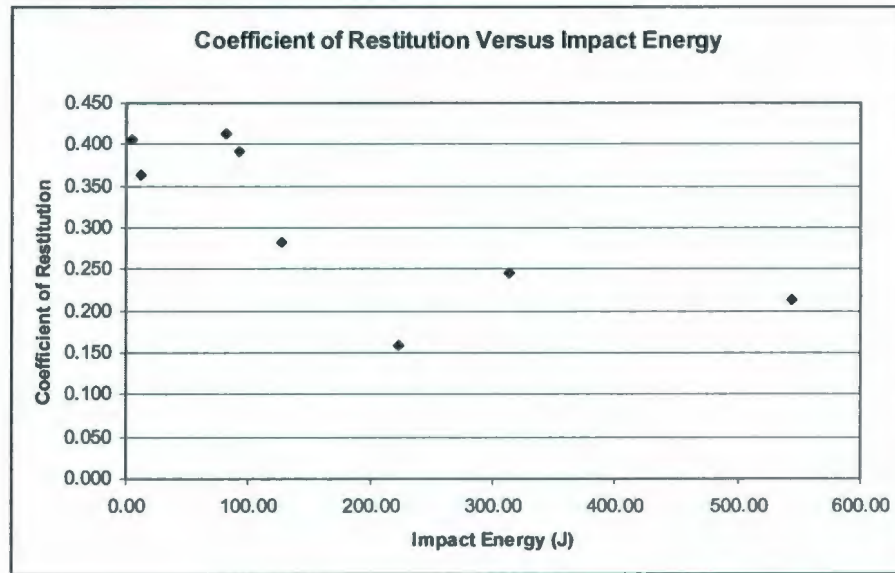


Figure 34: Coefficient of Restitution Analysis

### 2.3.10.3 Global Energy

Throughout the pendulum testing the lifeboat was strapped to two large metal frames to ensure that it would not move globally as a result of the impacts. To test the effectiveness of this system the global energy at each drop angle was found and then compared to the impact energy for that test. The percentage of global energy to impact energy was calculated for each test considered in the global energy analysis.

Tests 2, 14, 27 and 30 were randomly selected for the global energy analysis. Each of these tests had different impact energy values. To determine the global energy the global displacement was multiplied by the global force component in the direction of displacement. The global displacement was measured with the 0.5" LVDT, which was mounted externally on the acrylic panel opposite to impact. The global force was found by adding the force readings of the three load cells in the dynamometer that were oriented in the  $y$ -direction.

The global displacement was found by taking the 0.5" LVDT reading prior to impact and subtracting from it the 0.5" LVDT reading after impact. Note that points both prior to and after impact were taken from the stable data range in which there were no more oscillations. Figure 35 represents the 0.5" LVDT recordings for pendulum test number 2. The square marker was set just prior to the point of loading while the circular marker was set at the maximum displacement due to loading. The elastic displacement of the vessel could be observed from the difference in  $y$ -coordinates of the circle and square markers. The total elastic displacement was about 3.7 mm. The letter  $A$  on the curve represents the global displacement of the lifeboat as a result of the impact. The global displacement was found by subtracting the  $y$ -coordinate of a point on the stable curve after impact from the  $y$ -coordinate of the square point. The global displacement was found to be 0.20 mm.

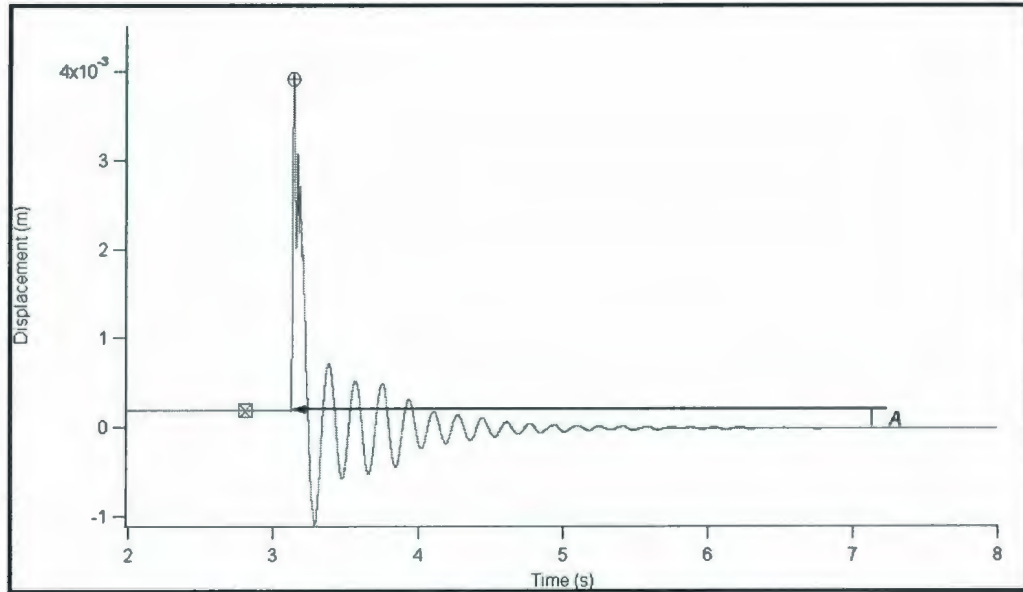


**Figure 35: Global Displacement - 0.5" LVDT Measurement**

The initial impact energy for each selected test was approximated based on theoretical speed and the known impactor mass. The equations used to calculate the impact speed and to determine the initial impact energy are shown below.

$$v_{theoretical} = \sqrt{2gL(1 - \cos\theta)}$$

**Equation 2.3: Impact Speed**

$$E_{impact} = \frac{1}{2}mv_{theoretical}^2$$

**Equation 2.4: Impact Energy**

The global energy as a percentage of initial impact energy for each test is shown in the table below.

**Table 8: Global Energy Percentages**

<b>Test #</b>	<b>Drop Angle</b>	<b>Global Energy %</b>
14	15	0.83
2	20	7.7
30	25	0.13
27	30	0.87

The results indicated that the global energy was negligible for all tests except test #2. This test had the global energy making up approximately 7.7% of the initial kinetic energy of the collision while the rest of the tests had a global energy percentage of less than 1%. To determine if the test 2 result was an outlier or inaccurate, another test with a drop angle of 20 degrees was analysed. The result of this test, test 26, indicated a global energy percentage of only 0.09%. This suggested that the result of test 2 analysis was an outlier.

A probable cause of the high percentage value for test 2 is that this test was one of the first impacts after set up. Therefore, it is likely that displacement occurred initially due to slack in the strapping of the lifeboat but then stopped when the lifeboat was pushed to the limits of the strap. The results of the global energy analysis indicated that the global energy was insignificant in terms of the initial impact energy.

## 2.4 Field Trials

Full scale trials were completed in which the IOT 20 person lifeboat was driven into pack ice and level first year ice. The purpose of these tests was to measure force magnitudes involved in ice impact, as well as to gain an understanding of lifeboat performance in various ice conditions. The results of the tests were subsequently used to help validate a mathematical model of the lifeboat operating in ice, enabling the prediction of impact forces for structurally limiting situations. The trials took place in two small bays located Triton, NL during April, 2009. The test locations are outlined on the map below and the two bays are marked as 1 and 2.



Figure 36: Field Test Location

### **2.4.1 Lifeboat**

The lifeboat used in field trials was the same TEMPSC used for pendulum testing. It was purchased from Beihai Shipyard in China. The lifeboat has an overall length of 5.28 m a maximum breadth of 2.20 m and a moulded depth of 1.10 m. The lifeboat was fabricated of single skinned fibreglass with an internal layer of polyurethane foam. The hull, inner hull and canopy were moulded as individual sections each having different thicknesses. The lifeboat had a displacement during trials of 3800 kg corresponding to a fully loaded state. It was equipped with a 29 hp engine and a three bladed propeller inside a steerable nozzle. The propeller had a diameter of 45.7 cm and a pitch of 27.9 cm. The nozzle inner and outer diameters were 19.7 cm and 20.5 cm respectively.

### **2.4.2 Instrumentation**

During field trials the lifeboat was equipped with all of the same DAS components that were used in the pendulum tests plus additional components. The additional DAS components included external video cameras, DGPS and a remote control system.

A total of six external cameras were secured to the lifeboat to get a complete view of the lifeboat surroundings, the local ice conditions and the ice impacts. There were also two internal cameras, positioned within the sea chest, for viewing the ice thickness. A digital global positioning system (DGPS) was used to take measurements of the lifeboat position, in latitude and longitude. There was an LVDT mounted behind each of the impact panels to record panel displacement caused by ice impact (at a rate of 8000 Hz).

An important feature of these trials was that the lifeboat was outfitted such that it could be driven externally using remote control. This remote system was used for a portion of the tests. The remote control system consisted of a DC powered servo which was fixed to the throttle and a linear actuator which was attached to the rudder. Both of these pieces of equipment were wirelessly connected to an external control station. The external control station contained one screen that monitored shaft rotation and throttle percentage, a second screen that showed the lifeboat camera views from the external cameras, a steering wheel to direct the lifeboat, and a set of pedals to control the speed. For these trials, the external control station was set up in the cabin of a fishing trawler that served as a standby vessel. An illustration of this set up is shown below.



**Figure 37: External Control Station**

In this figure, the lifeboat operator is manoeuvring the craft through a turning circle procedure with the aid of external controls. The lifeboat was also equipped with

instrumentation to record internal lifeboat conditions such as oxygen level, carbon dioxide level, noise level and light level. These instruments were included as part of an ongoing human factors study on lifeboat performance.

### **2.4.3 Test Plan**

Testing was conducted during April 22 to April 25, 2009. During this time, the lifeboat was tested in open water, pack ice and level ice conditions. In open water, roll decay and bollard pull tests were completed. Turning circle and zigzag manoeuvres were also conducted in open water to test the remote control operation. The results of these open water tests could also be compared to previous field testing in which the lifeboat was not equipped with either impact panels or a remote operating system to see if there are any performance differences.

In level ice, there were a series of turning circle and zigzag manoeuvres completed. There were also runs conducted at full and half throttle in which the lifeboat impacted the edge of level ice sheets. These manoeuvres were also completed in pack ice conditions. The figure below illustrates the lifeboat impacting ice at full speed.



**Figure 38: Lifeboat Manoeuvre in Ice**

#### **2.4.4 Ice Conditions**

The field trials were conducted in both level and pack ice conditions. Level ice refers to flat continuous ice and pack ice refers to broken level ice pieces. The figures below illustrate the level and pack ice cases.



**Figure 39: Level and Pack Ice Conditions**

The ice thickness was measured directly from individual pieces of ice and indirectly from observing camera images. The picture below represents a typical piece of ice encountered during trials.



**Figure 40: Typical Ice Thickness**

Figure 40 illustrates the ice thickness measured to be approximately 14 cm (5.5"). The ice thickness was also observed from cameras located inside the impact panel. The impact panel was fabricated from acrylic, which is a clear material that allowed for internal video capture of the ice thickness. The acrylic panel itself was marked with a 10 × 10 cm grid. The figure below illustrates a view of the ice through the impact panel, via the internal video camera.



**Figure 41: Internal Camera View of Ice Thickness**

Measurements indicated an ice thickness range during testing of 5 cm to 20 cm. The most frequent ice thickness encountered was 13 cm.

There were no direct measurements of ice strength taken during testing. However, there were measurements of ice temperature, salinity and conductance taken so that the ice strength could be approximated with the aid of empirical equations. These ice measurements were taken periodically throughout the first day of testing. The measured values are shown in the table below.

**Table 9: Ice Measurements**

Temperature (°C)	Salinity (ppt)	Conductance (µs)
-0.31	0.5	758
-0.32	0.3	473
-0.32	0.3	486
-0.32	0.3	544

The ice flexural and compressive strength were calculated from the measurements provided in Table 9. The equations for ice flexural and compressive strength were found using equations defined in Cammaert and Muggeridge (1988). These equations are provided below.

$$\sigma_f = 0.75 \left( 1 - \sqrt{\frac{v_b}{0.202}} \right)$$

**Equation 2.5: Ice Flexural Strength (From Cammaert and Muggeridge, 1988)**

$$\sigma_c = 1.65 \left( 1 - \sqrt{\frac{v_b \times 100}{275}} \right)$$

**Equation 2.6: Ice Compressive Strength (From Cammaert and Muggeridge, 1988)**

Both equations contain the variable  $v_b$  which is the brine volume of the sea ice. The equation for brine volume (expressed as a fraction) was described by Sanderson (1988), and is shown below.

$$v_b = 0.001 \times S \left( 0.53 - \frac{49.2}{T} \right)$$

**Equation 2.7: Brine Volume (From Sanderson, 1988)**

In this equation  $S$  is the ice salinity and  $T$  is the ice temperature. The minimum and maximum brine volume observed during field trials were calculated using the recorded ice parameters in Table 9. The brine volume values were then used to calculate the minimum and maximum flexural strength and compressive strength using Equation 2.5 and Equation 2.6. The maximum and minimum brine volume, compressive strength and flexural strength values observed during field trials are shown in the table below.

**Table 10: Ice Strength Range**

	<b>Max</b>	<b>Min</b>
<b>Compressive (MPa)</b>	1.44	1.37
<b>Flexural (MPa)</b>	0.391	0.279
<b>Brine Volume</b>	0.0796	0.0463

The mass of pack ice pieces impacted during field trials was estimated using external camera observations. The maximum ice piece dimension observed was 5.1 meters, while the smallest was approximately 0.5 meters. The ice pieces were assumed to be square from the top view and to have a thickness of 20 cm. This is the maximum ice thickness seen during field testing, but was a common thickness in the pack ice condition.

The ice piece dimension range was observed using the camera positioned to get an operator's view and the camera looking down at the lifeboat bow. The figures below represent images from these cameras.



**Figure 42: Front Camera Views**

The range of ice piece sizes was used to determine the ice mass range by multiplying by the ice density. The ice density used was  $900 \text{ kg/m}^3$ , which was estimated from ice

measurements taken during trials. The range of ice piece mass encountered during April, 2009 field testing was estimated to be 45 kg – 4600 kg.

#### **2.4.5 Results**

The data was analysed to determine impact force and speed for 139 ice collisions. The total impact force was found by adding the three peak load cell readings in the y-direction. Recall that the y-axis runs across the breadth of the lifeboat and thus the resultant force in the y-direction is normal to the impact panel. The impact speed was found using the DGPS data and refers to the forward speed of the lifeboat. The DGPS and dynamometer measurements were recorded with the same time base allowing for correlation of impact speed with impact force.

The impact position and the type of ice, either level or pack, were determined from external camera observations. The level ice cases correspond to ice having infinite dimensions. A sub-set of the data collected during field trials is shown in the table below. In this table the ice dimension refers to the maximum ice piece breadth and width. The remainder of the data is provided in Appendix B.

Table 11: Summary of Field Trial Data

Date	Impact Position	Ice Type	Ice Thickness (cm)	Ice Dimension (m)	Force (N)	Velocity (m/s)
Apr-22	Side	Pack	8	1x1.5	5168	1.9
Apr-22	Front	Pack	10	3x2.5	6342	1.9
Apr-22	Front	Pack	5	2x2.5	5541	1.9
Apr-22	Front	Pack	8	1x2.5	2762	1.9
Apr-22	Side	Pack	6	1x1.5	4377	0.4
Apr-22	Front	Level	5	Infinite	5382	2.2
Apr-22	Front	Level	7	Infinite	4121	0.47
Apr-22	Front	Pack	17	3x2	18556	2.5
Apr-23	Side	Level	7	Infinite	5725	1.6
Apr-23	Side	Pack	3	1x1	1262	0.84
Apr-23	Side	Pack	7	1x2.5	6011	2.6
Apr-23	Front	Level	12	Infinite	1637	1.1
Apr-23	Front + side	Pack	6	1.5x2	7094	2.5
Apr-23	Front	Pack	7	2x3	2935	1.5
Apr-23	Side	Pack	8	2x1.5	8225	2.6
Apr-24	Front	Level	5	Slushy	1270	2.4
Apr-24	Front	Pack	10	1x1	1185	2.6
Apr-24	Front	Pack	21	12x5	17005	2.2
Apr-24	Front	Pack	9	2x3	1943	1.8
Apr-24	Front	Pack	9	2x4	2622	1.8
Apr-24	Side	Pack	12	1x2	4840	1.6
Apr-24	Side	Pack	9	10x15	3802	1.7

The table contains ice impacts that occurred on three different days of testing. The weather during the trial period changed dramatically in terms of air temperature which may have influenced ice strength through the test period. Also, impacts on April 24<sup>th</sup> occurred in a different bay (bay 2) located close to the original test location. The impact position includes front and side impacts, corresponding to a head on collision and glancing side impact respectively. There were also cases in which the front and side of the lifeboat impact ice simultaneously.

The measured field data indicated a large variation in impact forces for collisions occurring at similar impact speeds. The first four rows of Table 11 represent impacts that occurred at identical speeds with impact forces ranging from 2762 N to 6342 N. The variation in impact force may be due to a number of factors, including ice type, ice strength, impact location, ice contact area and ice failure mode.

Recall that the forces recorded in Table 11 referred to the peak forces resulting from a collision. The peak force was found by observing the force-time history of each ice collision. The force versus time plot for one such impact is provided below. This collision occurred on April 22 and was the result of an impact with pack ice.

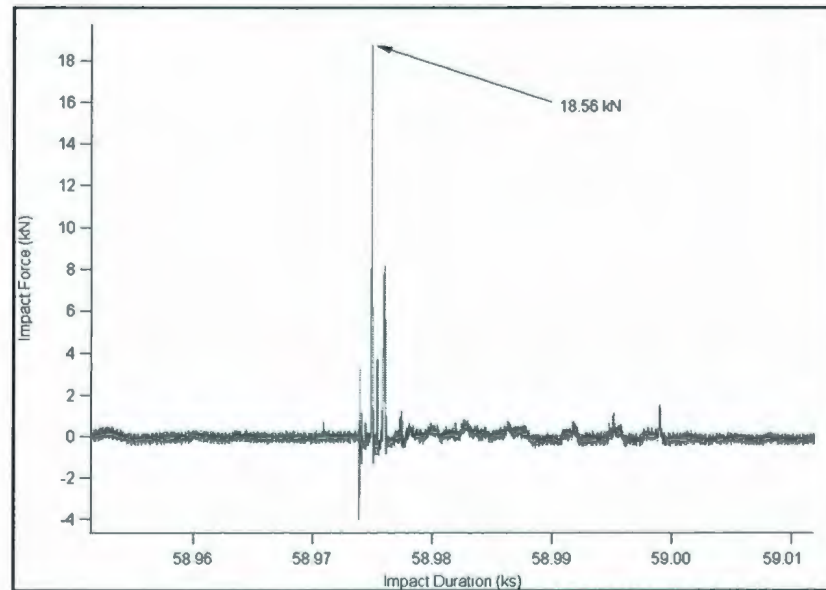


**Figure 43: Force versus Time Curve for Ice Impact**

The force recorded in the plot above is the sum of the three load cells oriented in the y direction. Note that there are multiple data peaks surrounding the maximum peak in

impact force. The data peaks subsequent to the maximum load are primarily due to additional ice contact. The data peak prior to the maximum force was due to contact with a small ice piece directly before the large pack ice collision.

### 2.4.6 Data Analysis

The measured ice impact forces were plotted against the corresponding impact speed. Figure 44 represents the impact forces encountered during field trials. The impact points are separated into pack and level ice impacts.

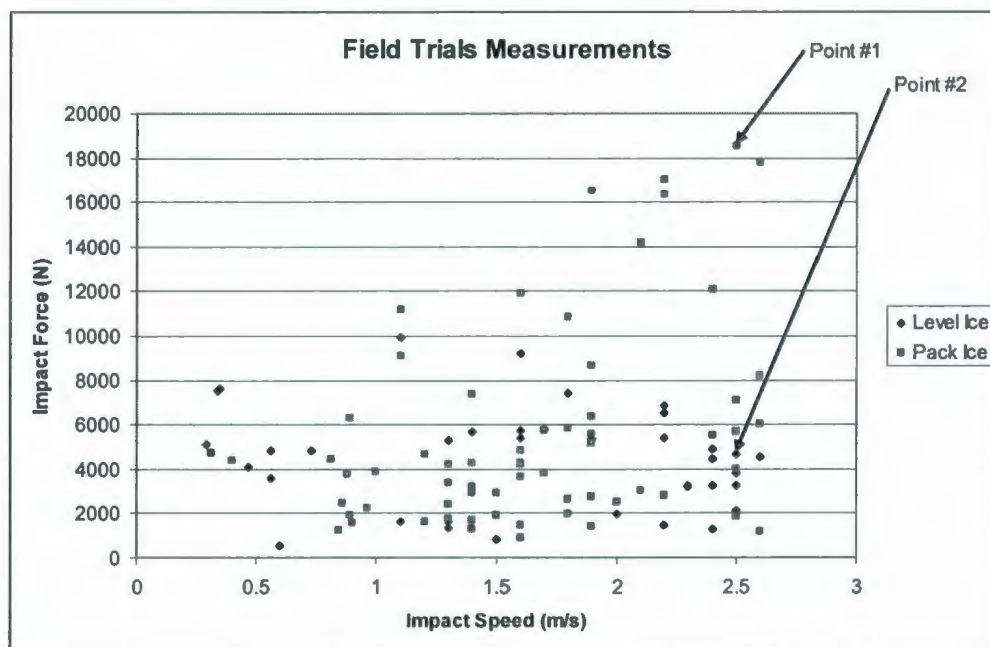


Figure 44: Field Impacts – Level and Pack

The pack ice measurements correspond to the highest measured impact forces at high impact speeds. The measured impacts appear to have a larger variation at higher impact speeds than at lower speeds. For example, at impact speeds from 0 to 1.0 m/s the ice

impact force ranges from approximately 500 N to 8000 N. For impact speeds between 2.0 m/s to 3.0 m/s the impact forces range from approximately 500 N to 18500 N. Both situations represent a speed range of 1.0 m/s however the higher speeds corresponded to an impact force range more than twice as large.

It is probable that at lower impact speeds, the limiting factor in the collision is the kinetic energy of the lifeboat; in other words, the lifeboat does not have enough energy to break ice. As impact speeds increase, the limiting factor would shift to ice strength as the lifeboat would have enough kinetic energy to promote some failure of the ice. Ice strength and failure is dependent on a number of factors, such as temperature, salinity, density and contact area. Hence, it is reasonable that at higher speeds there would be a larger variation in field trial impact forces.

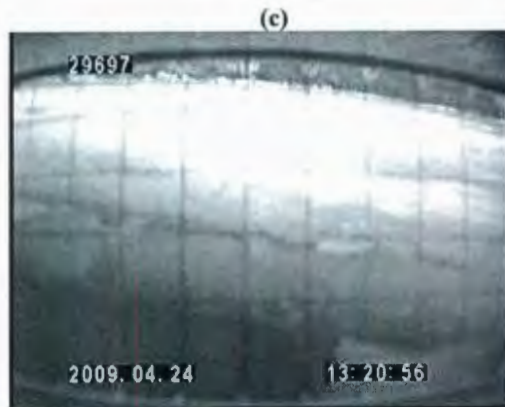
There are two impacts highlighted in Figure 44, both of which have an impact speed of approximately 2.5 m/s and resulting impact forces that differ by a factor of approximately 3.5. The impact corresponding to Point #1 caused the lifeboat to come to a complete stop. The resulting collision force had a magnitude of 18556 N. Figure 1 represented a sequential view of the interaction process for this particular ice collision. For this collision scenario the ice thickness was approximately 15 centimetres. This was found through analysis of internal video recordings.

Figure 1 (a) illustrates the lifeboat's initial contact with the ice edge. In this photo one can see the ice begin to crack as a cusp in flexure. Figure 1(b) is next in the impact time

sequence and shows that the lifeboat has progressed farther into the ice edge. The ice cusp has grown and radial cracks are apparent. The ice edge appears to be pushed under the lifeboat hull as it breaks in flexure. Figure 1(c) shows the lifeboat at a complete stop after the ice impact. The hull has advanced even farther into the ice sheet and the ice cusp has completely cracked. At this point the lifeboat does not have adequate energy to move farther through the ice.

The second impact considered, Point #2 in Figure 44, occurred on April 24 and involved a side impact of the lifeboat into level ice. The lifeboat came to a complete stop after the impact and travelled farther into the ice in comparison to the previous ice collision considered. Also, the ice seemed to be weaker with an appearance of consolidated slush. The force resulting from this impact had a magnitude of 4660 N which is approximately four times lower than the impact discussed above. Figure 45 provides internal and external camera images from this ice collision.





**Figure 45: Lifeboat Collision with Melting Level Ice**

The ice thickness was approximately the same (15 cm) for this collision as it was for the ice interaction that resulted in an impact force of 18556 N. The large variation in ice impact forces measured from these two impacts may be due in part to a variation in ice strength. The ice appeared to be weaker in the collision referring to Point #2 and the lifeboat travelled farther into the ice prior to coming to a complete stop. Another source of variation is the location of impact on the lifeboat hull. The impact location may have coincided with the load panel in one case, but not the other.

The field measurements were separated based on impact location. The plot below differentiates front impacts from side impacts.

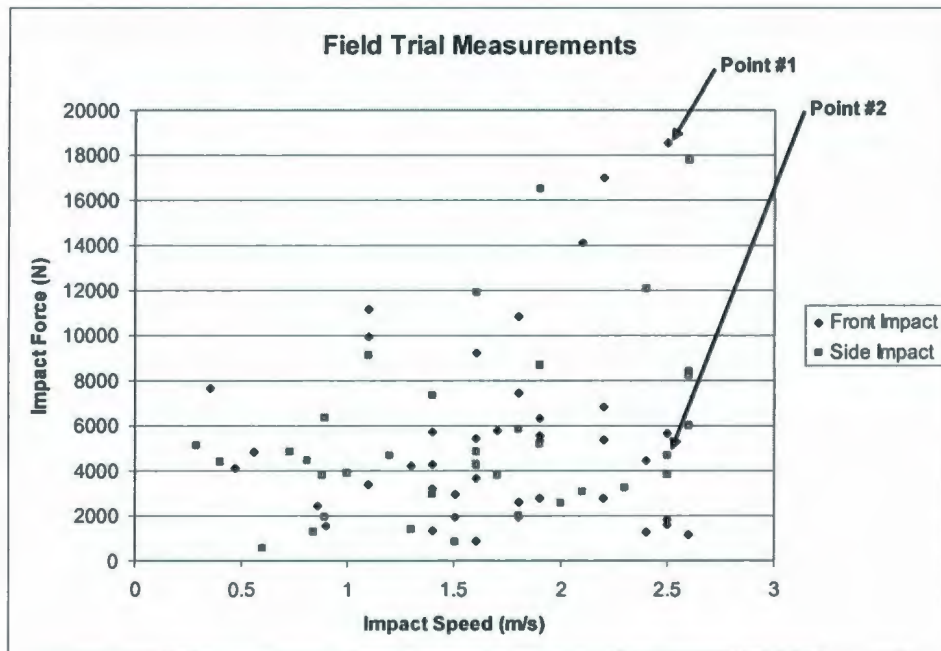


Figure 46: Field Impacts - Front and Side

Figure 46 indicates that the impacts corresponding to Point #1 and Point #2 occurred at different positions on the hull. The plot does not indicate an apparent trend between front and side impacts.

#### 2.4.7 Field Trial Comparison to Hydraulic Ram Tests

Hydraulic ram testing in 2008 indicated an ultimate load of 75 kN acting over a contact area of 0.018 m<sup>2</sup>. This is equivalent to an ultimate pressure of 4.22 MPa which represents the pressure relating to ultimate panel failure. This pressure was much larger than the pressure found from a typical ice impact in the Triton trials.

Two typical ice impacts measured during field testing were compared, in terms of peak force and contact area, to the hydraulic ram results. The first field impact occurred on

April 23, 2009 and involved the lifeboat travelling with an initial speed of 2.27 m/s and impacting a piece of pack ice on the bow shoulder area. The ice thickness was approximately 13 cm. The total force resulting from the impact was recorded as 8176 N. This force was the total of the readings from the three load cells that measured force in the y-direction. The impact area was approximated by viewing videos of the impact from different angles. The nominal contact area was approximated to be 0.039 m<sup>2</sup> relating to a nominal pressure of 0.204 MPa.

On the third day of field testing, April 24<sup>th</sup>, the lifeboat moved out of the initial test area into a nearby bay. The ice contacted on April 24<sup>th</sup> appeared harder than the ice encountered during the initial two test days. The second field impact considered for comparison to hydraulic ram measurements occurred on April 24<sup>th</sup> and involved an initial speed of 1.8 m/s, an ice thickness of 13 cm, an impact location on the bow shoulder and a resulting ice impact force of 9124 N. The figure below illustrates this impact.



**Figure 47: Overhead View of Field Trial Impact**

The impact width was estimated to be 50 cm using internal video observations. The nominal contact area was found by multiplying the contact width by the ice thickness, 13 cm. This resulted in a nominal contact area of 0.065 m<sup>2</sup> and corresponding pressure of 0.140 MPa.

A summary of the two field impact measurements and the structurally limiting pressure and area defined by hydraulic ram tests is provided in the table below.

**Table 12: Hydraulic Ram Limits and Typical Field Measurements**

<b>Source</b>	<b>Contact Area (m<sup>2</sup>)</b>	<b>Pressure (Mpa)</b>
Hydraulic Ram Tests	0.018	4.22
Field Impact April 23rd	0.039	0.21
Field Impact April 24th	0.065	0.14

Recall that the contact area for the hydraulic ram tests is representative of the true contact area between the hydraulic ram and the laminate panel. The contact area considered for field trial impacts represented the nominal area found from video observations. There is uncertainty involved in the field area measurements. The ultimate strength of the laminate suggested by hydraulic ram tests is much larger than typical ice pressures measured during field trials. It was expected that the ultimate strength would be larger than field measurements since no structural damage was encountered during trials.

#### **2.4.8 Conclusions**

A total of 139 ice impacts were analysed from the 2009 Triton field trials measurements. All field impact loads were below the structural load limitations defined by hydraulic ram panel testing. This agreed with the observation that there was no structural damage due to ice impact encountered during trials. The ice collision cases considered indicated impact pressures that were much lower than the ultimate strength defined by hydraulic ram testing. Also, the peak field load measurement was more than three times less than the ultimate load of actual lifeboat panel found from hydraulic ram results. The field trials measurements are subsequently used for comparison with ice loads predicted by a numerical model that represents a lifeboat operating in ice.

### **3 Modelling**

This section describes the path taken to develop a mathematical model to represent a conventional lifeboat (i.e. small craft) impacting ice. The purpose of developing a mathematical model of the conventional lifeboat impacting ice was to enable the prediction of operational limitations by comparing model predictions to experimentally measured lifeboat laminate structural limits. This allows for the development of guidelines governing items such as lifeboat speed, ice thickness, ice mass and ultimately, the structural design of lifeboats operating in ice. Operational guidelines are required in both pack and level ice conditions and thus a model is required that can represent both cases.

#### *3.1 Modeling Approaches*

The first attempt at modeling was a simple force model based on the analysis of field trial results. This model was based on a single data set and impractical in the sense that it could not be extended to model different ice conditions (strength, thickness and mass). Next, the level ice case was represented using the Lindqvist model (Lindqvist, 1989). The results of this prediction of ice resistance compared well with lifeboat model resistance test results. An issue with this model was that it predicted the global resistance. Generally, global icebreaking forces in level ice do not pose a significant structural risk in comparison to local loads due to contact with heavier ice that is hit unintentionally (Daley, 2009).

The next step in the modelling process modified the Lindqvist model to predict localized forces. A similar approach was undertaken by Liu, Lau and Williams (2006) to model ice-hull interaction for real time simulation of ship manoeuvring in level ice. This model was modified to describe the lifeboat operating in ice. The model required an input of nominal ice contact area, indentation depth and cusp quantity. These values were all input based on field trial results in a single ice condition. This restricted the applicability of this model to other ice states and also the prediction of these terms adds a level of uncertainty to the overall model.

A simple conservation of energy model was explored. This model used the Lindqvist model and field trial observations to assess how ice failure energy changed with increasing lifeboat speed. This model was representative of field trial tests and did not have the capability to be extended to different ice conditions. This limitation existed because the energy model did not have an ice strength term. Next, the Popov model was considered (Popov, 1967). This is an ice-hull interaction model which uses a conservation of energy approach. The Popov model is based on the idea that a general 3D impact between two bodies can be represented by a one dimensional collision between a single body and a rigid wall (Popov, 1968). The trouble with this model is that it assumes the lifeboat hull is rigid and thus there is no energy absorbed in panel deformation. This may be the case for weak ice in which the ice fails before the hull collects a force large enough to cause flexure. However, for situations having the capability of causing structural failure, this idealization is not accurate.

The Popov model was adjusted to include a panel energy input term. This “extended Popov” model and is based on the same principles as the Popov model described above. When used in conjunction with the flexural failure limit, the predictions made by this model for both level and pack ice conditions compared well with field trials measurements.

### ***3.1.1 Simple Force Model***

The simple force model is based on Newton’s first law. During lifeboat field testing global accelerations were measured using mounted accelerometers. The acceleration files were analysed to pinpoint peak accelerations corresponding to ice impacts in both level and broken level ice. Global accelerations were measured for ice impacts at a full range of impact speeds. The global acceleration was plotted against impact speed and a linear trend line was drawn through the data. The equation of this trend line was used to predict global accelerations for speeds not encountered in field trials. The plot of global acceleration versus impact speed is shown below.

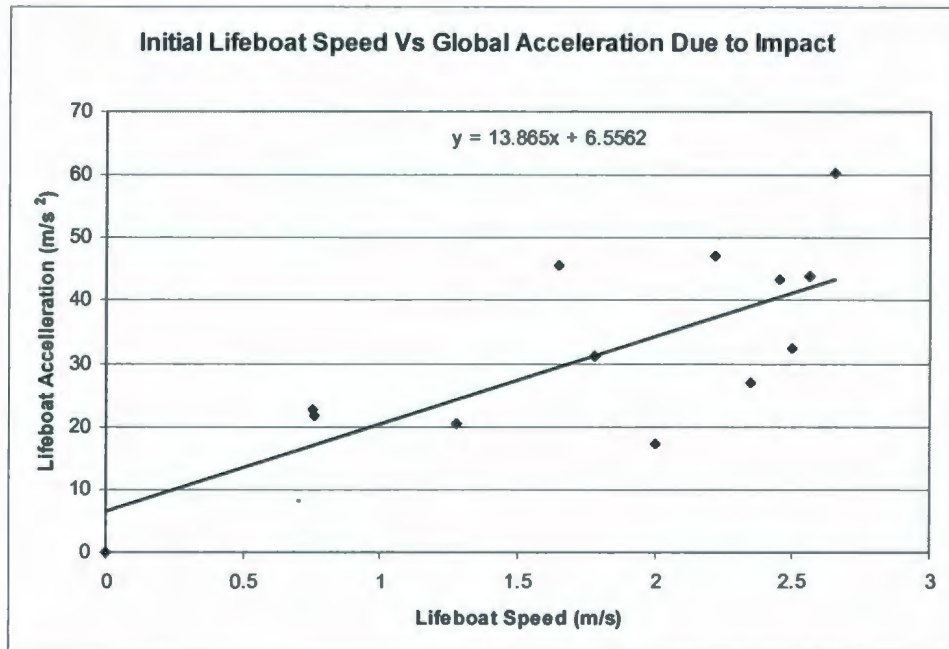


**Figure 48: Simple Force Model: Global Acceleration versus Speed**

The impact force can then be predicted for the lifeboat impacting ice at any speed. The equation used to predict impact force is shown below.

$$F_{impact} = m_{lifeboat} \times a_{global}$$

**Equation 3.1: Simple Force Model**

This impact force prediction method is rudimentary and has a number of uncertainties involved. The measured accelerations and thus predicted impact forces were extremely high. When compared to the global acceleration found by dividing the measured force by the known lifeboat mass, the measured accelerations were about 10 times larger. The measured accelerations may have been amplified due to the response of the structure upon which the accelerometer was mounted. Besides this issue, the simple force model does not accommodate different ice strengths, predicts global force instead of local force,

does not consider added mass, has no way of adjusting impact position and cannot differentiate between pack ice and level ice impacts.

### 3.1.2 Lindqvist Model

The Lindqvist model can be used to determine the icebreaking resistance of a vessel in level ice (Lindqvist, 1989). The Lindqvist resistance prediction equation is comprised of three components: the crushing resistance at the stem, the bending resistance over the whole bow and the submergence resistance along the underwater hull. The Lindqvist model in its general form is shown in the equation below.

$$R_{ice} = (R_c + R_B) \left(1 + \frac{1.4v}{\sqrt{gH_{ice}}}\right) + R_s \left(1 + \frac{9.4v}{\sqrt{gL}}\right)$$

Equation 3.2: Lindqvist Model Resistance Prediction (From Lindqvist, 1989)

In this equation  $R_c$  represents the ice crushing term,  $R_B$  is the ice breaking term and  $R_s$  is the submergence term. The ice crushing term is applicable only to ships with sharp stems, which continuously crush into ice (Lindqvist, 1989). Therefore, this term is not applicable to the blunt bow form of a lifeboat. The breaking and submergence resistance terms were found using the formulae below.

$$R_B = \frac{27}{64} \sigma_b B \left( \frac{H_{ice}^{1.5}}{\sqrt{\frac{E}{12(1-\nu^2)g\rho_w}}} \right) \left( \tan \psi + \frac{\mu \cos \phi}{\sin \alpha \cos \psi} \right) \left( 1 + \frac{1}{\cos \psi} \right)$$

Equation 3.3: Breaking Term (From Lindqvist, 1989)

$$R_s = \delta\rho g H_{ice} \left( BT \frac{(B+T)}{(B+2T)} + \mu(A_u + \cos\phi \cos\psi A_f) \right)$$

**Equation 3.4: Submergence Term (From Lindqvist, 1989)**

The variables involved in the ice resistance equations were described below.

- $v$  - vessel speed
- $H_{ice}$  - ice thickness
- $L$  - length of the vessel
- $g$  - acceleration due to gravity
- $\sigma_b$  - ice flexural strength
- $B$  - vessel breadth
- $T$  - vessel draft
- $E$  - modulus of elasticity of ice
- $A_u$  - area of the flat bottom
- $A_f$  - area of the bow
- $\delta\rho$  - density difference between water and ice
- $\alpha$  - bow angle (represented in drawing)
- $\phi$  - bow angle (represented in drawing)
- $\psi$  - function of  $\alpha$  and  $\phi$ ;  $\psi = \arctan(\tan\phi/\sin\alpha)$
- $\mu$  - friction factor between ice and hull surface

The figure below illustrates the underwater portion of the hull and presents some of the angles included in the ice resistance formulas described above.

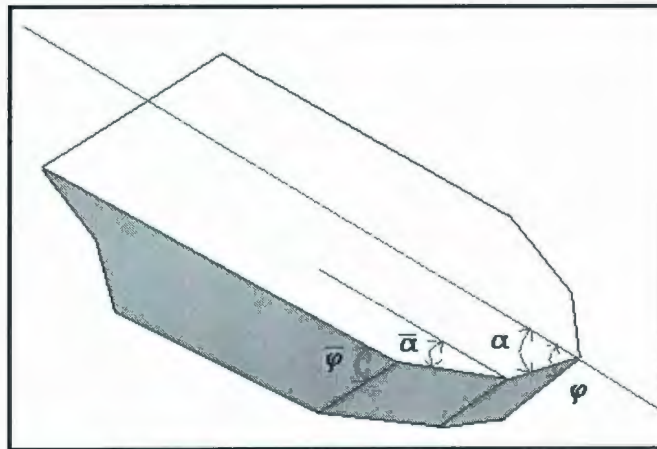


Figure 49: Hull Angles (Adapted From Lindqvist, 1989)

The Lindqvist model was assessed to determine how well it predicted the resistance of the lifeboat in level ice. To do this the Lindqvist predictions were compared to full scale resistance values extrapolated from model testing using the ITTC 78 method (ITTC, 1978).

### 3.1.2.1 Model Test Comparison

The model resistance tests were completed at a scale of 1:7. The ice thickness during testing was 46 mm, which corresponds to a full scale thickness of 322 mm. The hull-angles  $\alpha$  and  $\phi$  were determined from the 3D drawing of the model lifeboat. The waterline angle,  $\alpha$ , was found to be 44 degrees while the stem angle,  $\phi$ , was found to be 83 degrees. The variable  $\gamma$  was found based on the values of the other hull angles. This value was found to be 89.7 degrees. The length and breadth of the full-scale lifeboat at waterline was 9.7 m and 2.8 m respectively. The draft of the full scale-lifeboat was 0.854

m and the underwater and bow areas were 2 m<sup>2</sup> and 5 m<sup>2</sup> respectively. These values were all measured and scaled from the model drawing.

The flexural strength of ice was measured at the beginning and at the end of the model resistance tests. The values measured were 23 and 20 kPa respectively. The full scale ice flexural strength is equal to the model scale strength multiplied by the model scale factor. The flexural strength used in the Lindqvist model was taken to be the average of the two model ice measurements multiplied by the scale factor, 7. This resulted in a flexural strength of approximately 150 kPa full scale. This is the flexural strength used in the Lindqvist resistance prediction. The modulus of elasticity of ice was estimated using an empirical equation that relates the flexural strength to the ice modulus (Daley, 2009). This equation is shown below.

$$E = \sigma_f \times 5000$$

**Equation 3.5: Ice Modulus of Elasticity (From Daley, 2009)**

The modulus of elasticity of ice was found to be 752 MPa. It is important to note that typical ice elastic modulus values are around 6 GPa so the ice at hand is relatively weak. The density difference between water and ice during model testing was approximately 70 kg/m<sup>3</sup>. The friction factor between the lifeboat laminate and ice was taken as 0.05.

### **3.1.2.2 Lindqvist Model Results**

The Lindqvist model was used to approximate the total ice resistance on the hull of the lifeboat for a range of speeds corresponding to the speeds tested at model scale. The

model resistance tests which acted as a basis for comparison were completed up to full scale lifeboat speed of 1.5 m/s. These tests were completed in broken level ice at four different concentrations: 5, 6, 7, and 8 tenths. Since the model tests were conducted in broken level ice and not a consistent level ice sheet it was appropriate to remove the ice breaking term from the Lindqvist model. Therefore, the Lindqvist predictions included only a submergence term.

The ITTC 78 method was used to convert the measured model scale resistance values into full-scale results. The results compared well with the Lindqvist predictions. The full scale resistance values, found from the model tests, are shown in the plot below. This plot also includes the Lindqvist predictions.

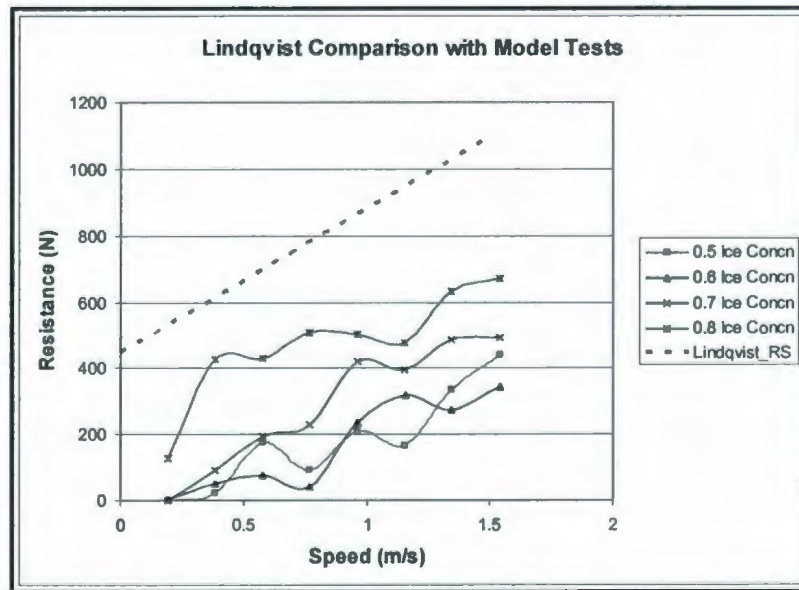


Figure 50: Lindqvist Model Predictions Compared To Resistance Test Results

The model test resistance values were presented for the four different ice concentrations tested. The model test data indicated that the resistance increased with increasing speed

and ice concentration. The Lindqvist model assumes level ice, or ice with a concentration of one. The Lindqvist predictions were higher than all the model test values. This followed the pattern of increasing resistance with increasing ice concentration.

Two lifeboat speeds, 0.385 and 1.16 m/s, were looked at closer to observe the pattern of increasing ice resistance with ice concentration. These speeds were selected for two reasons: first, simply because these were carriage speeds tested in the resistance model tests; second, because these two speeds indicated a constant increase in ice resistance with ice concentration. The resistance points corresponding to an ice concentration of one were predicted using the Lindqvist model.

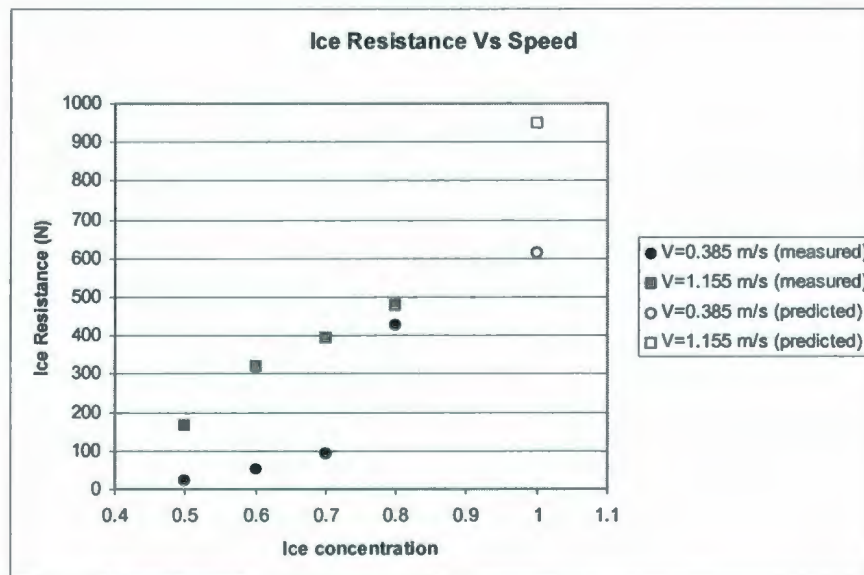


Figure 51: Ice Resistance versus Speed

The comparison of Lindqvist model predictions to extrapolated model test measurements showed that the Lindqvist results had the same pattern in terms of increasing ice

resistance with speed and ice concentration. The Lindqvist model predictions appeared to predict the global ice resistance of the lifeboat in pack ice well. This analysis suggests that the Lindqvist model could be used, in conjunction with an ice concentration factor, to predict the ice resistance in different pack ice concentrations.

In general, larger ice impact forces result from local impacts with heavy ice. Therefore, a method must be devised to predict local impact forces that arise from impact of level and pack ice.

### ***3.1.3 Extended Lindqvist Model***

The extended Lindqvist model adjusted the Lindqvist model to predict local impact force in level ice. A similar approach was undertaken by Liu, Lau and Williams (2006). The extended Lindqvist model uses an average load approach and calculates the equivalent local ice force on the hull according to ship motion and local ice conditions. The impact force in the extended Lindqvist model includes a breaking, submergence and clearing term.

The extended Lindqvist model was used to predict the local impact forces in level ice for the conventional lifeboat. The impact force was predicted for the operational speed range of the lifeboat and then compared with measured field trial impact values. The ice breaking term represented the force contributed by the ice breaking process. Therefore,

this component involved the force required to break ice in flexure and / or compression.

The equations to compute the flexural and crushing loads are shown below.

$$F_{flexure} = 0.518 \times \sigma_f \times h^2$$

**Equation 3.6: Extended Lindqvist - Ice Flexural Force (From Kerr, 1976)**

$$F_{crushing} = \sigma_c \times A$$

**Equation 3.7: Extended Lindqvist – Ice Crushing Force (From Sanderson, 1988)**

In these equations  $h$  refers to the ice thickness,  $\sigma_c$  is the ice compressive strength,  $\sigma_f$  is the ice flexural strength and  $A$  is the nominal ice contact area. The nominal contact area was assumed to be a constant value of  $0.00635 \text{ m}^2$ . This value was approximated based on field trial observations. In reality, the nominal contact area varies with ice geometry and impact position, along with other variables.

The submergence term was determined by multiplying the density difference between sea water and ice by the ice thickness and then again by the ice projected area. The term was divided into  $x$ ,  $y$ , and  $z$  components. The submergence terms are shown below.

$$F_{sub,x} = \Delta\rho gh_{A_{yz}}$$

$$F_{sub,y} = \Delta\rho gh_{A_{xz}}$$

$$F_{sub,z} = \Delta\rho gh_{A_{xy}}$$

**Equation 3.8: Extended Lindqvist - Ice Submergence Forces (From Liu, 2006)**

The projected area terms in the equations above represent the project area of submerged ice in each plane. For example,  $A_{yz}$ , represents the area of submerged ice in the  $yz$  plane. Predictions of the projected area values were based on observations made during field trials and field trial videos.

The clearing term is due to the inertial force caused by ice piece acceleration. The inertial force was found by dividing the kinetic energy of the accelerated ice by the distance travelled after ice impact. The process undertaken to calculate the clearing component was described by Liu (2006).

The extended Lindqvist model was used to predict the ice impact force for a range of impact speeds. The model predictions are shown in the plot below. The measured field trial data are also presented in this plot.

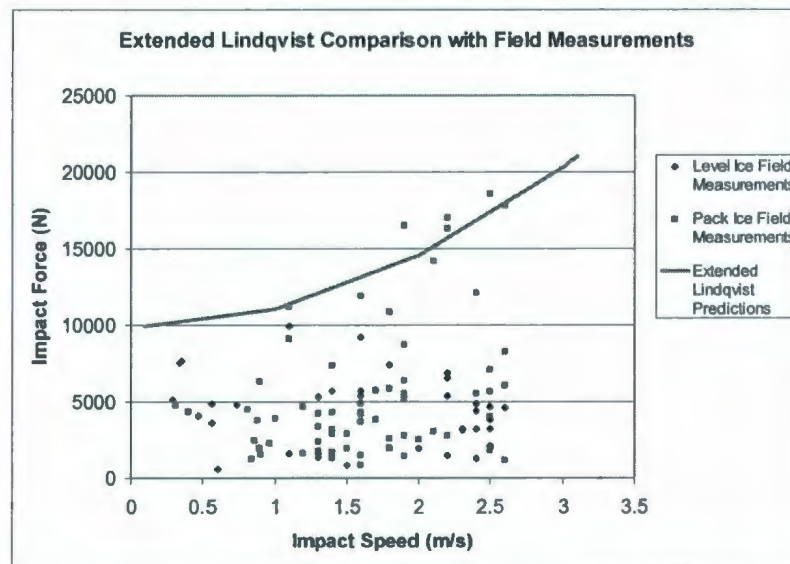


Figure 52: Extended Lindqvist Comparison with Field Trial Measurements

Overall, this model contained many uncertain terms including nominal area, projected areas, indentation depth, and cusp quantity. The comparison with field trial data showed model predictions close to the measured values. However, this was to be expected since the areas, indentation depth and cusp quantities were estimated based on observations

from this data set. A comparison with other measured data may not prove to be so accurate. This approach lacks the generality required of a predictive model.

### **3.1.4 Conservation of Energy Model**

In this model an energy balance was used to represent the lifeboat impacting ice. There were two separate cases considered: the first is an interaction with level ice and the second an interaction with pack ice. The level ice case considered a lifeboat transiting open water at constant speed. The lifeboat impacts level ice which has an infinite mass and travels some distance,  $l_{indent}$ , through the ice before coming to a complete stop. No structural damage occurs upon ice contact and hence, the panel energy is assumed to be zero. The conservation of energy equation to represent the level ice case is shown below.

$$\frac{1}{2} m_{boat} v_{boat,i}^2 + E_{propulsion} = E_{ice}$$

**Equation 3.9: Conservation of Energy Model - Level Ice**

In this equation  $m_{boat}$  represents the mass of the lifeboat,  $v_{boat,i}$  is the initial lifeboat speed,  $E_{propulsion}$  is the propulsive energy and  $E_{ice}$  is the ice failure energy.

The pack ice model involved the lifeboat travelling through open water at a constant speed and impacting a piece of pack ice. It was assumed that the lifeboat comes to a complete stop after impact and that the induced ice motion due to impact is insignificant. Another assumption is that hull failure occurs as a result of the impact. To determine the limiting speed the panel energy term was equated to the lifeboat ultimate failure energy

found from panel testing. The conservation of energy equation to represent the pack ice case is shown below.

$$\frac{1}{2} m_{boat} v_{boat,1}^2 + E_{propulsion} = E_{Ice} + E_{Panel}$$

**Equation 3.10: Conservation of Energy Model - Pack Ice**

The propulsive energy was found by multiplying the propeller thrust by the indentation depth into the ice. The thrust was calculated based on the tow resistance which had been measured for the lifeboat for a range of speeds (Simões Ré et al; 2008). The equation used to calculate the thrust is shown below.

$$T = \frac{R_T}{(1-t)}$$

**Equation 3.11: Lifeboat Thrust**

Where  $T$  is the thrust,  $R_T$  is the tow resistance, and  $t$  is the thrust deduction fraction. The thrust deduction fraction was estimated based on lifeboat hull parameters to be 0.36 (SNAME, 1988). A model of ice indentation versus speed was found using field trial results of known impact speeds and corresponding ice indentation. The equation used to determine the propulsive energy is shown below.

$$E_{propulsion} = T \times l_{indent}$$

**Equation 3.12: Propulsive Energy**

This propulsion energy approach was used in the level ice energy model to predict the ice failure energy for the operational speed range of the lifeboat. The ice failure energy was

plotted against speed and a trend line was fitted to the data. The equation of this trend line was used to predict the ice failure energy for the pack ice and level ice energy models.

For the level ice model the hull integrity was assessed by computing the ice failure energy for the full range of lifeboat speeds. Then for each speed the average ice resistance was computed using the equation below.

$$R_{average} = \frac{E_{ice}}{l_{indent}}$$

**Equation 3.13: Average Ice Resistance**

The average ice resistance was then compared with structurally limiting force values defined by panel testing. This analysis showed that the lifeboat would not encounter a structural failure at any operational speed in level ice. This was the case because the computed average resistance values were all well below the limiting force. The finding is based on structural limits defined by hydraulic ram testing and is thus relevant to the structure tested. The field trials complied with this result since there was no structural damage due to level ice impacts.

For the pack ice model the hull integrity was assessed by computing the lifeboat speed when the panel energy term was replaced with the structural yield and ultimate forces. The limiting speeds calculated from this approach were above the current maximum lifeboat speed. This indicates that the lifeboat could travel at any speed (for which it is powered) and impact pack ice without causing structural damage. Again, this case

compared well with field trial observations in which pack ice collisions did not cause structural damage.

The prediction of ice energy in this model used field trial results in relatively weak ice. Therefore, the results were indicative of this particular type of ice. To extend the model to different ice conditions another method of modelling ice energy must be considered. In other words, this model lacked the generality to allow it to predict impact forces for ice conditions other than the condition upon which the model was based.

### ***3.1.5 Popov Model***

The next attempt at modelling the lifeboat in ice involved an existing ice interaction model known as the Popov model. The Popov model calculates the normal force resulting from a rigid vessel impacting ice. This is done by first reducing the masses and velocities to the line of impact and then using a conservation of energy approach to solve the problem of a collision between two bodies (Popov, 1967). The concepts from this model were applied to the lifeboat to predict ice impact forces.

An idealization of the Popov model is that the ice pressure is defined in terms of the nominal contact area and process pressure coefficients,  $P_o$  and  $ex$ . The process pressure describes the variation of the average pressure within the nominal contact area as the ice indentation increases (Daley, 2004). The ice process pressure equation is shown below.

$$P_{ice} = P_o A^{ex}$$

**Equation 3.14: Pressure Area Relationship (From Daley, 1999)**

Here the term  $P_{ice}$  represents the ice pressure and  $A$  represents the nominal contact area between the ice and the lifeboat hull. The terms  $P_o$  and  $ex$  are both constants representative of the ice strength. This process pressure trend was apparent in many full-scale data sets and proposed by authors such as Sanderson (1988) and Ghoneim and Keinonen (1983).

An assumption in the Popov model of the lifeboat colliding with ice is that the nominal contact area between the lifeboat and the ice edge can be represented as the contact area between a vertical cylinder and an ice edge. The bow area of the lifeboat is of primary consideration since it is the region that would encounter the highest quantity of ice impacts and the highest magnitude of ice impact forces. The bow area of the conventional lifeboat, in the ice belt region, was approximated, in terms of geometry, as a vertical cylinder. Contact area as a function of ice indentation was represented as by Daley (1999).

$$A = 2H\sqrt{2R}\delta_{ice}^{0.5}$$

**Equation 3.15: Nominal Contact Area (Adapted From Daley, 1999)**

In this equation  $H$  represents the ice thickness,  $R$  is the radius of the lifeboat bow, and  $\delta_{ice}$  is the ice indentation. The lifeboat bow radius was measured from a drawing of the lifeboat to be 0.8 m. The normal impact force can be calculated by multiplying the ice pressure by the nominal contact area. This equation is shown below.

$$F_n = P_o A^{1+ex}$$

**Equation 3.16: Normal Ice Force (From Daley, 1999)**

There are two separate equations for predicting ice impact force in this model. The first models an impact with level ice and the second models an impact with pack ice. For the level ice case, it is assumed that the lifeboat comes to a complete stop after impact. For the pack ice case, the final ice speed is assumed to be equal to the final lifeboat speed. Both equations were derived using the same principles.

### *3.1.5.1 Level Ice Case*

The level ice case assumed that the ice had a velocity equal to zero throughout the collision. It also assumed that there was no significant panel deflection energy and that the lifeboat final velocity was zero. The basic conservation of energy equation for the level ice case is shown below.

$$\frac{1}{2} m_e v_n^2 = \int F_n d\delta_{ice}$$

**Equation 3.17: Popov Model - Conservation of Energy – Level Ice**

This equation states that all of the initial kinetic energy from the lifeboat is consumed by ice failure. The impact force arising from the lifeboat colliding with level ice was found using the conservation of energy equation along with the normal force, nominal contact area, and pressure-area relationship equations. The normal force equation for level ice is shown below.

$$F_n = P_o (2H\sqrt{2R})^{1+ex} \left( \frac{\frac{1}{2} m_e v_n^2 (1.5 + 0.5ex)}{P_o (2H\sqrt{2R})^{1+ex}} \right)^{\frac{0.5+0.5ex}{1.5+0.5ex}}$$

**Equation 3.18: Popov Model - Level Ice Impact Force (Adapted From Daley, 1999)**

Where:

- $H$  – ice thickness (m)
- $R$  – lifeboat bow radius (m)
- $m_e$  – effective mass of lifeboat at collision point (kg)
- $v_n$  – normal velocity at collision point (m/s)
- $P_o$  – ice process pressure term (Pa)
- $ex$  – ice process pressure exponent

The variables involved in the level-ice normal-force equation include the lifeboat speed, ice thickness and ice strength terms ( $P_o$  and  $ex$ ). One can also vary the impact position and adjust the hull angles accordingly. This affects the effective lifeboat mass and normal velocity both of which are described in a subsequent section.

### **3.1.5.2 Pack Ice Model**

The pack ice model assumed that the initial ice velocity was zero, the coefficient of restitution between the lifeboat and ice was 0.2 and the final lifeboat speed was equal to the final ice speed. This model also had the general Popov assumption that the lifeboat

was rigid and thus had no significant panel deformation energy. The basic conservation of energy equation for the pack ice case is shown below.

$$\frac{1}{2} m_e v_n^2 = \frac{1}{2} m_e v_{n,2}^2 + \frac{1}{2} m_{ice} v_{ice,2}^2 + \int F_n d\delta_{ice}$$

**Equation 3.19: Popov Model - Conservation of Energy - Pack Ice**

The impact force arising from the lifeboat colliding with pack ice was calculated using the equation shown below. This equation was derived from the conservation of energy equation for pack ice along with the normal force, nominal contact area and pressure-area relationship equations.

$$F_n = P_o (2H\sqrt{2R})^{1+ex} \left( \frac{1.5+0.5ex}{2P_o (2H \cdot \sqrt{2R})^{1+ex}} \cdot \left( m_e v_n^2 - m_e \left( \frac{m_e v_n - m_l v_n e}{m_l + m_L} \right)^2 - m_l \left( \frac{m_e v_n - m_l v_n e}{m_l + m_L} + v_n e \right)^2 \right)^{\frac{0.5+0.5ex}{1.5+0.5ex}} \right)$$

**Equation 3.20: Popov Model - Pack Ice Impact Force (Adapted From Daley, 1999)**

Where:

- $m_{ice}$  – mass of ice (kg)
- $e$  – coefficient of restitution between lifeboat and ice

The ice mass refers to the mass of the ice piece impacted in the lifeboat-ice collision. The coefficient of restitution was found experimentally from laboratory ice impacts on the lifeboat to be 0.2. All other parameters were the same as those described in the level-ice case.

The variables involved in the pack-ice normal-force prediction equation include: ice thickness, vessel speed, ice strength terms and ice mass. As in the level ice case, the impact position can be varied to approximate impact force at different hull locations.

### 3.1.5.3 Effective Mass and Normal Velocity

The effective mass is a function of the lifeboat mass, radii of gyration, hull angles and moment arms. It represents the apparent mass at the point of impact. The effective mass is defined as follows:

$$m_e = \frac{m_{lifeboat}}{C_o}$$

**Equation 3.21: Equivalent Mass (From Popov, 1968)**

Where:

- $C_o$  – mass reduction coefficient (unit less)

The mass reduction coefficient was calculated using the following equation.

$$C_o = \frac{l^2}{(1 + AMx)} + \frac{m^2}{(1 + AMy)} + \frac{n^2}{(1 + AMz)} + \frac{\lambda l^2}{(rx^2(1 + AMrol))} + \frac{\mu l^2}{(ry^2(1 + AMPit))} + \frac{\eta l^2}{(rz^2(1 + AMyaw))}$$

**Equation 3.22: Mass Reduction Coefficient (From Popov, 1968)**

In this equation  $l$ ,  $m$ , and  $n$  are the direction cosines. They are found using the equations below.

$$\begin{aligned} l &= \sin \alpha \cdot \cos \beta' \\ m &= \cos \alpha \cdot \cos \beta' \\ n &= \sin \beta' \end{aligned}$$

**Equation 3.23: Direction Cosines (Adapted From Popov, 1968)**

The terms:  $\lambda l$ ,  $\mu l$  and  $\eta l$  are the moment arms. They are represented by the equations below.

$$\begin{aligned}\lambda l &= n \cdot y_p - m \cdot z_p \\ \mu l &= l \cdot z_p - n \cdot x_p \\ \eta l &= m \cdot x_p - l \cdot y_p\end{aligned}$$

**Equation 3.24: Moment Arms (Adapted From Popov, 1968)**

The added mass terms were found using the following equations.

$$\begin{aligned}AMx &= 0 \\ AMy &= \frac{2 \cdot T}{B} \\ AMz &= \frac{2 \cdot B \cdot C_{wp}^2}{3 \cdot T \cdot C_b \cdot (1 + C_{wp})} \\ AMrol &= 0.25 \\ AMpit &= \frac{B}{T(3 - 2 \cdot C_{wp})(3 - C_{wp})} \\ AMyaw &= 0.3 + \frac{0.05 \cdot L}{B}\end{aligned}$$

**Equation 3.25: Added Mass Terms (Adapted From Popov, 1968)**

The equations describing the mass radii of gyration squared are given below.

$$\begin{aligned}rx^2 &= \frac{C_{wp} \cdot B^2}{11.4 \cdot C_m} + \frac{H^2}{12} \\ ry^2 &= 0.07 \cdot C_{wp} \cdot L^2 \\ rz^2 &= \frac{L^2}{16}\end{aligned}$$

**Equation 3.26: Radii of Gyration (Adapted From Popov, 1968)**

The mass reduction coefficient and subsequent equations contained parameters directly related to the hull geometry and point of impact. The  $x$ ,  $y$ , and  $z$  coordinates represent the

location of the impact position on the hull. The hull angles correspond to the impact point.

The normal velocity is equal to the lifeboat velocity multiplied by the  $x$ -direction cosine. This is shown in the equation below.

$$v_n = v_{ship} \cdot l$$

**Equation 3.27: Normal Velocity (From Popov, 1968)**

A conventional right hand coordinate system was used in the prediction model. The origin of the coordinate system was at the lifeboat center on the waterline.

#### **3.1.5.4 Model Comparisons**

The impact force was predicted for the operational speed range of the conventional lifeboat for both the pack ice and level ice conditions. These predicted values were then compared with measured impacts from the April 2009 field trials.

The lifeboat bow radius,  $R$ , was measured to be approximately 0.8 m and the ice thickness,  $H$ , during full-scale field trials with the lifeboat had a mean value of 0.14 m. For the purposes of illustration here, the ice mass in the pack ice model was set to be half of the lifeboat mass, 1900 kg. The value used for the exponent,  $ex$ , was -0.5. This  $ex$  value was proposed by Sanderson (1988) and was based on analysis of Polar Sea and other full scale ice breaker impact tests. The pack ice encountered during field trials appeared stronger

than the level ice. Hence, the ice process pressure term used for comparison with field trials measurements was different for the pack ice and level ice case.

In both ice conditions the ice appeared to be weak and decaying. There were no measurements taken during field trials that would allow for direct assessment of the ice process pressure term,  $P_o$ . Therefore, the values were taken from field trial results in the Bering Sea (St. John, 1986). The  $P_o$  values for the level and pack-ice conditions used for field trial comparison were 0.1 MPa and 0.15 MPa respectively. Note that these came from the lower end of the Bering Sea measurements.

Predictions of the level and pack ice Popov model are compared to the field trial measurements in the plot below. The field trial measurements were divided into pack ice and level ice cases.

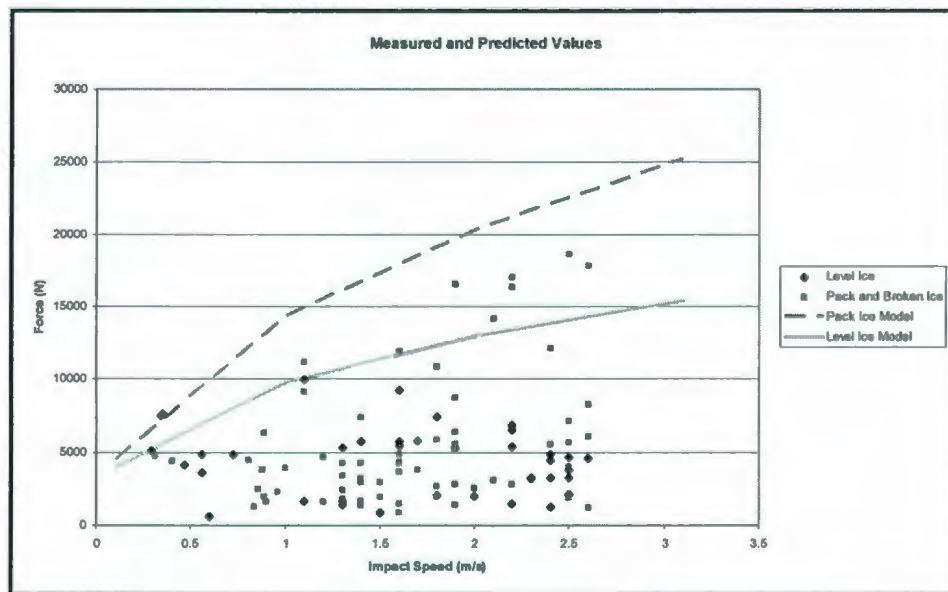


Figure 53: Popov Model Comparison with Field Measurements

The level and pack ice models both appear to represent the field measurements well. Both models indicate an increase in impact force versus speed which is observed in the measured data. The models predict impact forces that are, in general, higher than those measured for any given speed. This may be a result of the process pressure term  $P_o$ , used to represent the field trial ice. Of course, the pack ice impacts were not all with 1900 kg pieces of ice.

### *3.1.5.5 Model Concerns*

The main concern with this model was the assumption of hull rigidity. The Popov model was created to predict impact forces between large icebreaking vessels and ice pieces. In this situation the assumption of a rigid hull is reasonable. In the case of a small craft such as the conventional lifeboat, the hull is not rigid and panel deformation must be considered.

Another issue was that there was no easy method of determining the ice process pressure terms,  $P_o$  and  $ex$ . There have been tests done in various areas of the Arctic and Sub-Arctic which have records of the ice strength parameters. However, to predict impact forces with a high level of certainty the ice pressure values corresponding to the ice involved in the interaction process must be known.

Other concerns include the assumptions made regarding the lifeboat contact area and coefficient of restitution. These both lead to uncertainty in the model. The contact area

assumption was used to compute the nominal ice contact area as a function of the ice indentation. The coefficient of restitution assumption was used in the pack ice model, along with conservation of momentum, to determine the final lifeboat and ice velocities.

### 3.1.6 Extended Popov Model

The aim of the extended Popov model was to address the weaknesses in the general Popov model to increase the accuracy of impact force prediction. The extended Popov model includes a panel deformation term and it assumes that the ice crushing force is equal to the compressive strength of ice multiplied by the nominal contact area (Sanderson, 1988). There were two separate cases considered: level ice and pack ice. The pack ice condition assumes that ice failure occurs in compression. The level ice case considers both compressive and flexural failure. The equations for the level and pack ice cases are given below.

$$F_n = 8 \times H^2 \times \sigma_c \times R \times v_n \sqrt{\frac{K \times m_e}{K + 64 \times H^4 \times \sigma_c^2 \times R^2}}$$

Equation 3.28: Extended Popov - Level Ice Impact Force

$$F_n = \sqrt{\frac{8H^2\sigma_cRK}{(K + 8H^2\sigma_cR)}} \times \left[ m_e v_n^2 - m_e \left( \frac{m_e v_n - m_{ice} v_n e}{m_e + m_{ice}} \right)^2 - m_{ice} \left( \frac{m_e v_n - m_{ice} v_n e}{m_e + m_{ice}} + v_n e \right)^2 \right]$$

Equation 3.29: Extended Popov - Pack Ice Impact Force

$$F_{flexure} = 0.518 \times \sigma_f \times h^2$$

Equation 3.30: Flexural Failure Limit (From Kerr, 1979)

Where:

- $H$  – ice thickness (m)
- $\sigma_c$  – ice crushing strength (MPa)
- $\sigma_f$  – ice flexural strength (MPa)
- $R$  – lifeboat bow radius (m)
- $v_n$  – normal lifeboat velocity at collision point (m/s)
- $K$  – panel stiffness
- $m_e$  – effective mass of lifeboat at collision point (kg)
- $m_{ice}$  – mass of ice (kg)
- $e$  – coefficient of restitution between lifeboat and ice

Other variables include the craft particulars, bow angles and added mass terms. Each variable involved in the model can be changed to represent different ice conditions, impact location along the hull or craft type. This leads to a general model capable of representing a range of ice interaction situations.

The assumptions involved in this model are as follows:

- Lifeboat comes to a complete stop after contacting level ice
- Final lifeboat velocity is equal to final ice velocity
- Coefficient of restitution is 0.2
- Ice contact area described as a vertical cylinder contacting ice
- Hull deflection is linearly proportional to impact force

The assumption relating to the linearity of hull deflection and impact force was used as a means to incorporate panel deformation into the model. The panel stiffness was found from analyzing the force versus displacement curves that resulted from the hydraulic ram tests.

#### *3.1.6.1 Model Comparison*

The extended Popov model was used to predict ice impact forces typical of those observed during field testing. The mode value of each ice parameter observed during trials was input into the prediction model. The ice compressive strength was set to 1.44 MPa and the ice flexural strength was set to 391 kPa. The ice thickness was set to 0.14 m, the ice mass was set to 3800 kg (lifeboat mass) and the panel stiffness was set to 2.91 MN/m. Predictions were made for a range of impact speeds relating to the operational speed range of the lifeboat. These predictions were compared to impact forces measured in the field. The model predictions and measured field impact forces are shown in Figure 54 and Figure 55 below.

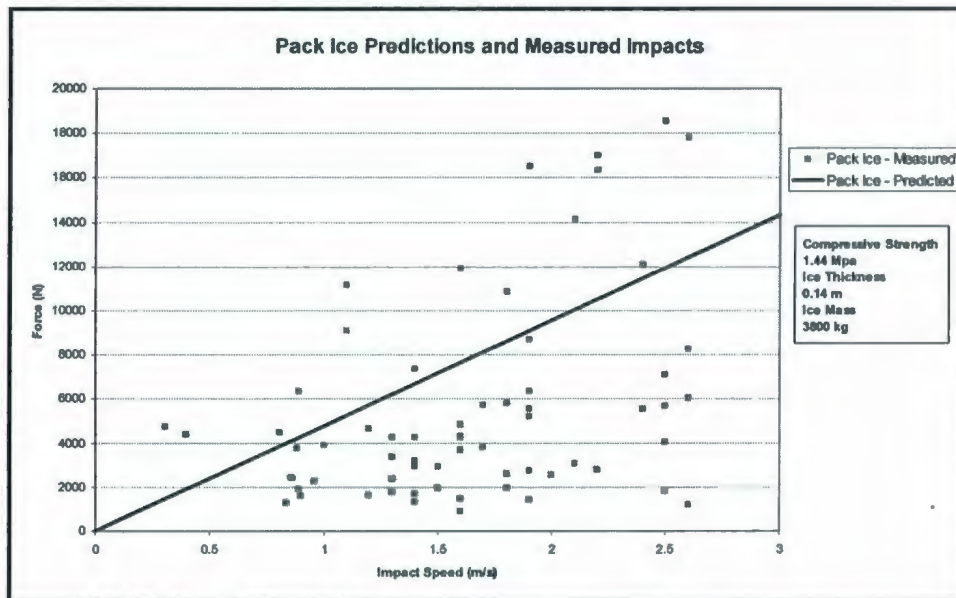


**Figure 54: Extended Popov Pack Ice Comparison**

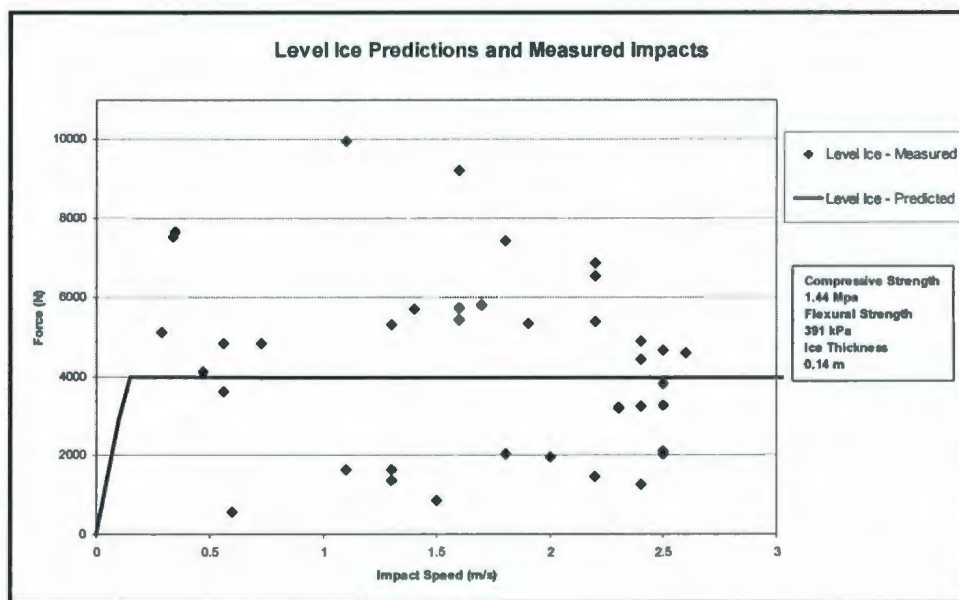


**Figure 55: Extended Popov Level Ice Comparison**

The predicted pack and level ice impact forces compare well with the measured data. The prediction lines are within the pack and level ice field measurements. This was expected since the mode values of the ice parameters were used in the predictions.

### **3.1.6.2 Sensitivity Analysis**

A sensitivity analysis was performed on the level and pack ice extended Popov prediction equations to determine the extent to which each variable affects the predicted impact force. The range of each variable tested in the sensitivity analysis is based on the limits of ice parameters observed during 2009 field trials and the extents of the empirical terms defined through experimental testing. When a variable is considered in the sensitivity analysis the remaining variables are maintained at the mode value observed during field trials or the mean value calculated from experimental testing. The value of each variable is represented in the legend of each plot.

#### **Ice Mass**

The sensitivity of the extended Popov model to variations in ice mass was explored first. The ice mass observed from Triton, 2009 trials ranged from 45 kg to 4600 kg. The ice mass is a variable in the pack-ice case but not the level ice case. The pack ice model was used to predict the impact forces arising from collisions with ice at the upper and lower limits of the ice mass range. The model was also used to predict ice impact forces arising from collision with an ice piece having a mass equal to 100 times the fully loaded lifeboat mass (380000 kg). The predictions are made for impact speeds throughout the lifeboat operational speed range. The results of the pack ice model predictions are shown in the figure below.

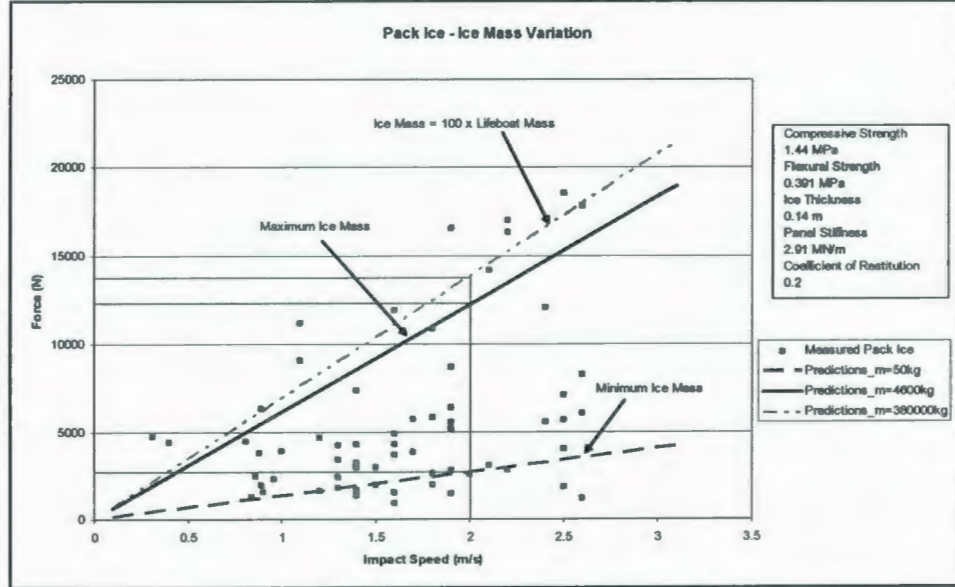


Figure 56: Pack Ice Predictions – Ice Mass Variation

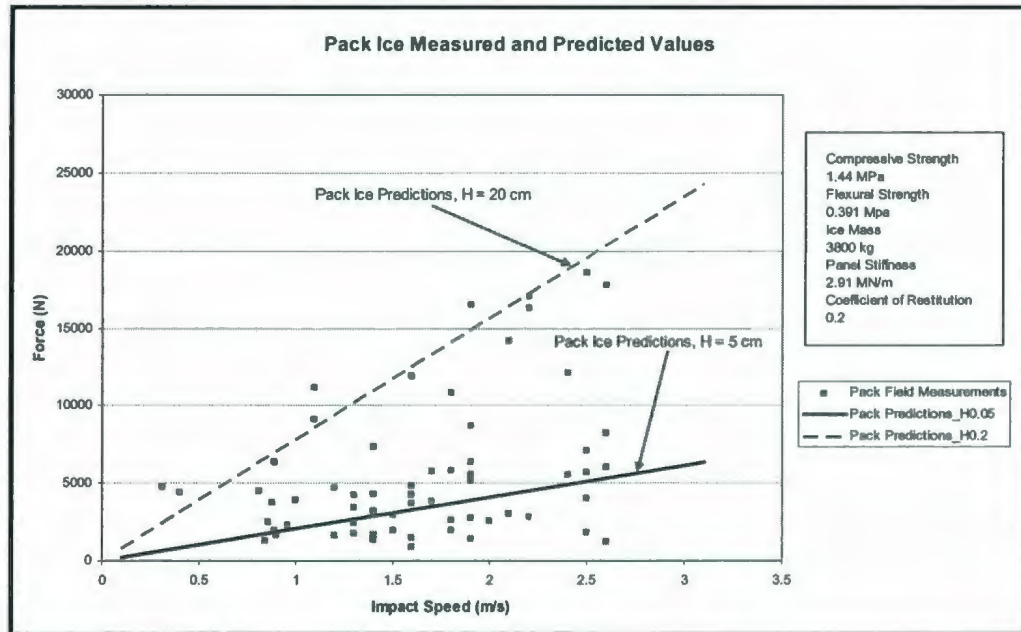
Figure 56 indicates that the extended Popov model is sensitive to variations in ice mass. It also indicates that if the ice mass is beyond some limiting value the model becomes insensitive to mass variation. An impact speed of 2.00 m/s is highlighted in Figure 56 to illustrate this finding.

### Ice Thickness

The ice thickness is the next parameter considered. The ice thickness was observed to range from 0.05 m to 0.2 m during field testing. The extended Popov model was used to predict the impact forces arising from collisions with ice at the upper and lower limits of the ice thickness range. The variation in level ice predictions are shown in the plot below.



below. This plot indicates that the pack ice impact force predictions are also sensitive to variation in ice thickness.



### Ice Strength

The next variables considered in the sensitivity analysis are the ice strength terms. The flexural strength is only a variable in the level ice case, as it is assumed that all ice fails in compression for the pack ice condition. Compressive strength is a variable in both the pack and level ice cases. The range in compressive strength was found to be 1.37 MPa to 1.44 MPa, and the range in flexural strength was found to be 0.279 MPa to 0.391 MPa. Level ice predictions were made at both the low and high ice strength limits. This comparison is shown below along with field trial level ice measurements.

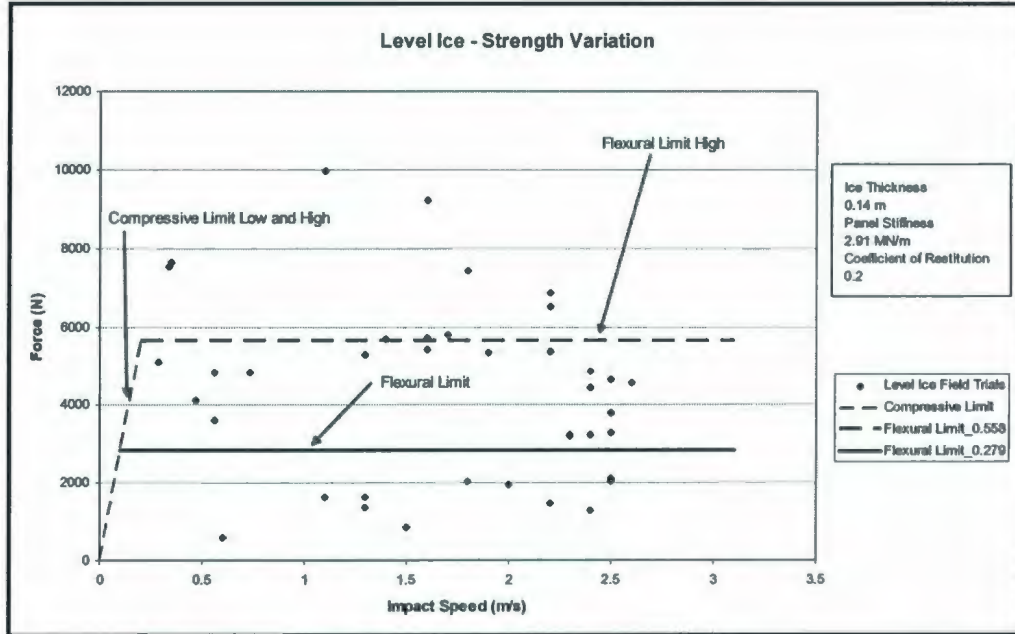


**Figure 59: Level Ice Predictions - Ice Strength Variation**

There was no apparent change in the compressive limit for the range in compressive strengths observed during trials. The flexural limit was moderately affected by the variation in flexural strengths observed during trials.

Next the sensitivity to ice strength was assessed for the pack ice model. Predictions were made with the pack ice equation for compressive strength values of 1.37 MPa and 1.44 MPa. These predictions are shown on the plot below, along with pack ice field trial measurements.

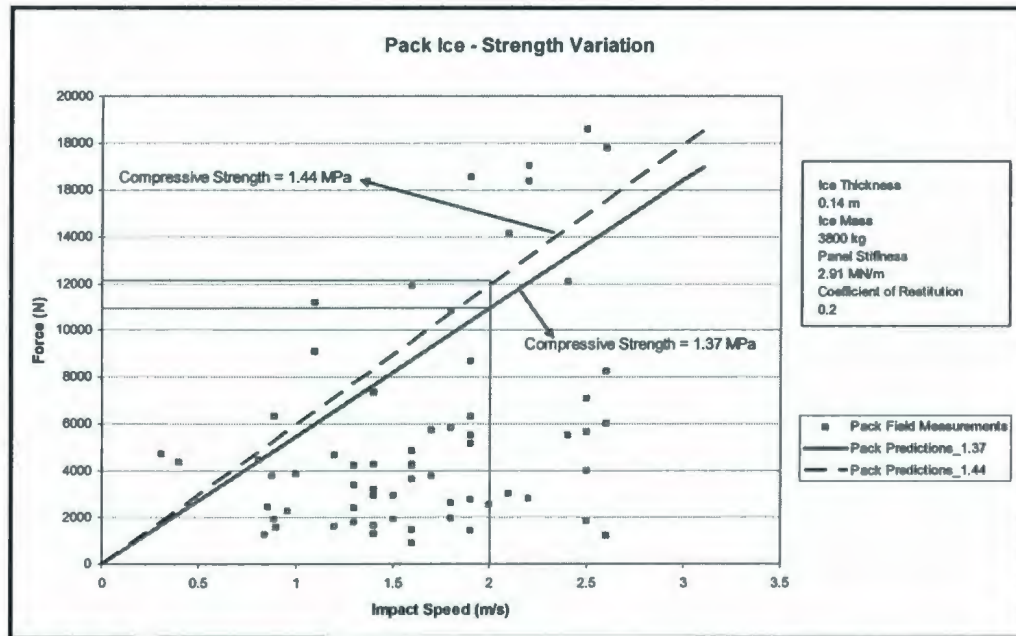


**Figure 60: Pack Ice Predictions - Ice Strength Variation**

The range in ice strength observed during trials was small and therefore it is not possible to determine the model sensitivity to strength variation. Figure 60 indicates that the model predictions do not vary greatly for the ice strength range that was assessed.

### Panel Stiffness

The panel stiffness was the next variable considered in the sensitivity analysis. The laminate panel stiffness was found to range between 2.06 MN/m – 2.91 MN/m from analysis of hydraulic ram test results. The impact force predictions of the level ice extended Popov model for the extents of the panel stiffness range are shown below.

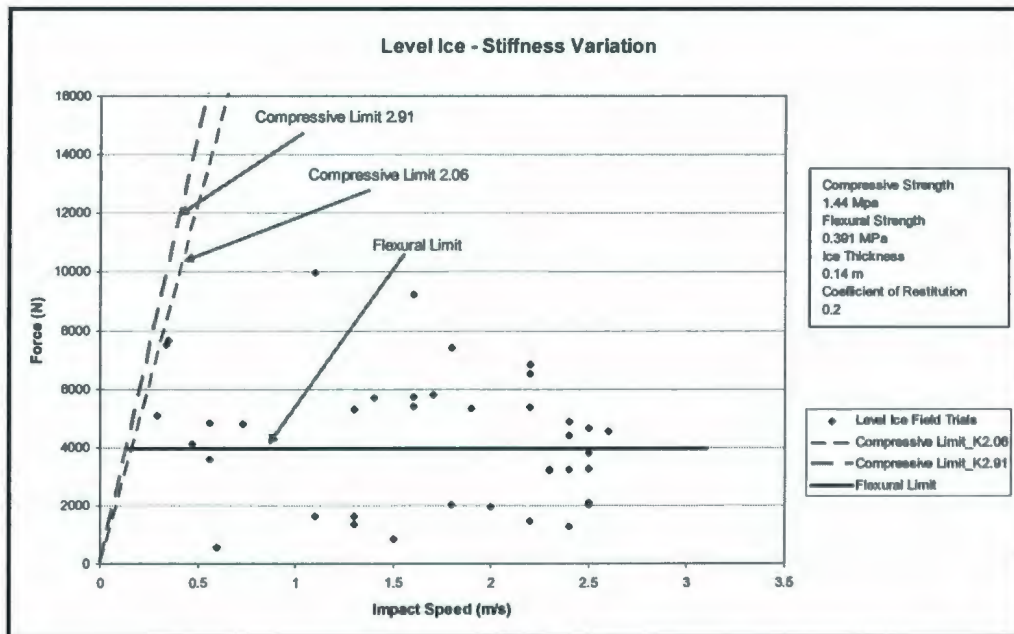


**Figure 61: Level Ice Predictions - Stiffness Variation**

The flexural limit is unaffected by variation in panel stiffness. The compressive limits for both  $k$  values are extended beyond the flexural limit for clarity. There is only slight offset in the compressive limit due to  $k$  variation, which suggests that the level ice extended Popov model is insensitive to changes in panel stiffness. The pack ice sensitivity analysis for panel stiffness is described in the plot below.

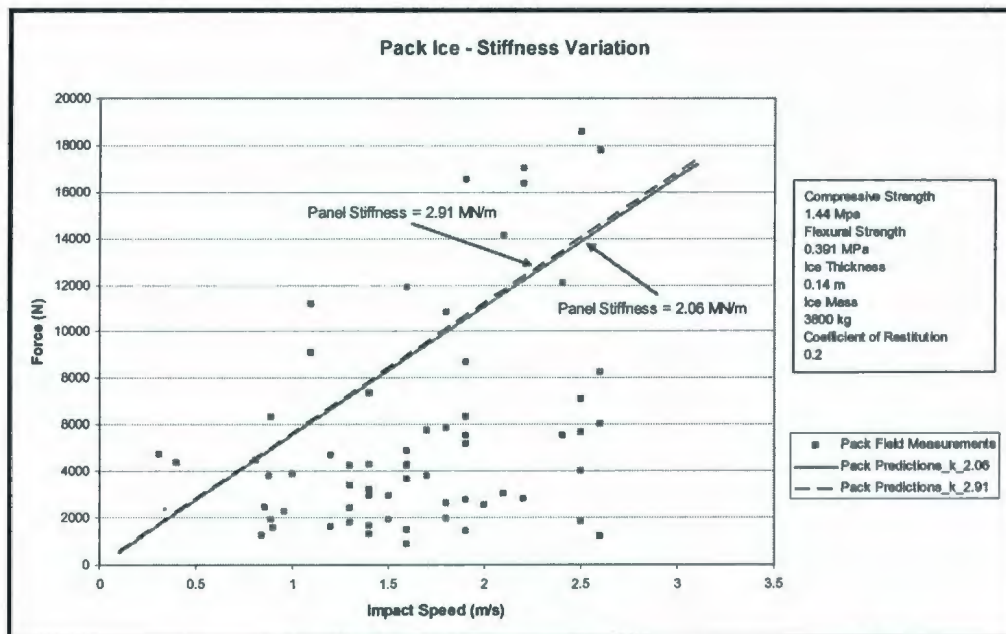


**Figure 62: Pack Ice Predictions - Stiffness Variation**

The variation in predicted impact forces due to a variation in panel stiffness is barely distinguishable. This indicates that the pack ice impact force predictions are not sensitive to panel stiffness variation for the stiffness range assessed.

### **Coefficient of Restitution**

The coefficient of restitution,  $e$ , between ice and lifeboat laminate was the final variable considered in the sensitivity analysis. This was a variable only in the pack ice prediction equation. The coefficient of restitution was found to range from 0.15 to 0.25 from analysis of pendulum test results. The pack ice model was used to predict impact forces using the minimum and maximum extents of the range of  $e$  values. These predictions are shown in the plot below. The predicted impact force does not vary significantly for the range of coefficient of restitution values considered.

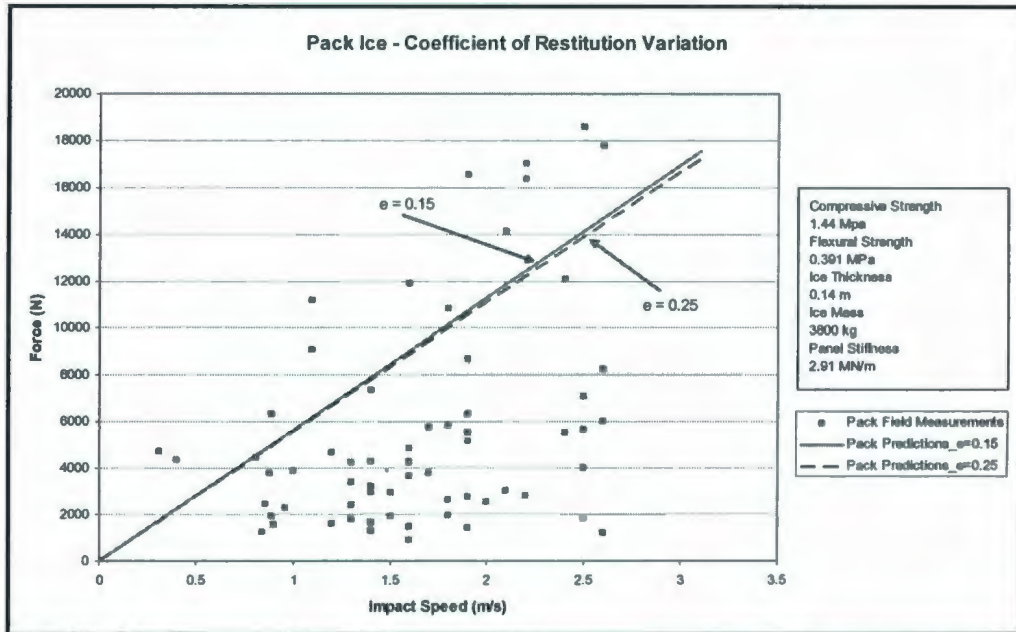


**Figure 63: Pack Ice Predictions – Coefficient of Restitution Variation**

In summary the sensitivity analysis suggests that the model is quite sensitive to variations in ice thickness and ice mass. There appears to be moderate sensitivity to ice strength. Variations in panel stiffness and coefficient of restitution had a small affect on the impact force predictions.

## 4 Regulated Design

This section describes an assessment made concerning the applicability of two standards to small craft design. The standards considered in this study include the Canadian Standards Association's (CSA) General Requirements, Design Criteria, the Environment and Loads and the International Organization for Standardization's (ISO) Petroleum and Natural Gas Industries – Arctic Offshore Structures. The latter standard is a draft and is subject to change prior to final publication. These two guidelines were primarily developed for large, stationary, offshore structures and thus the relevance to small, mobile craft design is uncertain.

To complete the analysis the local and global ice pressures were computed, relevant to each standard, for nominal contact areas ranging from 0.1 to 1.0 m<sup>2</sup>. The corresponding ice loads were found by multiplying the ice pressure by the nominal contact area. The design loads were compared to one another, to laminate limitations defined by material testing and to extended Popov model predictions.

### 4.1 CSA Ice Design Loads

The CSA guidelines were used to compute the global and local ice design loads for the level ice condition. CSA deals with ice loading in terms of a probabilistic approach. The probabilistic method involves the distribution of measured full-scale forces.

### 4.1.1 Global Loading

The global ice pressure was defined as shown in the equation below.

$$P = C_p A^{D_p}$$

Equation 4.1: CSA Global Ice Pressure

In this equation  $A$  refers to the nominal contact area between the structure and piece of ice,  $C_p$  is a coefficient and  $D_p$  is a negative exponent.  $C_p$  and  $D_p$  are both empirical constants that relate the ice pressure to the nominal contact area. These constants were defined based on field data from large structures in ice.

To define the global ice loads a number of assumptions had to be made. Lifeboat-ice interactions were assumed to be in the low aspect ratio category. The aspect ratio was defined as the loading width divided by the loading height. The category low was defined as aspect ratios below 10. The global pressure constants,  $C_p$  and  $D_p$ , were defined for high and low aspect ratios. Three ice zones were defined by the standard. The first zone extends across the Canadian / Alaskan boundary. Pressure - Area (PA) constants are defined in terms of measurements taken from these zones. Zone one was used for the current calculation. The PA constants are also divided by ranges in contact area. For this calculation the PA constants were selected based on the less than 50 m<sup>2</sup> contact area range.

Using the aforementioned assumptions,  $C_p$  and  $D_p$  were found to be 3.0 and -0.4 respectively. The result of the global ice force versus increasing contact area is shown in the plot below.

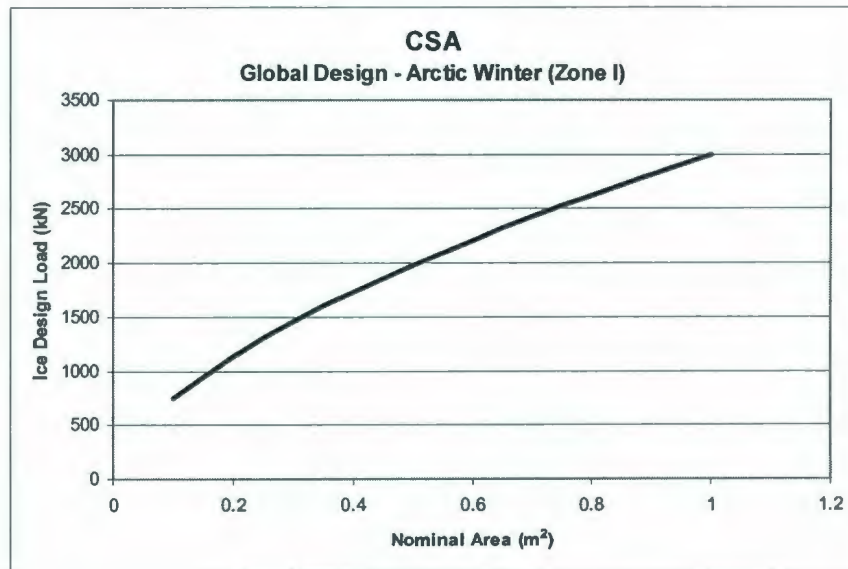


Figure 64: CSA Global Ice Loads

#### 4.1.2 Local Loading

CSA standards define the local ice pressure in terms of a probabilistic method introduced by Jordaan et al. (1993). An update to this method has been proposed by Taylor et al. (2009) and is followed to compute the local loadings. The extreme ice pressure for a given exceedence probability is shown in the equation below.

$$z_e = x_o + \alpha \{ -\ln[-\ln F_z(z_e)] + \ln v + \ln r \}$$

Equation 4.2: CSA Local Ice Pressure

Where:

$x_o$  – offset in the distribution of full-scale measurements

$\alpha$  – factor that defines the dependence of pressure on contact area

$F_z(z_e)$  – exceedence probability

$\nu$  – expected number of events

$r$  – expected proportion of impacts

A value of zero for the data set offset,  $x_o$ , has proven to be conservative for small contact areas (Taylor, 2009). The present calculations assume that  $x_o$  is equal to zero. The expected number of events was randomly chosen to be 500 and the expected proportion of hits was set to 0.5. In other words, it is assumed that there are 250 ice impacts per year. The exceedence probability was selected to be 1%. This means that there is a 1% chance that an event will occur that results in an ice loading larger than the defined design load. The term  $\alpha$  is defined by the equation below.

$$\alpha = Ca^D$$

**Equation 4.3: CSA Local Pressure Area Coefficient**

In this equation the term  $a$  represents the nominal contact area and  $C$  and  $D$  are coefficients defined by full-scale data. Jordaan (2009) presents tabulated values of  $C$  and  $D$  corresponding to different full-scale ice trials. The full scale trials were completed by ice breaking ships in different ice environments. It was recommended to select the coefficient  $C$  based on similar ice conditions for which the structure is to be designed. The coefficient  $D$  was maintained at a mean value of -0.7 for each ice environment as

recommended. Three ice environments were considered including the Bering Sea in Spring, the Bering Sea in Winter, and the Beaufort Sea in Fall. The  $C$  coefficients corresponding to these conditions are 0.12, 0.28 and 0.53 respectively. The results of the local design loads for each ice environment are shown on the plot below.

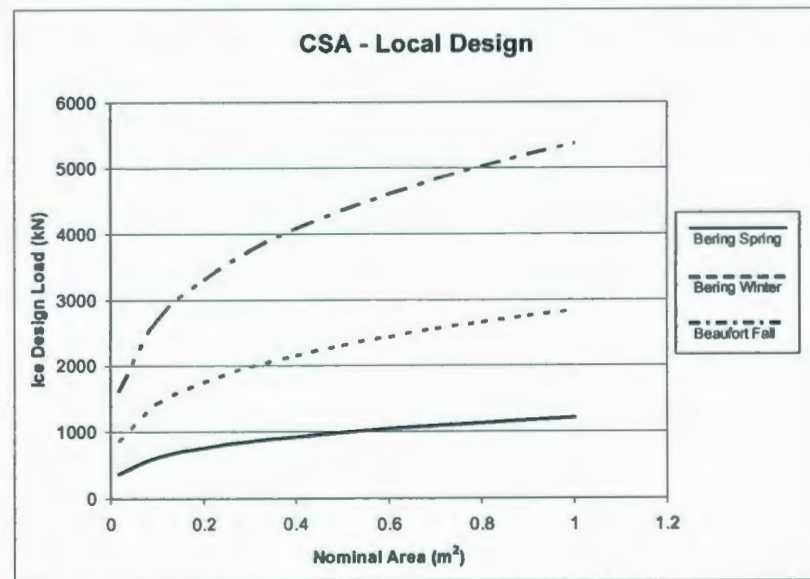


Figure 65: CSA Local Ice Loads

#### 4.2 ISO Ice Design Loads

The ISO guidelines describe the methodology behind calculating design loads using both the deterministic and probabilistic method. The guidelines are used, following the deterministic approach, to calculate the global and local design loads for the lifeboat in the level ice condition.

### 4.2.1 Global Loading

The global pressure was defined in terms of the structure width and the ice thickness. The structure width was taken as the maximum lifeboat breadth, which is 2.2 m. The equation for calculating the global pressure is provided below.

$$P_G = C_R h^n \left( \frac{w}{h} \right)^m$$

Equation 4.4 : ISO Global Ice Pressure

In this equation  $h$  and  $w$  are the ice thickness and structure width. The variables  $m$  and  $n$  are empirical exponents that account for the size effect, and the constant  $C_R$  is an ice strength coefficient. The value of the empirical exponent  $m$ , was given as -0.16. The exponent  $n$  was given to be -0.3 for nominal areas greater than or equal to one. For lower nominal areas the exponent is described using the equation below.

$$n = -0.50 + \frac{h}{5}$$

Equation 4.5: ISO Global Pressure Exponent

A constant ice contact width of 1.0 m is assumed. This relates to an ice thickness range of 0.1 m to 1.0 m. The ice strength coefficient,  $C_R$ , was selected to be 2.8. This is representative of an Arctic sea area and is based on full-scale testing. The global load was found by multiplying the global pressure by the corresponding nominal area. The global design loads for the lifeboat, as defined by ISO standards, are shown in the plot below.

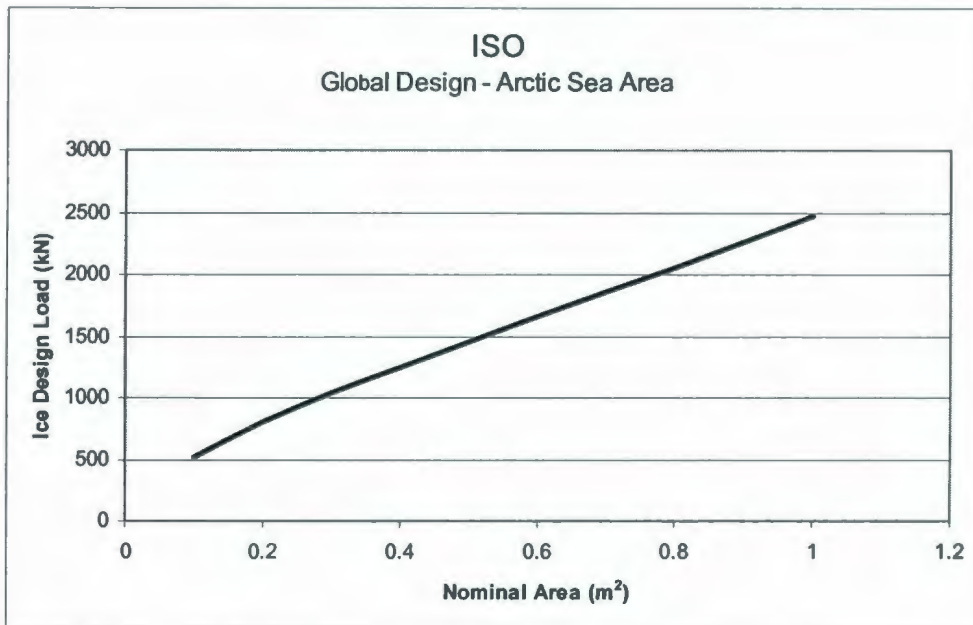


Figure 66: ISO Global Ice Loads

#### 4.2.2 Local Loading

The local pressure for first-year level ice was defined based on data from the Gulf of Bothnia. The local pressure is described by the equation below.

$$p_L = p_f \times \gamma_L$$

Equation 4.6: ISO Local Ice Pressures

In this equation  $\gamma_L$  is a constant that was recommended to be 2.5 when using the deterministic method. The variable  $p_f$  is defined as the full-thickness local pressure. This is the pressure representative of contact with the full floe thickness. The full thickness pressure was found using the equations below.

$$p_f = 2.35h^{-0.50} \quad \text{for } h > 0.35 \text{ m}$$

$$p_f = 4.0 \quad \text{for } h \leq 0.35 \text{ m}$$

Equation 4.7: ISO Local Ice Full Thickness Pressures

The local design loads, as defined by ISO standards, for the level ice condition, are shown in the plot below.

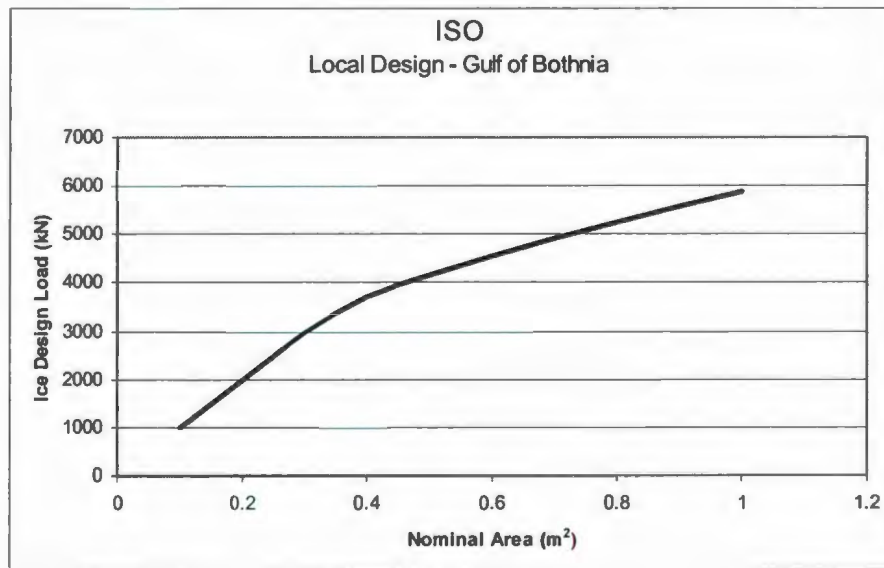


Figure 67: ISO Local Ice Design Loads

### 4.3 Design Load Comparison

The design ice loads calculated for the lifeboat using the CSA and ISO standards are compared to one another, laminate limitations defined by material testing and extended Popov model predictions.

### 4.3.1 CSA versus ISO

The design loads calculated based on the CSA and ISO standards are similar in terms of loading magnitudes. This was expected since the loads were calculated for the same craft, under similar ice conditions, and for identical contact areas.

The local design loads, for both standards, ranged from 500 to 6000 kN corresponding to contact areas between 0.1 m<sup>2</sup> and 1.0 m<sup>2</sup>. The CSA local design loads had a minimum of 500 kN and a maximum design load of 5500 kN corresponding to nominal areas of 0.1 m<sup>2</sup> and 1.0 m<sup>2</sup> respectively. The ISO local loads had a minimum of 1000 kN and a maximum of 6000 kN for the same nominal areas. The local design loads calculated using both standards are plotted together for comparison on the graph below.

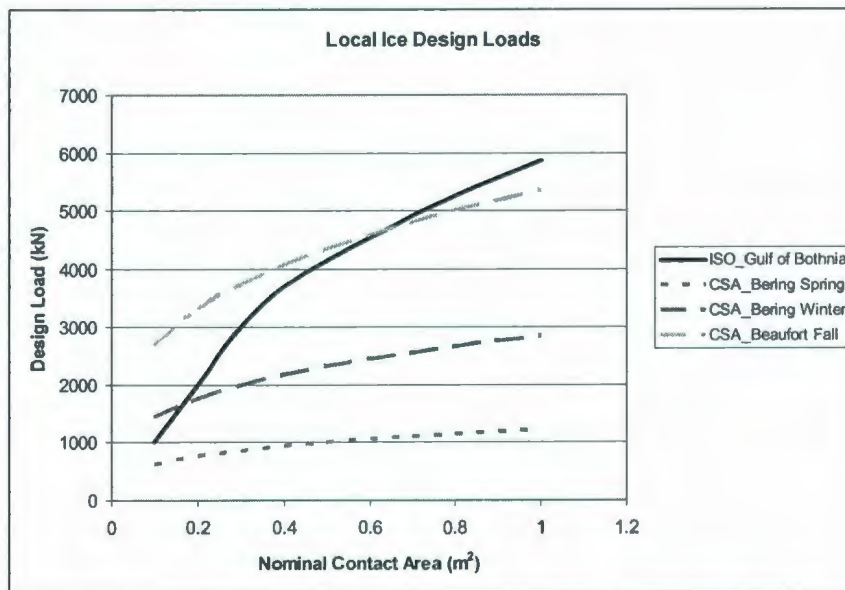


Figure 68: CSA vs ISO - Local Design

The global loads ranged from 500 kN to 3000 kN for both design standards. The CSA global loads ranged from 750 to 3000 kN while the ISO design loads ranged from 500 to 2500 kN. The global loads are plotted together for comparison on the graph below.

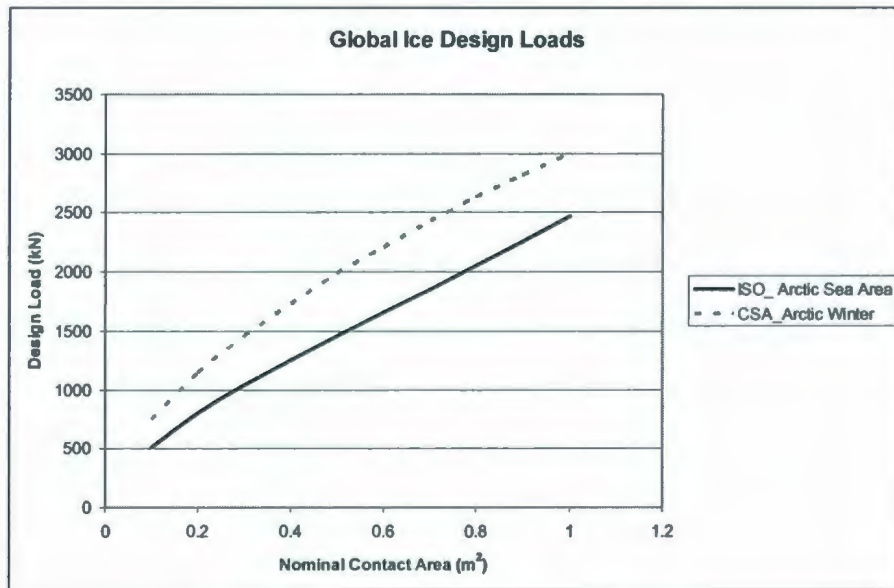


Figure 69: CSA vs ISO - Global Design

In terms of local design loads, the ISO standards have the strictest requirements for a nominal area of 1.0 m<sup>2</sup>. For global loads, the CSA guidelines have the more stringent requirement.

#### 4.3.2 Design Loads versus Laminate Limitations

Hydraulic ram testing of lifeboat laminate indicated an ultimate load of approximately 75 kN and a force corresponding to panel yielding of approximately 55 kN. These limitations resulted from tests conducted with 18"×18" panels that were cut from the hull of a

conventional lifeboat. The panels tested had surface area equal to approximately 0.21 m<sup>2</sup> and the contact area between the hydraulic ram and the laminate surface was 0.018 m<sup>2</sup>.

The global and local design loads were compared to the structural limitations at a nominal area of 0.018 m<sup>2</sup>. A summary of both the global and local design loads at this contact area is provided in the table below.

**Table 13: Design Loads for Nominal Area of 0.018 m<sup>2</sup>**

Regulation	Loading	Environment	Force (kN)
ISO	Global	Arctic Sea	172
ISO	Local	Gulf of Bothnia	180
CSA	Global	Arctic Winter	482
CSA	Local	Bering Spring	363
CSA	Local	Bering Winter	847
CSA	Local	Beaufort Fall	1604

The smallest design load for a contact area of 0.018 m<sup>2</sup> is the global requirement for the Arctic Sea. This load can be observed from Table 13 as 172 kN, which is more than double the ultimate load of lifeboat laminate as defined by panel tests. The lowest local requirement for this contact area is for the Gulf of Bothnia. This load requirement of 180 kN is over three times the structural yield limit and over two times the ultimate limit. The lowest global and local loads were obtained using ISO standards. The corresponding CSA loads were higher.

#### **4.3.3 Design Loads versus Model Predictions**

The extended Popov model was used to assess ice impact forces on the lifeboat arising from the lifeboat contacting ice that had strength typical of Beaufort Sea ice. The results

indicated that at an ice thickness of 1 m and impact speed of 3.1 m/s the ice impact force would be approximately 74 kN.

Local ice design loads for ice strength typical of Beaufort Sea ice was assessed using CSA design methodology. The local design loads ranged from approximately 1604 kN to 5400 kN corresponding to contact areas between 0.018 m<sup>2</sup> and 1.0 m<sup>2</sup> and an ice thickness of 1.0 m. The design loads are over 20 times larger than the predicted ice load at an ice thickness of 1.0 m. This is true for the range of design loads corresponding to different contact areas.

#### *4.4 Applicability to Small Craft*

The purpose of this section is to address the applicability of the CSA and ISO standards to small craft design. The standards were created to address design issues relating to large installations operating in ice. Large offshore structures react quite differently to ice loading than small craft. In general, large structures have higher rigidity than small craft. Hull flexibility leads to a reduction in ice loading since a portion of the available impact energy is dissipated in hull deformation. There is also a large mass variation between small craft and large vessels or installations, which affects the available momentum of the ice collision.

A significant structural difference between conventional lifeboats and large-structure ice loading concerns the structural design of the bow region. Large vessels designed to operate in ice have ice breaking bows that cause ice to fail in flexure. The flexural limit of

ice is, in general, lower than the compressive limit and thus ice-breaking bows experience lower ice forces than conventional bows. Many small boats such as lifeboats are not designed for ice operation and do not have an ice-breaking bow configuration.

Three primary factors that limit ice loading on structures are limit stress, limit force, and limit momentum (Croasdale, 1984). Limit stress involves ice local failure, while limit force refers to the condition in which the available loading force is less than the limit stress. The limit force condition is due to insufficient driving forces such as wind and waves. The limit momentum condition results when the combined affect of mass and impact speed is insufficient to cause ice failure. The CSA and ISO standards were created to design a structure to withstand ice failure loads (limit stress). Other load limiting mechanisms were neglected in the formulation of these standards. The limit stress is the highest of the three limiting conditions.

The PA constants in the standards all arose from field testing conducted with large vessels. It is possible that these constants are not applicable to small craft design. The standards do not include an impact speed variable. However, field test and model predictions indicate that impact speed has an influence on impact ice force magnitude. The design load requirements for the lifeboat outlined by both the CSA and ISO standards are much (two to three times) larger than the current structural capability of the lifeboat. The design loads estimated by the standards are not suited for design of the flexible structures typical of small craft.

## 5 Conclusions

A simple semi-empirical model has been developed to predict the impact forces arising from a conventional lifeboat colliding with ice. The extended Popov model is devised based on a conservation of energy approach. It contains empirical components such as the coefficient of restitution and panel stiffness defined from laboratory experimentation. Two ice failure modes are considered: compression and flexure. A key element of this model is that it considers hull deformation due to ice impact. The consideration of hull flexibility is appropriate for lifeboats as they have non-rigid hulls.

The extended Popov model contains variables relating to hull geometry, added mass, ice strength and ice size and thus has the generality required of a predictive model. The model was used to predict ice impact loads typical of field trial conditions. Predictions compared well to the ice loads measured during field trials for both the pack and level ice case.

Lifeboat laminate limitations were defined in terms of yield and ultimate impact force. These values were based on hydraulic ram testing of laminate panels. Structural limitations were used in conjunction with model predictions of ice impact forces to create an operational guidance plot. This type of plot can be used as a means of assessing safe and unsafe operational procedures for a lifeboat in ice.

Operational guidance plots can be developed by finding the intersection of the model prediction curves with the yield and ultimate structural limits. For illustrative purposes an example is considered in which the conventional lifeboat impacts ice that has a compressive strength of 1.44 MPa, a flexural strength of 391 kPa, and a mass of 380000 kg. Model predictions were made for a range of ice thicknesses from 0 to 1.2 m. The impact speed considered in this example is 3.1 m/s. The operational guidance plot for this situation is shown in Figure 70.

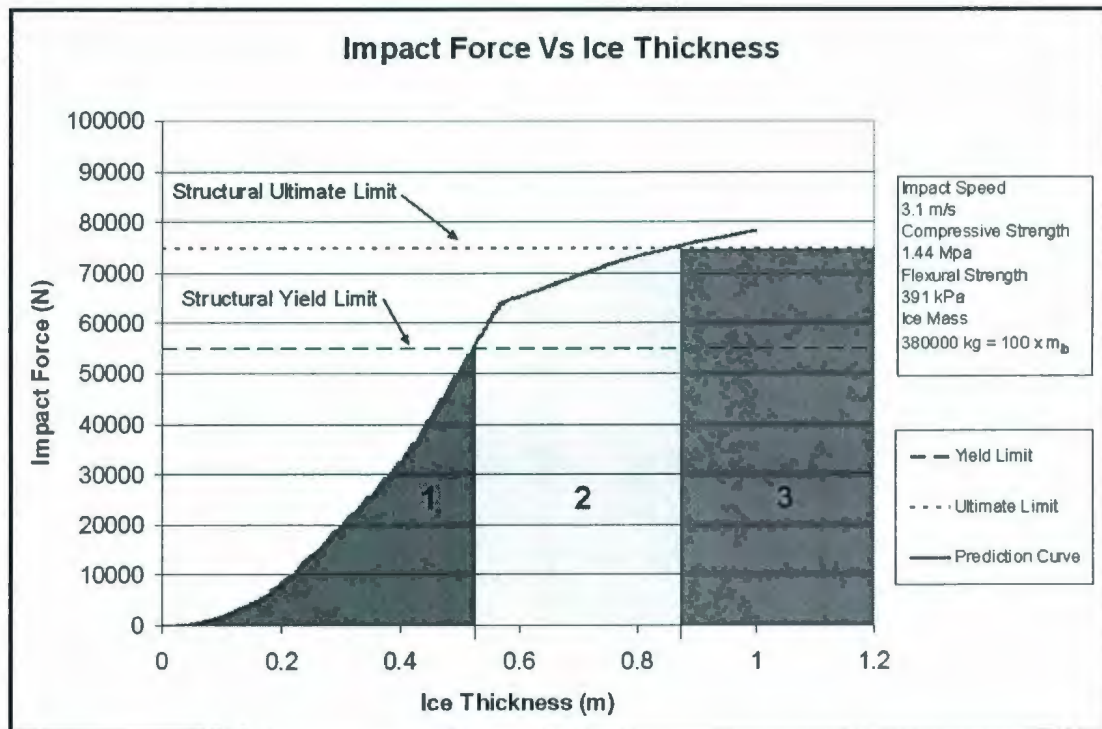


Figure 70: Operational Guidance

The plot area is divided into three sections. Section 1 represents ice collisions that result in an impact force below the force required to cause structural yielding. Section 2 is

representative of ice collisions that result in an impact load above the structural yield force but below the force required to cause ultimate structural failure. The third section represents ice collisions that result in an impact force above the force required to cause ultimate structural failure.

For the situation considered in this example, the lifeboat can impact ice up to a thickness of approximately 0.52 m without causing structural damage. Operational guidance plots similar to Figure 70 can be made for a variety of different interaction situations by adjusting the parameters in the extended Popov prediction model accordingly.

Extended Popov model predictions of ice loads for the lifeboat operating in ice conditions typical of the Beaufort Sea were compared to ISO and CSA structural load requirements defined for the same environmental area. The design load requirements were much larger than the predicted ice loads. This suggests that these standards are not applicable for small craft design. This was expected since the standards were devised to govern large offshore installations and vessels operating in ice.

The research presented in this thesis can provide insight into the structural design of an ice-capable lifeboat. It can also be incorporated into performance based standards that govern lifeboat operation in ice environments. The approach undertaken for the development of an operational guidance plot can be extended to define safe and unsafe conditions for any small craft operating in ice.

## References

American Society for Testing and Materials (1996), Standard Test Method for Tension-Tension Fatigue of Polymer Matrix Composite Materials, D3479 / D 3479M.

Barker, A.; Simões Ré, A.; Walsh, D; Kennedy, E., (2004) Model Testing of an Evacuation System in Ice-Covered Waters With Waves, PERD/CHC Report 61-6, 92 pages.

Blevins, R. D; (1979) Formulas for Frequency and Mode Shape, Copyright by Van Nostrand Reinhold Company Inc; New York, USA.

Browne, Robin P; Gatehouse, Evan G; Reynolds, Alan, (2008) Design of an Ice Strengthened Lifeboat, Proceedings of ICETECH 2008, 8 pages.

Cammaert, A. B; Muggeridge, D. B; (1988) Ice Interaction with Offshore Structures, Van Nostrand Reinhold Company Inc; New York, USA.

Colbourne D. B., (1987) A Three Component Method of Analyzing Icebreaking Resistance, PhD Dissertation, NRC/IOT, IR-1989-07.

Croasdale, K. R., (1984) The limiting driving force approach to ice loads, Proc. of Offshore Technology Conference, OTC Pap. 4716 (1984), pp. 57-64.

Daley, Claude, (1999) Energy Based Ice Collision Forces, Proc. Of the 15<sup>th</sup> International Conference on Port and Ocean Engineering under Arctic Conditions, Helsinki University of Technology, Finland, August 1999, 13 pages.

Daley, Claude, (2004) A Study of the Process-Spatial Link in Ice Pressure-Area Relationships, PERD/CHC Report 7-108, 30 pages.

Daley, Claude, (2009) Sea Ice Engineering: Theory and Practice, Draft Version, 138 pages.

Gagnon, R., (2004) Analysis of Laboratory Growler Impact Tests, Cold Regions Science and Technology 39, pp. 1-17.

Ghoneim, G. A., Keinonen, A. (1983) Full Scale Impact Tests of Canmar Kigoriak in Thick Ice, Proceedings of the 7<sup>th</sup> POAC Conference, Helsinki.

Igloliorte, Gareth; Kendrick, Andrew; Fredj, Abdelfettah, (2007) Global and Structural Performance of a TEMPSC in Pressured Ice, Proceedings of the 26th International Conference on Offshore Mechanics and Arctic Engineering (OMAE), 14 pages.

Igloliorte, Gareth; Kendrick, Andrew; Brown, Robert; Boone, Jim, (2008) Performance Trials of a Totally Enclosed Motor Propelled Survival Craft, Proceedings of ICETECH 2008, 9 pages.

International Maritime Organization (2007) Guidelines for Ships Operating in Polar Waters – Annex 11, 36 pages.

International Maritime Organization, (2003) Life-Saving Appliances, London, 187 pages.

International Organization for Standardization (2000) Plastics – Determination of puncture impact behaviour of rigid plastics, 6603-2.

International Towing Tank Conference (1978) Proceedings of the 15<sup>th</sup> ITTC, The Hague, The Netherlands, published by the Netherlands Ship Model Basin, Wageningen, Netherlands.

Johansson, Ben M. (2006) Ice Breaking Life Boat, Proceedings of ICETECH 2006, Paper Number ICETECH06-162-RF.

Jordaan, I. J. et al. (1993) Probabilistic Analysis of Local Ice Pressures, Journal of Offshore Mechanics and Arctic Engineering.

Kerr, A. D., (1979) On the Buckling Force on Floating Ice Plates, Proceedings of IUTAM Symposium, Copenhagen.

Kotras, T. et al. (1983) Predicting Ship Performance in Level Ice, SNAME Transactions, Volume 91, New York.

Lau, Michael; Simões Ré, Antonio, (2006) Performance of Survival Craft in Ice Environments, Proceedings of ICETECH 2006, 8 pages.

Lewis, J. W., Edwards, R. Y., (1970) Methods for Predicting Icebreaking and Ice Resistance Characteristics of Icebreakers, SNAME Transactions, Volume 78.

Lindqvist, Gustav, (1989) A Straightforward Method for Calculation of Ice Resistance of Ships, The 10th International Conference on Port and Ocean Engineering Under Arctic Conditions, Volume 1, pp. 723 – 735.

Liu, J., Lau, M., Williams, M., (2006) Mathematical Modeling of Ice-Hull Interaction for Ship Maneuvering in Ice Simulations, Proceedings of ICETECH 2006, 8 pages.

Milano V. R., (1973) Ship Resistance to Continuous Motions in Ice, SNAME Transactions, Volume 81.

Milano V. R., (1980) A Re-Analysis of Ship Resistance When in Continuous Motion Through Solid Ice, Proceedings of Intermaritec Symposium, Hamburg.

O'Brien, Daniel P., (2004) Seascape System of Evacuation, 17th International Symposium on Ice, 30 pages.

International Standards Organization, (2008) Petroleum and Natural Gas Industries – Arctic Offshore Structures, 19906, 428 pages.

Popov, Yu, N; Faddeyev, O. V; Kheysin, D. Ye; Yakovlev, A. A., (1968) Strength of Sailing Ships in Ice, Sudostroyeniye Publishing House, Leningrad, 1967, 223 pages.

The Society of Naval Architects and Marine Engineers, (1988) Principles of Naval Architecture, Volume II, Resistance, Propulsion and Vibration, 327 pages.

Sanderson, T.J.O., (1988) Ice Mechanics, The Dorset Press, Great Britain, 253 pages.

Seligman, Bruce; Bercha, Frank; Hatfield, Peter, (2008) ARKTOS Full-Scale Evacuation Tests, Proceedings of ICETECH 2008, 6 pages.

Simões Ré, Antonio; Veitch, Brian J., (2007) Lifeboat Operational Performance in Cold Environment, Royal Institution of Naval Architects (RINA) International Conference, 6 pages.

Simões Ré, Antonio; Veitch, Brian; Kuczora, Andrew, (2008) Field Trials of an Instrumented Lifeboat in Ice Conditions, Proceedings of ISOPE, 6 pages.

Spenser, D. S., Jones, J. and Colbourne, D. B., (1992) A Proposed Standard Method for Conduct and Analysis of Ice Resistance Model Tests, Institute for Marine Dynamics, LM-1992-01.

Standards for Lifeboats, Transport Canada TP 7320 E, 1992, 62 pages.

St. John, James W. et al. (1986) Consolidation of Local Ice Impact Pressures Aboard the USCGC Polar Sea Final Report, Maritime Administration, Washington D. C, USA.

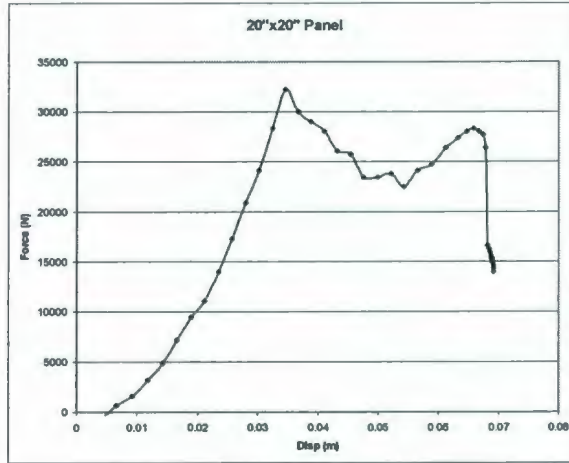
Taylor, Rocky et al., (2009) Local Design Pressures for Structures in Ice: Analysis of Full-Scale Data, Proceedings of the ASME 28<sup>th</sup> International Conference on Ocean, Offshore and Arctic Engineering, Hawaii, USA.

Timco, G.W., (1986) Indentation and Penetration of Edge-Loaded Freshwater Ice Sheets in the Brittle Range, Proceedings of the Fifth Conference on Offshore Mechanics and Arctic Engineering (OMAE), Tokyo.

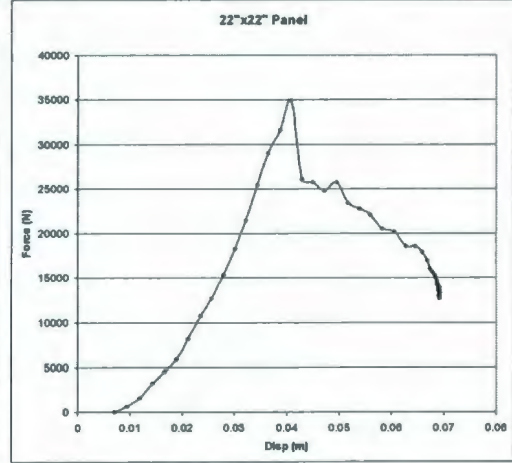
Timco, G. W; Dickins, D. F., (2005) Environment Guidelines for EER Systems in Ice-Covered Waters, Cold Regions Science and Technology 42 (2005) 201 – 214.

## **APPENDIX A**

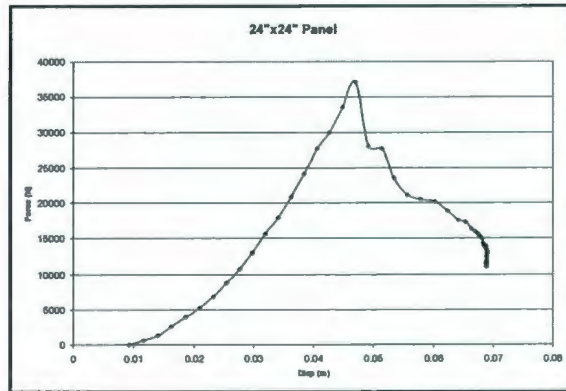
### 2009 Hydraulic Ram Test Results



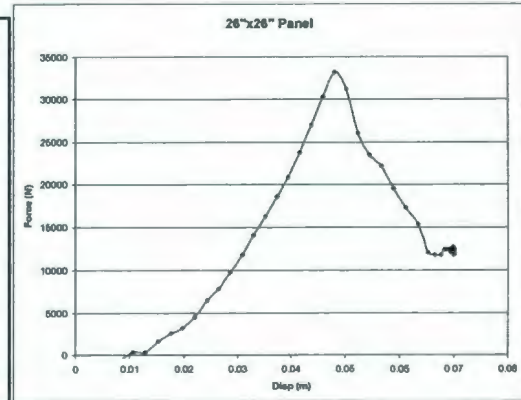
**A1**



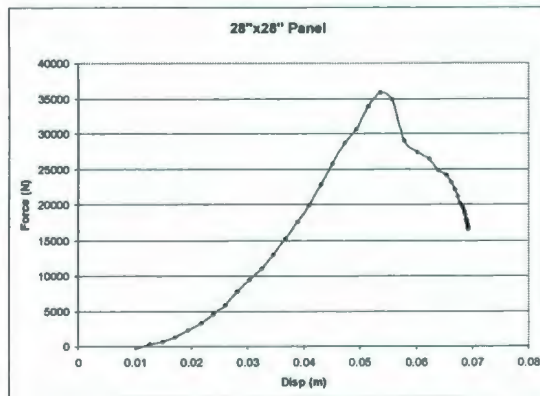
**A2**



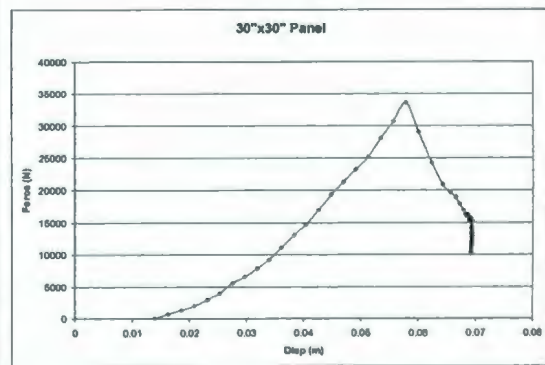
**A3**



**A4**



**A5**



**A6**

## **APPENDIX B**

### Field Trial Results

Date	Impact Position	Ice Type	Ice Thick (cm)	Ice Dimension (m)	Force (N)	Velocity (m/s)
Apr-22	Front and side	Pack	Undeterminable	Undeterminable	1764	1.3
Apr-22	Front and side	Pack	Undeterminable	Undeterminable	2393	1.3
Apr-22	Front	Pack	4	2.5x2	3195	1.4
Apr-22	Side	Pack	Undeterminable	1.5x1	2553	2
Apr-22	Side	Pack	13	1.5x2	4449	0.81
Apr-22	Side	Pack	8	1.5x2	4239	1.6
Apr-22	Front	Pack	4	5x2.5	876	1.6
Apr-22	Side	Level	4	Undeterminable	843	1.5
Apr-22	Front	Level	8	Undeterminable	5338	1.9
Apr-22	Side	Pack	8	1x1.5	5168	1.9
Apr-22	Front	Pack	10	3x2.5	6342	1.9
Apr-22	Front	Pack	5	2x2.5	5541	1.9
Apr-22	Front	Pack	Undeterminable	2x0.75	18556	2.5
Apr-22	Front	Pack	8	1x2.5	2762	1.9
Apr-22	Side	Pack	6	1x1.5	4377	0.4
Apr-22	Front	Pack	7	Undeterminable	1575	0.9
Apr-22	Front	Level	5	Infinite	5382	2.2
Apr-22	Front	Level	7	Infinite	4121	0.47
Apr-22	Front	Level	9	Infinite	7656	0.35
Apr-22	Front	Level	8	Infinite	4435	2.4
Apr-23	Front and side	Pack	15	Slushy	2264	0.96
Apr-23	Front	Pack	Undeterminable	8x1.5	10820	1.8
Apr-23	Side	Level	7	Infinite	5725	1.6
Apr-23	Side	Pack	3	1x1	1262	0.84
Apr-23	Side	Pack	Undeterminable	10x2	12079	2.4
Apr-23	Side	Pack	Undeterminable	2x1	8675	1.9
Apr-23	Side	Pack	Undeterminable	8x2	16518	1.9
Apr-23	Front	Pack	Undeterminable	2.5x2.5	5663	2.5
Apr-23	Side	Pack	7	1x2.5	6011	2.6
Apr-23	Front and side	Pack	Undeterminable	4.5x3	4007	2.5
Apr-23	Front	Level	12	Infinite	1637	1.1
Apr-23	Front and side	Pack	6	1.5x2	7094	2.5
Apr-23	Side	Pack	17	Infinite	17794	2.6
Apr-23	Side	Level	10	Infinite	4658	2.5
Apr-23	Front and side	Level	10	Infinite	3606	0.56
Apr-23	Side	Level	5	Infinite	3807	2.5
Apr-23	Front	Level	5	Infinite	4841	0.56
Apr-23	Front and side	Level	10	Infinite	2114	2.5

Apr-23	Front	Pack	7	2x3	2935	1.5
Apr-23	Side	Pack	8	2x1.5	8225	2.6
Apr-23	Side	Level	8	Undeterminable	4827	0.73
Apr-23	Side	Pack	Undeterminable	1.5x1	8400	2.6
Apr-23	Side	Pack	9	4x2.5	16331	2.2
Apr-23	Front and side	Pack	9	5x6	1667	1.4
Apr-23	Front and side	Level	10	Infinite	4578	2.6
Apr-23	Front and side	Level	5	Infinite	2028	2.5
Apr-23	Front and side	Level	5	Infinite	3278	2.5
Apr-23	Front and side	Level	8	Infinite	4875	2.4
Apr-23	Side	Pack	19	2x3	2918	1.4
Apr-23	Front	Pack	4	Slushy	1829	2.5
Apr-23	Side	Level	8	Infinite	2027	1.8
Apr-23	Front	Pack	7	1.5x1.5	1936	1.5
Apr-23	Front and side	Level	5	Infinite	1963	2
Apr-23	Front	Pack	10	2x1	2792	2.2
Apr-23	Front and side	Pack	9	2x3	5518	2.4
Apr-23	Side	Pack	9	Infinite	4665	1.2
Apr-23	Side	Pack	7	Infinite	3038	2.1
Apr-23	Front	Level	8	Infinite	11886	1.9
Apr-23	Side	Pack	Undeterminable	3x3	7135	2.4
Apr-23	Side	Pack	17	4x5	13852	1.9
Apr-23	Front	Pack	Undeterminable	1x1.5	2449	2.1
Apr-24	Front	Level	5	Slushy	1270	2.4
Apr-24	Front	Pack	10	1x1	1185	2.6
Apr-24	Front	Pack	20	12x5	17005	2.2
Apr-24	Side	Pack	Undeterminable	1.5x2	4283	1.6
Apr-24	Front impact	Level	9	Infinite	3246	2.4
Apr-24	Front and side	Level	Slushy	Infinite	6533	2.2
Apr-24	Front and side	Level	19	Infinite	3208	2.3
Apr-24	Side	Level	19	Infinite	3232	2.3
Apr-24	Front	Pack	9	2x3	1943	1.8
Apr-24	Front	Pack	9	2x4	2622	1.8
Apr-24	Front	Level	Slushy	Infinite	6858	2.2
Apr-24	Front	Level	Slushy	Infinite	5805	1.7
Apr-24	Front	Level	5	Infinite	5419	1.6
Apr-24	Front	Pack	6		4265	1.4
Apr-24	Front and side	Pack	6	4x6	3672	1.6
Apr-24	Front and side	Level	8	Infinite	9226	1.6
Apr-24	Side	Level	6	Infinite	578	0.6
Apr-24	Side	Pack	12	1x2	4840	1.6

Apr-24	Side	Pack	9	10x15	3802	1.7
Apr-24	Side	Level	14	Infinite	9085	1.1
Apr-24	Front	Pack	13	0.5x3	3382	1.3
Apr-24	Front and side	Level	13	1x3	5294	1.3
Apr-24	Front	Pack	10	2.5x2.5	2446	0.86
Apr-24	Front	Level	9	Infinite	9965	1.1
Apr-24	Front and side	Level	20	Infinite	14135	2.1
Apr-24	Front and side	Pack	12	2x3	1419	1.9
Apr-24	Front and side	Pack	14		1467	1.6
Apr-24	Side impact	Pack	Undeterminable	5x6	11898	1.6
Apr-24	Front impact	Level	11	Infinite	5696	1.4
Apr-24	Front and side	Pack	15	1.5x2	1622	1.2
Apr-24	Side	Level	18	Infinite	1369	1.3
Apr-24	Front	Pack	12	1x1	1314	1.4
Apr-24	Front and side	Level	9	Infinite	1627	1.3
Apr-24	Side	Pack	10	1x3	6320	0.89
Apr-24	Front	Level	7	Infinite	7427	1.8
Apr-24	Front and side	Pack	Undeterminable	1.5x3	5724	1.7
Apr-24	Side	Pack	14	3x6	3890	1
Apr-24	Side	Pack	4	Slushy	3768	0.88
Apr-24	Front	Level	Undeterminable	Infinite	11168	1.1
Apr-24	Side	Pack	12	5x4	7343	1.4
Apr-24	Front	Pack	Undeterminable	4x1.5	4230	1.3
Apr-24	Front and side	Level	Undeterminable	Infinite	1464	2.2
Apr-24	Side	Pack	Undeterminable	2x5	1924	0.89
Apr-24	Side	Pack	8	2.5x2	5817	1.8
Apr-24	Front and side	Pack	Undeterminable	2x1.5	4718	0.31
Apr-24	Side	Level	11	Infinite	5113	0.29
Apr-24	Front and side	Level	11	Infinite	7528	0.34





